University of Nevada, Reno

# Experimental Study of X-ray Production and Implosion Dynamics of Low-, Mid-, and High-Atomic-Number Materials on University-Scale Z-pinch Machines of Various Architecture

A dissertation submitted in partial fulfillment of the requirements for the degree of Doctor of Philosophy in Physics

by

Christopher James Butcher

Dr. Victor L. Kantsyrev – Dissertation Advisor

August 2022

THE GRADUATE SCHOOL

We recommend that the dissertation
prepared under our supervision by

**Christopher James Butcher**

entitled

**Experimental Study of X-ray Production and Implosion Dynamics of Low-, Mid-, and High-Atomic-Number Materials on University-Scale Z-pinch Machines of Various Architecture**

be accepted in partial fulfillment of the
requirements for the degree of

**DOCTOR OF PHILOSOPHY**

Victor Kantsyrev, Ph.D., Advisor

Alla Safronova, Ph.D., Committee Member

Joshua Williams, Ph.D., Committee Member

Thomas White, Ph.D., Committee Member

Adam Steiner, Ph.D., Committee Member

Ana de Bettencourt-Dias, Ph.D., Committee Member

Hans Moosmüller, PhD., Graduate School Representative

Markus Kemmelmeier, Ph.D., Dean, Graduate School

August 2022

## Abstract

Earlier research with the novel Double Planar Wire Array (DPWA) and Double Planar Foil Liner (DPFL) loads imploded on the high-impedance UNR Zebra Marx bank generator showed them to be excellent radiators of x-rays. This work focuses heavily on implosions of DPWA loads of low- to mid- to high-atomic-number metals and low-atomic-number DPFL loads performed using the low-impedance UM MAIZE Linear Transformer Driver (LTD). The DPWAs consisted of two wire planes of micron-scale sized wires, while the DPFLs consisted of two planes of micron-scale thickness foils. Current from the machine causes the load planes to ablate, creating two sheets of plasma that pinch in the center of the arrays. As the load begins to implode, radiation in a broad range is emitted, and then detected using various diagnostics, such as an absolutely calibrated PCD, filtered Si-diodes, x-ray pinhole cameras, spectrometers, and a fast, visible light camera which captures plasma evolution.

In contrast to the Marx bank (which has been in widespread use in pulsed power research for decades), the LTD is a relatively new pulsed power architecture with the theorized potential to be more efficient than the widely used Marx bank generators. However, up to this point, very little is known on how DPWAs and DPFLs implode on LTDs, so it is important to study. Also, by making comparisons to previous implosions of similar load types on the Zebra generator, we can better understand how the changes in machine architecture and current values affect the radiation emission and implosion dynamics. In addition, unlike the Zebra generator, the low-impedance of the MAIZE LTD makes the discharge current highly susceptible to changes in the load inductance. By

studying the load inductance throughout the Z-pinching process of DPWAs and DPFLs on the MAIZE LTD, we can better optimize future loads for the potential of reaching higher peak currents, faster current risetimes, and greater x-ray emission.

To perform experimental low-current produced plasma research on the UNR main campus, and to test x-ray diagnostics as well as train students, we have developed a hard x-ray source based on a vacuum diode with laser-plasma cathode triggering dubbed "Sparky-HXRS" (or Sparky Hard X-Ray Source). One of the main objectives of this research was to study the hard x-ray characteristic radiation which is believed to be caused by inner-shell ionization of neutral atoms by non-thermal electron beams propagating through the cold thermal plasma. Such hard x-ray characteristic radiation as well as its polarization properties has not yet been studied in detail in pulsed power plasmas. Sparky-HXRS was designed for producing monochromatic x-rays while keeping the production of bremsstrahlung low in comparison. Laser-driven vacuum x-ray diodes have been attractive for the generation of short-duration x-ray pulses in a compact set-up, which can be temporally synchronized with the laser pulse. Such a device can operate with any voltage, and, if operated with the optimal voltage, can provide better monochromatization of a particular radiation range. The device was designed such that any desired metal could be studied by using that material of interest to form the anode. A number of anode materials were studied with varying atomic numbers, including: brass (an alloy of copper and zinc), stainless steel (an alloy of iron and chromium), titanium, and tungsten. The development of the Sparky-HXRS device also included the development of an "open-air" spectropolarimeter, to study the polarization of characteristic x-rays.

This dissertation is dedicated to my parents, Terrance and Chandra Butcher, for always supporting me.

## Acknowledgments

This section has been one of the most difficult to write out of this whole dissertation. The more I thought about it, the more people and organizations came to mind. First and foremost, I would like to thank my advisor, Dr. Victor Kantsyrev, without which this work wouldn't have been possible. I will forever be thankful for the years of mentorship and guidance, and all the opportunities given to me in a number of laboratories and conferences. I also want to thank my Co-advisor, Dr. Alla Safronova, for all of her help over the years. I would also like to thank all the members of my committee: Dr. Thomas White, Dr. Joshua Williams, Dr. Adam Steiner, Dr. Ana de Bettencourt-Dias, and Dr. Hans Moosmuller. Thank you all for taking the time be on committee.

During my graduate career, I've had the opportunity to work with many other groups, most notably the Gilgenbach/McBride group at the University of Michigan. Without their help in running the experiments on MAIZE, much of this research wouldn't have been possible. In particular, I'd like to thank Dr. Ronald Gilgenbach, Dr. Ryan McBride, and Dr. Nicolas Jordan for allowing us to use their facilities, and for their mentorship during MAIZE campaigns. I would also like to thank Dr. Paul Campbell, Dr. David Yager-Elorriaga, and Stephanie Miller for all their help during the campaigns. Last from the Michigan team, I would like to thank Dr. Adam Steiner for his help and mentorship over the years, especially regarding the inductance modelling presented in this work.

I'd like to thank the UNR Physics Department and all the professors I've had the pleasure of learning under, from undergrad up until now. I would also like to thank the members of the UNR Physics machine shop, especially Wade Cline for all his help with

designing and building diagnostics and the Sparky-HXRS machine. Also, I would like to thank the UNR Physics office staff for all their help over the years.

I would also like to thank a number of organizations. When I first started college, I didn't know a single person, and as the first in my household to go to college I had no idea what I was in store for. The first club I joined was the TMCC Alpha Pi Gamma chapter of Phi Theta Kappa Honor Society, which helped me realize my potential. At UNR, the Society of Physics Students and the Astronomy Club helped me grow as both a scientist and student outside of the classroom. I owe a lot to these clubs and organizations, without which, I likely wouldn't be where I am today.

I have had the pleasure of working with and learning alongside many wonderful people in the UNR Physics program. I would like to thank many of the other members of Dr. Kantsyrev's experimental group, Dr. Ishor Shrestha, Veronica Shlyaptseva, and especially Dr. Kimberly Schultz for welcoming me into the group and teaching me how to work in a lab, as well as for all their company over the years. Also, I would like to thank the students of Dr. Safronova's theoretical group, most notably Dr. Emil Petkov, Dr. Austin Stafford, Ryan Childers, and Amandeep Gill. I'd also like to thank my fellow students Alex Rollings and Demitri Call, for being good friends over the years.

Lastly, I would like to thank my family. Especially my parents, Terrance and Chandra Butcher, for raising me and all the sacrifices they've made over the years to get me to where I am today. Also, I'd like to give a special thank you to my grandfather Robert Butcher, and my grandmother Cassandra Green for their support early on in my college career. I would also like to thank my grandfather, Dale Taylor, for all the help he's given me over the years.

This work was supported by the National Nuclear Security Administration under DOE grants # DE-NA0003047 and # DE-NA0003877. Experiments at the NTF were supported in part by # DE-NA0002075.

# Table of Contents

## Contents

## List of Tables

## List of Figures

# 1 Introduction and Motivation

Solid, liquid, gas, and plasma. These are the four states of matter. The first three (solids, liquids, and gases) are very well known to us, as they are abundant in our everyday lives. The fourth state, plasma, however, is not so abundant. Which is a bit ironic as, in the greater scope of the observable matter in the universe, plasma makes up nearly all of it. It is estimated that as much as 99.9% of the observable matter in the universe is made up of plasma, and yet we know relatively little about it, compared to our knowledge of the other states. This is because plasma only exists in the most extreme conditions, which are usually very fleeting in nature (such as a lightning strike), and up until the past century, have had very little ways to study it, by way of diagnostics and experimental facilities. However, experimental capabilities to create plasmas in the laboratory under controlled conditions have advanced extremely since the creation of the Marx bank generator in the 1920s [1], [2], and the advancement of experimental diagnostics has continually improved ever since as well. The recent development of the Linear Transformer Driver [3]–[7], a new form of pulsed power device based off of a different architecture than the Marx bank, has fueled new innovations and discoveries in the past two decades.

Before we move any further, we need to establish what exactly makes something a plasma. A plasma, loosely speaking, can be thought of as a hot, dense gas of ions and electrons, which is influenced by electric and magnetic fields. If we return to the states of matter, a solid is the “coldest” state a material can be in. If we add heat (energy) to the material, it becomes a liquid, and if we add even more, it becomes a gas. If we add even more heat, the material will begin to ionize and, once ionized sufficiently, the material will

begin to be influenced more by the electric and magnetic fields, and less by traditional hydromotive forces. This is, in my opinion, most eloquently explained by Chen [8], that plasmas share three conditions:

1) The size of the plasma (L) must be much larger than the Debye Length ($\lambda_D$) of the plasma. As the plasma is made up of an equal amount of positive and negative charges, the plasma's behavior can be termed as *quasineutral*, as the plasma will appear as electrically neutral from the outside. However, within the plasma, each charge has an electric potential field. The Debye Length is the characteristic length at which the potential from charges is neutralized by the collective potential of the surrounding charges. The Debye Length is a function of the electron and ion temperatures density. Therefore, in order for the plasma to be quasineutral, the size of the plasma must be sufficiently larger than the Debye Length, or else there will not be enough space for the collective shielding effect to occur, and it will be a simple ionized gas.

2) The number of the particles within a unit volume of the plasma ($N_D$) must be large enough to facilitate the first condition. If the plasma contained only a small number of particles, the screening effect couldn't occur. This unit volume is often described using a Debye Sphere (a sphere with radius $\lambda_D$), in which the density must be high enough to facilitate the electric screening effect described in the first condition.

3) The plasma frequency ($\omega$) must be high enough, and the time between collisions with neutral particles ($\tau$) must be low enough, such that $\omega\tau > 1$. The

electrons in a plasma, being much lighter and faster moving than the more massive ions, any disturbance will cause the electrons to move, and begin to oscillate around the more massive ions. This gives the electrons in the plasma a characteristic frequency. Also, the particles will collide with neutral atoms. However, if the time between collisions with neutral atoms is too high, then the electrons will be forced back into equilibrium and the plasma will behave as a standard ionized gas, where the behavior is determined more by typical hydrodynamic forces, and not electromagnetic forces.

It is for these reasons that plasmas do not typically occur in nature, as it is very difficult for these conditions to be met naturally on Earth (space, however, is another story). As mentioned, plasmas exist in some of the most extreme conditions. So, to study plasmas experimentally, we must simulate or create these extreme conditions. One of the most effective ways of doing this in the lab is through the use of pulsed power devices. A pulsed power device is a machine that stores energy in capacitors over time and discharges that energy in a much shorter timespan through a current carrying load. The current running through the load deposits enough energy to ionize the load material and form a plasma. Magnetic fields created by the current motion then cause the material to "pinch," or compress in some way which raises both the temperature and density of the plasma. The most common form of pinching is a Z-pinch, in which the material ablates between a parallel placed cathode and anode, causing the material to pinch along the Z-axis. However, there are other forms of pulsed power devices (such as dense plasma focuses) that cause the material to pinch in other geometries, but those are beyond the bounds of this work.

Traditionally, the most common form of pulsed power machine has been the Marx bank, which is a type of capacitor bank. In a traditional Marx bank, banks of capacitors are connected in series by voltage switches, with the final bank leading to the pulse forming line, and then to the current carrying load. The current is triggered by applying a voltage to the first switch, causing a breakdown and connection. The subsequent switches are then triggered sequentially, as the connecting of each capacitor bank causes the voltage to rise and breakdown the next switch trigger. This discharging of the capacitor banks in series causes Marx banks to be inherently high-impedance machines, as the impedance of each capacitor bank is added together. This high-impedance machine architecture is ideal for driving high voltages into high-impedance loads.

The newer architecture pulsed power device, Linear Transformer Drivers (LTDs), use a different method of discharging the current. The LTD takes advantage of inductive voltage adding by utilizing a number of capacitor bricks, each containing two capacitors (charged to opposite polarities) and a spark gap switch, all stored in parallel [9], [10]. When the current pulse is to be fired, each brick must be triggered individually, and the pulse is delivered to the load simultaneously. This method of having many parallel capacitors and triggering the switches in parallel keeps the inductance of the current path low, while maintaining a high voltage and capacitance, which is ideal for creating fast current-risetimes without the need for any pulse forming machinery. In addition, when compared to Marx banks of similar currents, LTD's compact physical machine architecture and relative ease of machine maintenance, makes them attractive for university-scale pulsed power experiments. However, as the LTD is a relatively new type of pulsed power device, it is important that we perform experiments to understand the implosion characteristics of

novel load Z-pinch types on such devices. We can then use data obtained from similar novel load implosions on Marx bank machines to benchmark and understand the results we see on LTDs.

The research from these pulsed power plasmas has many applications and importance. The most notable are fusion research, astrophysical research, and national defense, but plasma physics also has applications to the medical field as well as manufacturing of everyday products. While not naturally abundant on our Earth, plasmas are plentiful in our wider universe, as the lack of atmosphere in deep space allows plasmas to remain hot for sustained periods of time, such as the case for galactic nuclei and gaseous nebulas. And the gravitational forces of stars allow for them to remain hot and dense, while also facilitating fusion reactions in their cores. The problem, however, in studying these astrophysical phenomena is that they are, relatively speaking, *very* far away. So far away, that even rudimentary studies of some of these celestial bodies can require billions of dollars' worth of equipment. The question then becomes, how can we study these objects in a more controlled and, relatively, cost effective setting? And the answer to that is laboratory astrophysics. In the lab, by carefully choosing a set of parameters (such as voltage, energy, load material, load configuration, etc.), we can simulate the extreme conditions of these astrophysical objects, which allows us to place experimental diagnostics up close to the plasma. The field of laboratory astrophysics has allowed for us to better understand our universe and the basic physical principals within it.

The stewardship of our American nuclear stockpile is another major motivation behind this research. Plasma physics research is, in one sense, a study of matter in extreme

conditions, not unlike the extreme conditions that occur in a nuclear detonation. The study of high energy density plasma (HEDP) physics helps to ensure our fundamental understanding of the physical processes that occur in a detonation. Also, the x-rays emitted from pulsed power plasmas are of extreme importance to the stewardship of the nuclear stockpile, as x-rays of different energy can penetrate different depths of a nuclear weapon, making our understanding of the production and reaction to x-rays an utmost necessity to our nation's security.

Lastly, as the world's demand for energy continues to grow, it is becoming increasingly important to find an abundant source of energy. Fusion energy is the best candidate to meet that growing need. Fusion, at its simplest definition, is when two or more atomic nuclei combine to form a heavier element and, in the process/reaction, energy is expelled. Theoretically, through fusion, you could supply the world's energy with nothing but hydrogen (H), with the only byproduct aside from the energy being helium (He). Current fusion experiments typically use heavier isotopes of hydrogen, deuterium (D, an isotope of H in which the nucleus has one proton and one neutron) and tritium (T, a radioactive isotope of H that has one proton and two neutrons in the nucleus), as the heavier isotopes are more reactive than typical H (this higher reactivity also makes D and T important in nuclear weapons research).

This dissertation focusses on the results from a multitude of experiments that took place over many years on several different pulsed power machines of varying voltage, current, and energy. The first experiments took place on the University of Nevada, Reno's (UNR) Zebra Marx bank generator with Planar Wire Arrays (PWAs), a type of current

carrying load that had early pioneering research done at the UNR Zebra generator. The early Double Planar Wire Array (DPWA) experiments on the UNR Zebra generator proved them to be excellent radiators of x-rays as well as good diagnostic access to the central plasma forming region. For these reasons, DPWAs were also selected for experiments on the University of Michigan's MAIZE LTD machine, which was, at the time these experiments began, the only university-scale LTD machine of similar current scale to the UNR Zebra machine. As the LTD is an emerging pulsed power technology, it is essential that we understand how different loads perform on these machines.

Also, this dissertation showcases the development of a tabletop low-current hard x-ray source, named Sparky Hard X-ray Source (Sparky-HXRS), at the UNR main campus. The study of characteristic x-ray radiation is critical to understanding some of the fundamental physical atomic processes of different elements, however, they can be difficult to study in high energy implosions. For this reason, Sparky-HXRS was developed to meet this need. Sparky-HXRS has been modularly designed to be, theoretically, capable of producing characteristic radiation from any metal, based on the chosen anode and cathode material, as well as the voltage the anode is held at.

For this work, it is important to understand the fundamental physics of Z-pinches, which are described in Chapter 2, where the four phases of a Z-pinch are discussed. In addition, the various load types used in experiments in this work are described, as well as other important Z-pinch load types.

Aside from the machines themselves, experimental diagnostics are the most important aspects of experimental physics. Chapter 3 provides a detailed description of the

diagnostics used in this work. There are a number of diagnostic types discussed: current diagnostics, optical and laser-based diagnostics, electron beam diagnostics, and theoretical diagnostics/modelling. The first three are all physical diagnostics that are placed somewhere in or around the machines during the experiments. The last, theoretical diagnostics/modelling, are methods used to interpret the data collected from the physical diagnostics, such as calculating the plasma parameters from the spectrographs collected, or estimating the plasma inductance throughout a pinch from the current trace. These models are also used in predicting experiments, which is a necessary part of experimental planning, helping to get the most desired and optimized experimental results.

Chapter 4 presents results from both the UNR Zebra generator and the UM MAIZE LTD using DPWAs. In this work, DPWAs of various atomic number were analyzed: low-atomic-number aluminum, brass (a combination of two mid-atomic-number elements, copper and zinc), and high-atomic-number tungsten. Also presented is the first double planar foil liner on the MAIZE LTD. These experiments compare new results from the MAIZE LTD to previous data from the UNR Zebra generator. The results compare DPWA implosions from a low-impedance LTD machine to a high-impedance Marx bank. The low-impedance of the LTD means that the inductance change of the plasma has a large effect on the current trace of the machine, unlike what is seen on a higher-impedance machine like Zebra, where the current trace is highly repeatable. In addition, the efficiency of the LTD machine was tested, meaning that the energy output throughout the pinch was compared to the energy initially stored in the machine's capacitors. As LTDs were predicted to be more efficient than traditional Marx banks, the efficiency has to be measured.

Chapter 5 presents the development and results of the new tabletop Sparky-HXRS. The machine was developed to study characteristic radiation of a number of elements, most notably, to study the polarization of characteristic radiation of L-shell W. The results presented include data from a number of different anode materials (including brass, Ti, W, and stainless steel 304) and cathode materials (including Cu, Al, Ti, and W), as well as the development and implementation of new diagnostics used especially on the Sparky-HXRS machine, such as the open air spectropolarimeter and the implementation of the SOPHIA®-XO high-intensity x-ray CCD. The Sparky-HXRS was successful in producing characteristic radiation from every element implemented in experiments.

Finally, Chapter 6 summarizes some of the important finding and results of this work and discusses some of the plans to continue this research going forward.

# 2 Introduction to Z-pinch Plasmas

The Z-pinch is a common method for producing high energy density (HED) plasmas in the laboratory, by using strong currents to vaporize a current carrying load, and "pinching" the material through Lorentz forces (or **J** x **B** forces). There are a variety of current carrying loads that can be studied, such as foils, wires, gas puffs, and laser ablated plasma plumes. Using pulsed power devices, these loads are placed between an anode and cathode, and a high current is forced through the load in a short amount of time (typically on the scale of hundreds of ns). This high current causes the load to vaporize and ionize through Ohmic heating, and the **J** x **B** forces subsequently push the material towards the center of the load axis (the Z-axis, geometrically) causing the material to "pinch," forming a high-density, high-temperature plasma column. The pinching of the material results in further heating and ionizing of the plasma, causing the emission of extreme ultraviolet (EUV) and x-ray radiation.

## 2.1 The Four Phases of a Wire Array Implosion

There are four phases to a wire array z-pinch implosion: current initiation, in which the current begins flowing through the cold wires and they begin to heat due to resistive heating; the ablation phase, in which the heated wires begin to ablate; the implosion (or run-in phase), when the wire material has fully ablated and the magnetic fields send the material towards the center of the load; and lastly, stagnation, when the material all meets and "pinches" at the center of the load, this is also when the primary radiation burst occurs [11].

### 2.1.1 Current Initiation

The current initiation phase is the first phase of the wire array z-pinch process, and occurs within the first 5-20 ns of the current pulse [12]. When the current pulse begins to rise, some fraction of current is distributed into each wire, and, in turn, energy is deposited into each wire. This energy causes the wires to undergo a phase transition from solid (cold) wire, into a partially liquid and gas phase. As the current continues to rise, a critical voltage threshold is passed; at this point, a resistive voltage collapse occurs along the wires surface, causing the formation of a low-density coronal plasma on the wire surface. This plasma, having a much lower resistance than the still intact inner wire cores, robs some of the continuing current from the wires, forming what is known as the inhomogeneous core-corona plasma [13].

### 2.1.2 Ablation

Ablation of the wires is the second, and longest, phase of the wire array Z-pinch process, taking up around 50-80% of the total pinching process duration. Immediately proceeding the formation of the core-corona plasma, the magnetic forces of the individual wires contain the coronal plasma around the wires, however, as the current continues, so too does additional material continue to ablate from the dense wire core due to Ohmic heating. This additional influx of material to the core-coronal plasma causes a strong density gradient around the wire, which expands [12], [14]. The total expansion or maximum size of the coronal plasma diameter is dependent upon the wire material [15].

At this point, the Lorentz Force (**J** x **B** forces) send the coronal plasma streaming towards the center of the load, or the aptly named z-axis of the load. This coronal plasma

streams towards the z-axis at a near constant velocity, which forms the precursor plasma column along the z-axis where the pinch will ultimately occur [16]. In addition to the continued Ohmic heating, the kinetic energy of the streaming plasma is thermalized, beginning the emission of EUV radiation, which continues throughout the next phase (implosion) as well [17].

The precursor plasma column was first observed in ref. [18], and occurs when portions of the core-coronal plasma is sloughed off and is forced into the center of the load by the **J** x **B** forces. This phenomena has been observed for cylindrical wire array implosions at both the 1 MA current level machines [19]–[22] as well as higher multi-MA level machines [23] as well as for double planar wire arrays at the 0.5-1 MA current scale [24]–[28].

The precursor plasma has been observed to progress through three distinct stages: the first stage consists of the initial column formation, with a larger diameter relative to the later stages; the second stage is the contraction stage, which is also the primary radiative output from the precursor (analogous to a small z-pinch); and the third and final stage is the expansion, which occurs as more material flows from the outer ablating material, and this stage lasts up until the overall pinch of the load. For DPWA implosions on the MAIZE LTD, this precursor column was found to have a significant impact on the current trace and subsequent implosion (see Section 4).

### 2.1.3 Implosion

The implosion is the third phase of the wire array z-pinch. The implosion phase begins when the wires have ablated enough for gaps to form in the wire cores, allowing the

magnetic field to penetrate the array [29]. This accelerates the remaining wire material towards the center of the load. Ideally, all material would be pushed towards the center and collide (pinch) at the same moment in time. However, as the magnetic field penetrates the gaps, magnetic bubbles are formed, which cause an asymmetry in the movement of mass. These magnetic bubbles also grow under Rayleigh-Taylor instabilities. This asynchronicity in mass movement causes the implosion intensity to be greatly reduced, when compared to ideal implosion approximations. It has been found that the early emission of EUV radiation, beginning in the ablation phase and continuing through the implosion phase, accounts for about 10% of the total EUV radiation throughout the pinch [17].

### 2.1.4 Stagnation

Stagnation is the fourth and final phase of the wire array z-pinch, and the phase coinciding with the main radiation emission. Following the implosion phase, as the leading edge of the plasma fronts collide along the z-axis, much of the kinetic energy of the plasma is thermalized on impact. The imploding plasma compresses the precursor plasma column and produces large bursts of EUV and x-ray emission (about 50-60% of the total EUV radiation throughout the pinch [17]). The following pinch destruction and plasma expansion corresponds to low levels of EUV radiation emission (about 10-20% of the total) as the thermal energy decreases. The EUV radiation emission decreases in time [11], [17].

## 2.2 Z-pinch Loads

### 2.2.1 Single Planar Wire Arrays

One form of wire array is the single planar wire array (SPWA), which consists of a number of wires (typically of micron scale thickness) separated by some interwire

separation distance (typically on a mm scale) arranged in a linear row. The planar wire array (PWA) style load was first developed at UNR, and has shown unique implosion capabilities, and have proven to be excellent radiators of x-rays [30].

### 2.2.2 Double Planar Wire Arrays

Double planar wire arrays (DPWAs) are very similar in structure to SPWAs in that they are, conceptually, made up of two SPWAs placed some distance apart in parallel orientation to each other; this distance is known as the interplanar gap (see Figure 1). It was found in ref. [25] that the implosion dynamics of DPWAs are strongly dependent upon the Aspect Ratio (φ) which is defined as the ratio of the planar width (PW) to the interplanar gap (IPG).

$$\varphi = \frac{PW}{IPG}$$

Equation 1

The DPWA, as a load type, has been shown to be both a compact load design, and an excellent radiation source. The current distribution between the wires has been shown to be similar to that of SPWAs; with a larger portion of the current being distributed initially to the outermost wires (farthest from the load center) of the load, and the innermost wires getting less [31], this causes the outermost wires to ablate sooner during the ablation phase of the pinch. These outermost wires, ablating sooner than the innermost wires are large contributors to the formation of the precursor column, which, as described in Section 2.1.4, compresses during the stagnation phase, producing a large x-ray burst. This implosion dynamic, unique to the DPWA, is a contributing factor to the DPWA being the highest

producer of x-rays, amongst planar wire arrays tested on the UNR Zebra generator [24], [25].

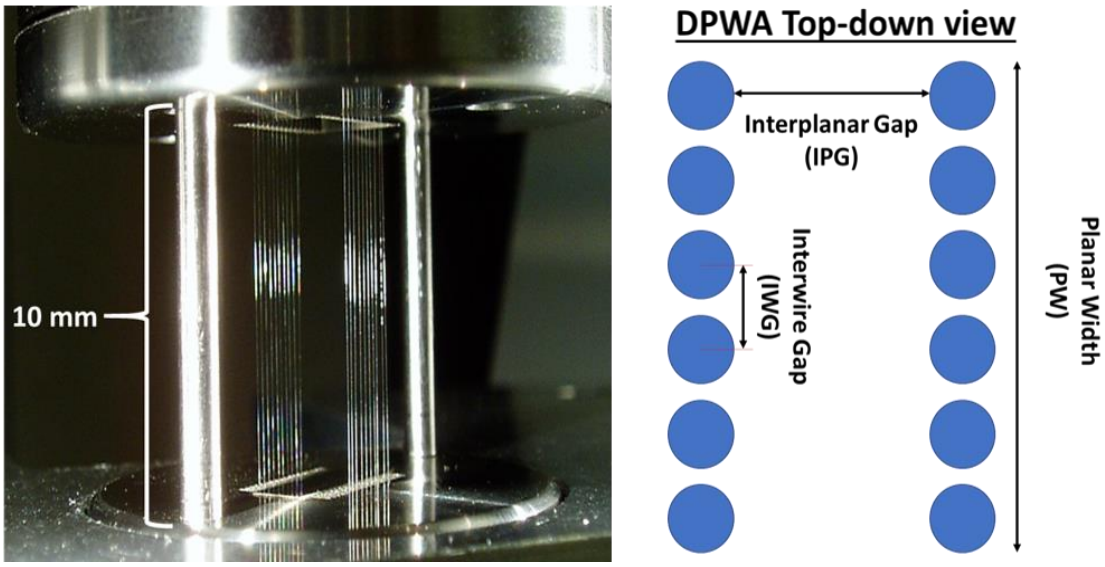


Figure 1: A picture of a double planar wire array (DPWA) is shown on the left, and a top-down sketch of a 6 x 6 DPWA is shown on the right. Note the Interwire Gap (IWG), Interplanar Gap (IPG), and Planar Width (PW), as these are all important measurement that determine the aspect ratio, and thus the implosion dynamics, of the load.

Due to the x-ray emission efficiency and large x-ray production capabilities of DPWAs, they were an ideal candidate for study on both the UNR Zebra generator as well as the UM MAIZE LTD. The study of DPWAs of various materials, from low- to mid- to high-atomic numbers, on both machines is a primary focus of this work, and is discussed in detail in Section 4.

### 2.2.3 Other Important Wire Arrays

Although not heavily addressed in this work, any discussion of wire array Z-pinches would be incomplete without describing both X-pinches and cylindrical wire arrays. Both

are incredibly important for ongoing research at both the university level and at national labs [32], [33].

#### *2.2.3.1 X-pinches*

X-pinches are a form of z-pinch loads in which wires are cross-connected between the anode and cathode to form an "X" shape. Experiments with X-pinches on the UNR Zebra machine were composed of either 2 or 4 crossed wires making for an area of heavier mass concentration at the center of the array where the wires cross. During the pinch, this crossing point creates a very hot, dense plasma (more so than the other areas of the load). This area is the primary source of x-ray radiation from the x-pinch [32], [33]. These x-pinch loads are useful when a small, concentrated source of x-rays desired.

#### *2.2.3.2 Cylindrical Wire Arrays*

Cylindrical wire arrays consist of an array of wires in a circular pattern. The number of wires that make up the cylindrical array can be as low as 16, for smaller devices, to 100+ at larger machines. These arrays create a very uniform central plasma, as the stream of mass from the wires is very symmetrical. These arrays are also useful for compressing a central material, such as foam or a gas hohlraum. Some cylindrical wire arrays include another cylindrical wire array placed inside another. These are known as nested cylindrical wire arrays [34].

### 2.2.4 Foil Liners

Foil Liner loads are very similar to wire array loads; however, the wire configurations are transformed into continuous foils of micron scale thickness. As a possible alternative to PWAs and CWAs on future >30-MA generators, Planar Foil Liners (PFLs, see Figure 2) have been proposed. The continuous foil load is thought to be a useful

replacement for discrete wires at >30-MA current levels because when the CWAs and/or PWAs are scaled to such currents, the interwire gap spacing decreases, and the coronal plasma surrounding each individual wire expands and significantly overlaps with the coronal plasmas from neighboring wires [35]. Previously, encouraging results with Double Planar Foil Liners (DPFLs, see Figure 2) were obtained in experiments using the high-impedance UNR Zebra generator [12, 13], where it was found that the Al DPFL electron temperature ($T_e$), electron density ($n_e$), and x-ray yield were comparable to Al DPWAs with similar mass. However, almost no data on DPFL x-ray sources have been collected on low-impedance drivers, such as a single-cavity Linear Transformer Driver (LTD). As a result, very little is known about the implosion and radiative performance of these load types on low-impedance drivers.

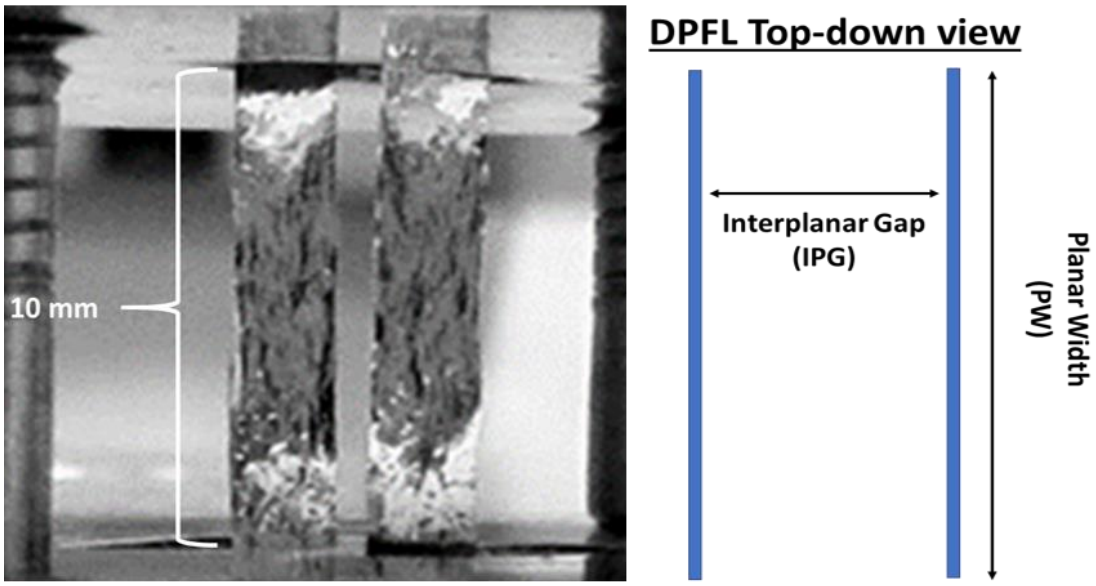


Figure 2: A picture of a double planar foil liner (DPFL) is shown on the left, and a top-down sketch of a DPFL is shown on the right. Note the Interplanar Gap (IPG) and Planar Width (PW), as these measurements determine the aspect ratio of the DPFL.

# 3 Experimental and Theoretical Techniques

The experiments in this work were performed with a variety of pulsed power devices and diagnostics. This section discusses the UNR Zebra generator, the UM MAIZE LTD, and the UNR Sparky-HXRS, as well as the numerous experimental diagnostics (both physical and theoretical models) used to collect and interpret the data.

## 3.1 Overview of The MAIZE LTD and Zebra Marx bank Pulsed Power Machines

### 3.1.1 The UNR Zebra Marx Bank Generator

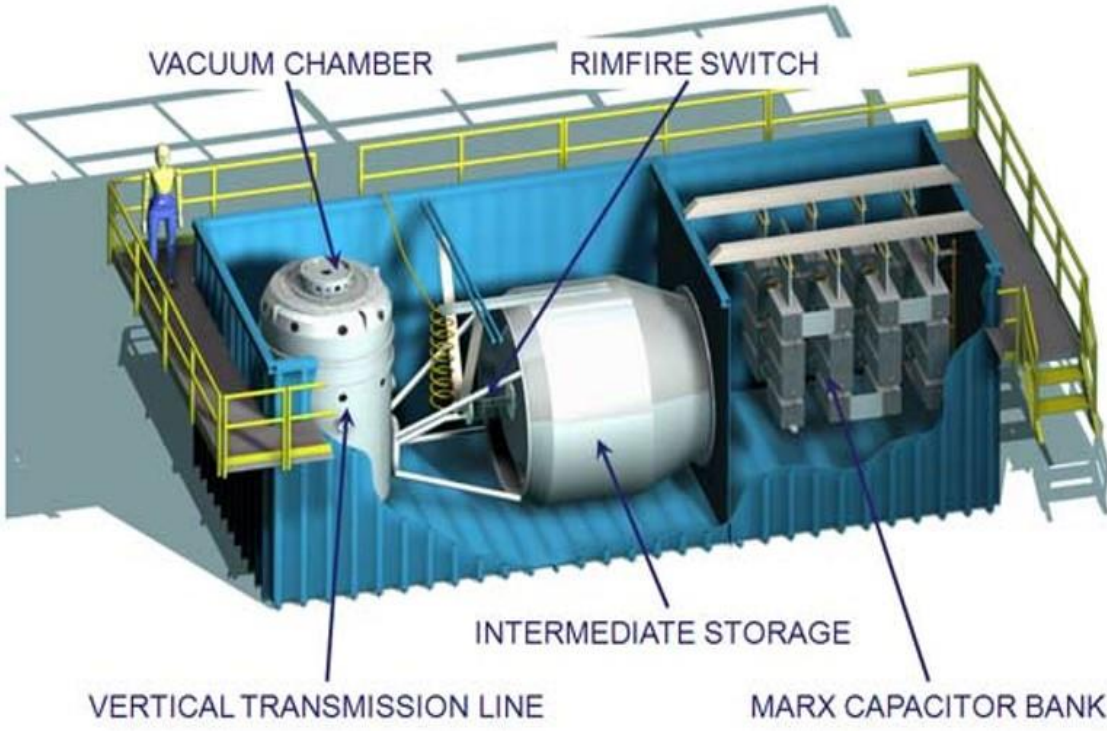


Figure 3: Cutaway cartoon image of the Zebra Marx Bank pulsed power generator. Image courtesy of **https://www.unr.edu/ntf/facility/zebra**.

The Zebra pulsed power generator is a high-current university-scale Marx Bank generator located at the University of Nevada, Reno's Zebra Pulsed Power Lab (formerly known as the "Nevada Terawatt Facility"). The UNR Zebra generator uses a Marx bank of capacitors (see Figure 3) which stores about 150 kJ of energy, which is released into a current carrying load with a maximum current of 1 MA and a 100 ns current rise-time [14-15].

The Zebra generator operates by first charging up the capacitor bank (consisting of thirty-two 1.3 μF capacitors in parallel) to a maximum of 100 kV, though the capacitor bank is usually restricted to 85 kV in operation to ensure the machine is not damaged during operation. Once the bank is charged, the capacitor bank is then discharged in series into an intermediate storage capacitor (28 nF, 3.5 MV). Once the intermediate storage capacitor has reached 80% charge, the capacitor is discharged by a gas $SF_6$ insulated Rimfire switch, into the transmission line. This machine has a high-impedance of 1.9 Ω, which is responsible for the high-impedance of the Zebra generator. The current is then distributed to/through the load, reaching the anode and flowing through the load to the cathode and the walls of the chamber, to ultimately discharge through the return current paths. As described in Section 2, this large current quickly flowing through the load creates a plasma, and ultimately a Z-pinch due to the **J** x **B** forces generated by the current. For the Zebra generator, the high energy implosion creates a large amount of debris throughout the pinching process. For this reason, diagnostics are typically placed at least 1 m from the center of the chamber (see Figure 4).

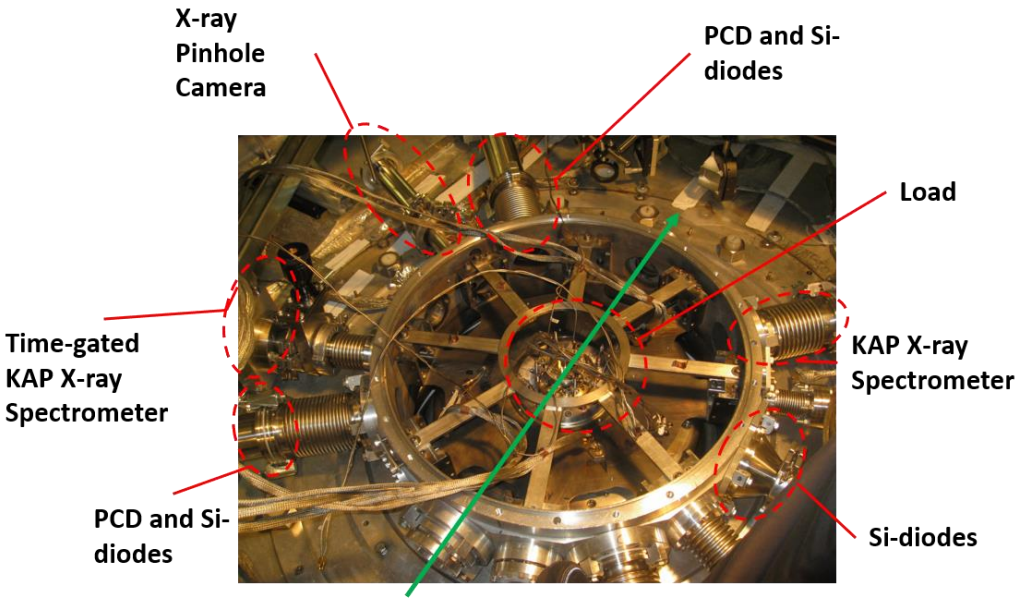


Figure 4: Zebra Vacuum/Diagnostic Chamber with diagnostic labelled.

#### *3.1.1.1 The Load Current Multiplier*

The Load Current Multiplier (or "LCM") was an addition, custom built for the Zebra machine and implemented in 2007-2010 [16-17]. The LCM implemented on the Zebra generator increased the Zebra current from 1 MA to up to 1.7 MA, without significant modification to the machine [40]. This feat is accomplished by minimizing the inductance mismatching that limits the energy transfer efficiency when the machine is in its standard configuration (ie: without the LCM). When the LCM is applied, the anode is replaced by two concentric toroids, and the generator current flows into the LCM along the inner surface of the largest electrode, where it, in turn, induces an opposite current in the opposing electrode. The induced current and generator current are then combined at the convolute, which increases the overall current. In the case of the Zebra LCM, the current

is nearly doubled, but this technique can be used for higher multiples of the current as well [39].

### 3.1.2 The UM MAIZE LTD Generator

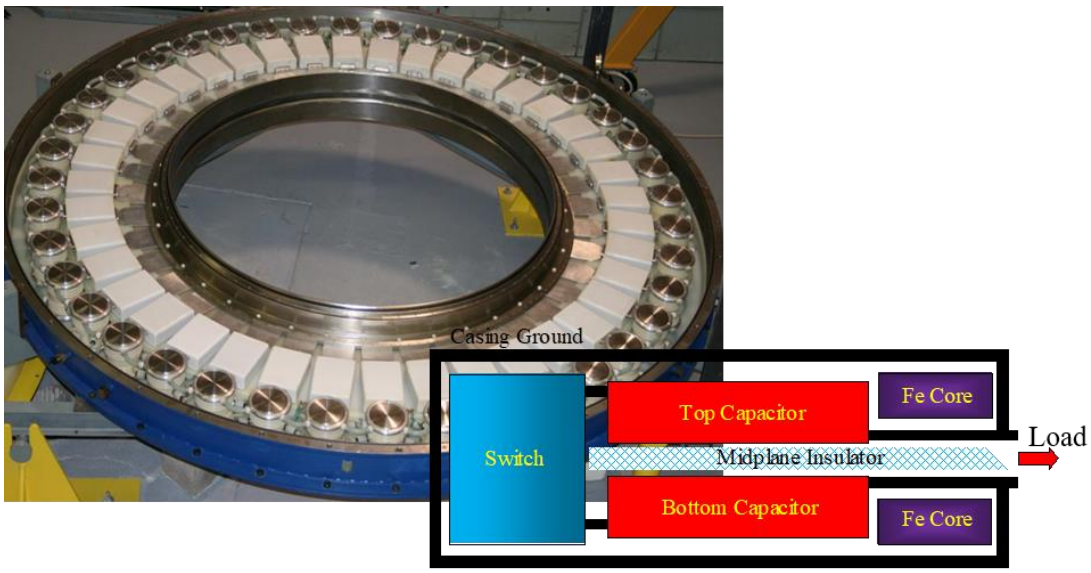


Figure 5: Image of the Capacitor Bank Cavity of the MAIZE LTD, and Capacitor Brick diagram. Figure courtesy of University of Michigan Plasma, Pulsed Power, and Microwave Laboratory. Retrieved from https://plasmabay.engin.umich.edu/research/michigan-accelerator-for-inductive-z-pinch-experiments-maize/ and ref. [7].

The MAIZE machine consists of a single-stage low-impedance (0.1 Ω) LTD cavity, capable of driving up to 1 MA of current with 100 ns risetime into an impedance matched, non-inductive load. However, for the loads imploded in this work, the peak current was in the range of 500-600 kA with a risetime of approximately 250 ns. The generator cavity contains 40 bricks, with each brick consisting of two capacitors charged to opposite polarities connected in series to a six-gap, sequence multi-electrode spark-gap switch (see Figure 5). At the center of the MAIZE cavity is the vacuum/diagnostic chamber, a 1 m in

diameter chamber which houses the load in the center, with room surrounding it for diagnostics, and surrounded by viewing windows for external diagnostics (see Figure 6). The current is measured by taking the average of four B-dot current measurements, located azimuthally symmetrically around the chamber. Detailed discussions of the operation of the MAIZE LTD are featured in refs. [7], [41]–[43].

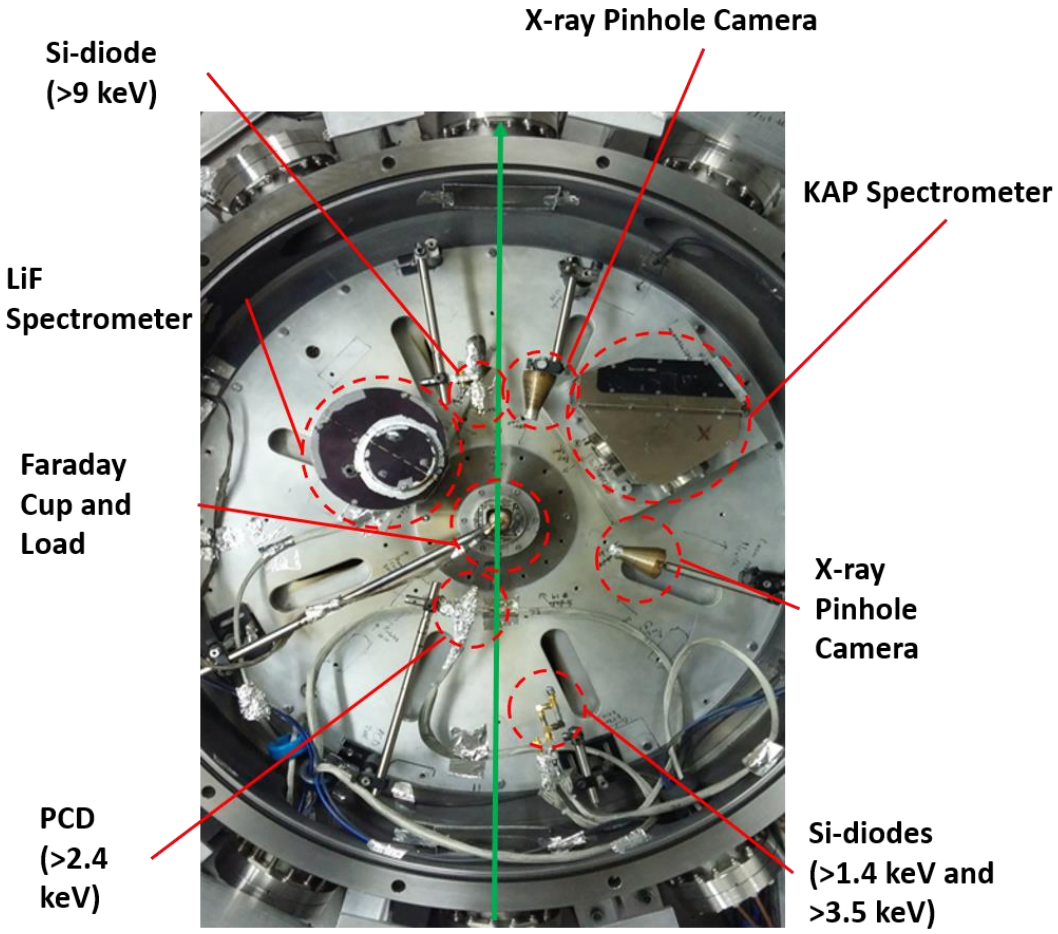


Figure 6: Image of the MAIZE LTD Vacuum/Diagnostic Chamber with diagnostic labelled.

## 3.2 The Tabletop Sparky-HXRS

The Sparky hard x-ray source (Sparky-HXRS) is a low-current tabletop x-ray source developed at UNR. Sparky-HXRS was operated in two modes: First Configuration (FC) which used a bank of six 12 nF capacitors connected in parallel and was charged to a maximum voltage of 27 kV, and Second Configuration (SC) which used a single 0.6 nF capacitor charged to a maximum of 23 kV as the energy storage source. The discharge was triggered by a pulsed Nd:YAG laser beam focused on a planar slab cathode. The anode was placed above the cathode (8 mm gap between the electrodes), and the laser induced plasma from the cathode and subsequent electron beam, makes contact with the anode, causing the stored current to flow between the electrodes. This causes a “cold” plasma to form on the anode surface, as a result of the electron beam and micropinch, which radiates characteristic hard x-rays from the anode, and the micropinch that forms lower in the discharge plasma area radiates mainly in the softer x-ray region. As the development and characterization of the Sparky-HXRS machine was a large part of this dissertation, a larger discussion of this machine will be given in Section 5.

Figure 7: Sparky-HXRS in Second Configuration with Faraday cage.

## 3.3 Diagnostic Overview

Diagnostics are the essence of experimental physics, as they are the tools used to measure, model, and ultimately understand the physics being demonstrated throughout an experiment. For the experiments covered in this dissertation, the diagnostics used have been broken down into four main subcategories: Current Diagnostics, which are important to measure, as the current peak and risetime are incredibly important in the creation of experimental plasmas and have a direct effect on the conditions of the plasma created; Optical and Laser Based Diagnostics, which are useful in imaging the created plasmas; X-

ray Diagnostics, the broadest category, and the lifeblood of these particular studies, as they measure all manner of x-ray radiation emitted by the plasma during and throughout the pinching process, and whose measurements can be used to categorize the plasma; Electron Beam Diagnostics, which are used to measure and estimate the electron beams generated by the production of the plasma; and lastly, Theoretical Diagnostics/Modelling, which are extremely useful, and often necessary, to interpret measurements made by the experimental diagnostics and, through use of physical principles and equations, analyze the plasma characteristics. Many of the diagnostics discussed in this section (in most cases the exact same diagnostics) were used in experiments on all three machines: Zebra, MAIZE, and Sparky-HXRS.

### 3.3.1 Current Diagnostics

#### *3.3.1.1 Rogowski Coil*

The Rogowski Coil was named for Walter Rogowski, who first wrote about the diagnostic in ref. [44]. The diagnostic uses the principle of electromagnetic induction to measure alternating currents. This is done by placing a Rogowski Coil, made up of a closed loop toroid that encircles the current carrying medium and connects to a signal measuring device (in this work, an oscilloscope). The current changing in the current carrying medium induces an electromotive force current in the Rogowski Coil, which then appears as a signal on the oscilloscope. The voltage signal induced in the Rogowski Coil is given by Equation 2:

$$v(t) = \frac{-AN\mu_0}{l}\frac{dI(t)}{dt},$$

Equation 2

where *v(t)* is the voltage induced, *A* is the area of the small loops, *N* is the number of turns (loops), $l$ is the circumference of the Rogowski Coil, $\mu_0$ is the permeability of free space (also known as the "magnetic constant"), and $\frac{dI(t)}{dt}$ is the rate of change of the current in the current carrying medium being measured. Due to the low inductance of the Rogowski Coil, it is extremely sensitive to even small changes in current. This equation can be manipulated to derive the current in the current carrying medium as follows:

$$I(t) = \frac{-l}{AN\mu_0}\int v(t)\,dt$$

Equation 3

For the purposes of this work, Equation 3 was used to estimate the current in Sparky-HXRS, where $l = 0.08\pi\ m$, $N = 250\ turns$, and $A \cong 2 * 10^{-5}\ m^2$.

#### *3.3.1.2 B-dot Sensors*

Magnetic pickup loops (often colloquially referred to as "B-Dot sensors/probes") are used in many university-scale (<10 kA scale) pulsed power devices to measure the current. In many cases, the transmission line of these larger pulsed power devices is not conducive (either through physical limitations, or through the magnitude and timing of the current changes) to the use of a Rogowski coil. B-dots, however, are small inductive loops that can be placed withing the vacuum chamber without requiring many (or any) modifications to the chamber. Unlike the Rogowski Coil, which utilizes the change in

current to generate an EMF in the line, the B-dot utilizes the change in magnetic field to induce a current in the sensor. As the load implodes at the center of the chamber, the current flowing through the load generates a magnetic field; the loops of the B-dot sensors are placed perpendicularly to the load current direction (such that the magnetic field lines will flow through the interior of the B-dot coils) which then generates the signal.

Experiments on Zebra featured five B-dots (four placed azimuthally symmetrically around the chamber and another placed nearer to the load), while MAIZE features four azimuthally symmetrically placed B-dots around the chamber. In both cases, the signal generated with the B-dots is averaged over all signals to yield the most accurate representation of the current flowing through the load. The placement of the B-dot sensors can also provide valuable information about the conditions of the shot (ie. if one signal is much higher than the others, then there may have been arcing in the transmission line, leading to less current and energy being deposited into the load).

### 3.3.2 Optical and Laser Based Diagnostics

#### *3.3.2.1 Laser Shadowgraphy and Self-emission imaging*

Laser Shadowgraphy is a technique used to image dense plasmas, in which a laser beam is collimated and shined through a plasma, where the laser light is absorbed and refracted, and the light that passes through is then imaged by a camera. This technique is similar to, and can be thought of as an advanced method of shadow-puppetry. The image on the camera reveals the structure of the plasma, as the denser parts of the plasma will have absorbed and refracted more of the laser light than less dense areas. Although beyond the scope of this work, as shadowgraphy was only used as a means of imaging the plasma, this technique can also be used to estimate the density of the plasma. However, this

involves solving the Poisson equation with suitable boundary conditions, given that shadowgraphy is a second derivate of density [45].

For experiments at the UNR Zebra facility, an Nd:YAG laser fires a 150 ps, 532 nm pulse. The critical density of a 532 nm laser beam is $3.9 \times 10^{21}$ $cm^{-3}$, meaning that plasmas with an electron density that exceed this density cause a complete shadow. Many of the plasmas in this work are on the order of $10^{19}$-$10^{20}$ $cm^{-3}$, not enough to completely block out the laser, but significant enough to block out a large majority of the incoming laser light. The laser is triggered in unison with the Zebra current pulse, therefore, in order to image the plasma at different times throughout the pinch, varying lengths of cable are added to the triggering system, which prevents the triggering pulse from reaching the laser and camera too early.

Prior to entering the Zebra diagnostic/vacuum chamber, the laser pulse passes through a beam splitter, where the beam is split into two separate beams. One of the beams continues into the chamber and passes through the plasma; the other beam is sent through a separate optical path (which takes the beam 5 ns to go through) before ultimately returning to the original beam pass and continuing on through the plasma. The two pulses are now 5 ns apart from each other, and, having passed through a beam splitter, are now orthogonally polarized, which is useful as the beam paths are now separated using optical polarizers to send the beams into two different CCD cameras, resulting in two shadowgraphy images with a 5 ns difference in time. For a high-impedance machine like the Zebra generator, the implosion dynamics of loads are highly repeatable, and therefore, the images from several shots with identical loads are often “stitched” together, to image the implosion at many different times throughout the implosion.

At the UM MAIZE LTD facility, a frequency-doubled Nd:YAG laser fires a 2 ns, 532 nm pulse to serve as a laser backlighter for the shadowgraphy images. This pulse was then sent through and optical path, in which the beam was sent through a beam splitter; one part of the beam continues on, and the other part of the beam is sent into a repeating beam path, which takes 10 ns, before ultimately leading the beam back through the beam splitter [46]. These pulses pass through the plasma and are imaged on a 12-frame intensified CCD camera, gated at 10 ns. Ultimately, you get 12 images, 10 ns apart, all from the same shot, which is very useful as the implosion dynamics are less repeatable on low-inductance machines like the MAIZE LTD (however, shots on the MAIZE LTD are still quite repeatable, see Section 4.5).

The 12-frame intensified CCD camera was also used to take self-emission images of the implosion (see, for example, Figure 14, Figure 15, and Figure 16), in which only the light emitted by the plasma was detected by the camera. Previous experiments using cylindrical foil liners on MAIZE showed only small variations in the observation of the plasma-vacuum boundary between self-emission and laser-backlit shots [35-36].

### 3.3.3 X-ray Diagnostics

#### *3.3.3.1 X-ray Filters*

X-ray filters are used to prevent x-ray detectors from measuring photons below a certain x-ray cutoff energy. As x-ray photons pass through a material, the photons can interact with that material in a number of different ways, which ultimately attenuates the strength of the beam of x-ray radiation. In plasmas, when studying higher energy photons, often lower energy photons (in the visible or UV range) are generated and can artificially "inflate" the desired signal measurement. Filters are useful in filtering out a significant

amount of these lower energy undesirable photons. The transmission coefficient (T) of a filter is determined by the following equation:

$$T = e^{-n\sigma d}$$

Equation 4

where $d$ is the thickness of the material, $n$ is the number density of atoms, and σ is the cross-section of photoabsorption and scattering of the material [49].

For this work, the term "cut-off energy" will be used to refer to the energy at which a photon above this energy will see greater than 1/e (or >36.8%) transmission, and anything below that energy will see below 1/e transmission rate (or <36.8%). For a list of the materials, thickness, and cut-off energies used in this work, see Table 1. For sake of simplicity, in this work a diode will often be referred to by its cut-off energy. For example, a diode featuring an x-ray filter with a >1.4 keV cut-off energy, will often be referred to as "the 1.4 keV diode."

| Filter Material and Thickness | Cut-Off Energy (keV) |
|---|---|
| 8 µm Be | 0.75 |
| 7.5 µm Kapton | 1.4 |
| 6 µm Mylar + 0.2 µm Al coating | 1.4 |
| 25 µm Kapton + 4 µm Mylar + 0.8 µm Al coating | 2.4 |
| 12.4 µm Ti | 3.5 |
| 90 µm Al | 8.2 |
| 120 µm Al | 9 |
| 560 µm Al | 15 |

Table 1: A list of all the filter used on diagnostics in this work. Filter material, thickness, and cut-off energy are listed, where the cut-off energy is defined as the 1/e transmission rate of photon beam intensity.

#### *3.3.3.2 Silicon Photodiodes*

The silicon photodiode detector (sometimes shortened to Si-diode or SiD, in this work) is a primary diagnostic in this work. The Si-diode is useful for recording the time-history of radiation in a selected filtered x-ray band (ie: greater than the filtered cut-off energy). For this work covering experiments on Zebra, MAIZE, and Sparky-HXRS, two types of Si-diodes were used: AXUV HS-1 and HS-5 photodiodes. These photodiodes provide both spatially and spectrally integrated, time-resolved x-ray flux measurements.

These detectors have a 3-7 nm thin $SiO_2$ surface layer, which is penetrated by incident photons that produces electron-hole pairs across the p-n junction within the diode, and then creates a current proportional to the number of incident photons. The signal generated is read on an oscilloscope, where it can then be used to estimate the number of incident photons.

The diodes, AXUV HS-1 and HS-5, are both produced by Opto Diode Corp., and share many similarities. Their fundamental differences are in their detecting area size, and internal capacitance (leading to signal current rise time). The HS-1 diode has a 0.25 x 0.25 $mm^2$ detecting area, 5 pF capacitance, and a 250 ps rise time, while the HS-5 diode has a larger detecting area of 1 $mm^2$, 40 pF capacitance, and 700 ps rise time [50], [51]. With such a fast response time, these detectors are ideal for detecting even very short (ns scale) radiation signals. In addition, these Si-diodes have a nearly 100% quantum efficiency over a large array of spectral regions with very little, if any, energy lost in the creation of the electron-hole pair [52], [53]. These Si-diodes are also very accurate, with a flat response to each photon detected, with one photon creating one charge [54]. These Si-diodes are operated with -45 V bias voltage in all applications in this work.

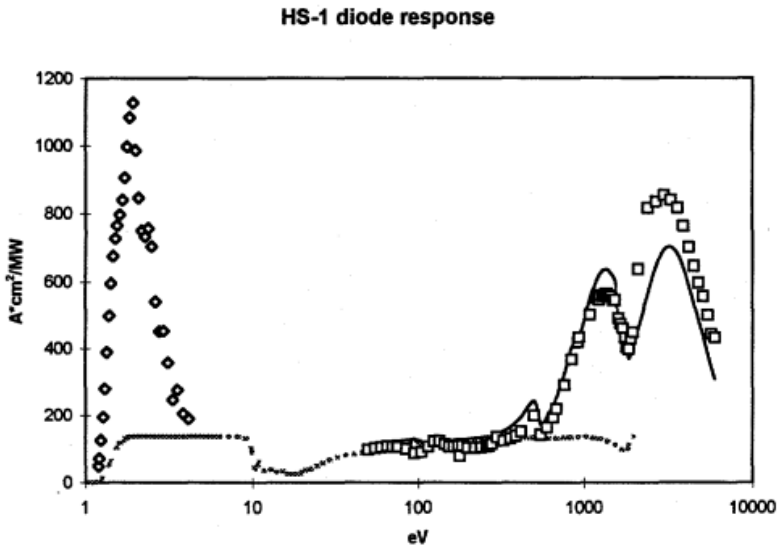


Figure 8: HS-1 silicon diode spectral response. (Fig. 4 from ref. [55])

As can be seen in Figure 8, the photon response of these diodes is not flat in the soft (<1 keV) x-ray region, however, all of the research in this work is filtered at >1.4 keV and above, so this is not an issue. The Si-diodes are also sensitive to particles with high energy (>100 keV), so, where appropriate, the Si-diodes were placed far enough from the plasma to avoid interactions with any electron or ions beams, and, in cases when this could not be done (ie: when the x-ray radiation signal was too weak to be detected at a safe enough distance to avoid energetic beams) strong permanent magnets were placed in front of the diodes to shield them from the energetic particles.

#### *3.3.3.3 Polycrystalline Diamond Detector*

Polycrystalline Diamond Detectors (also called PCDs, and sometimes "Photoconducting Diamond Detectors") are another form of x-ray detecting diodes [56], [57]. However, unlike the Si-diodes, they do not measure photoelectrons, but rather the

incident x-ray flux produces a current [58]. The PCDs also have a fast response time of 500 ps [59], making them ideal to study even very short x-ray signals. The PCD holds a number of distinct advantages over Si-diodes. The first is that they have a flat spectral response over a wide spectral region in an even softer x-ray region (200-2200 eV) [60]. The other distinct advantage is their ability to be absolutely calibrated, as described in ref. [59], which allows for an incredibly accurate measurement of x-rays detected. The induced current is given by

$$I = \frac{1}{13} P_{in}(1 - e^{-\alpha d}) \frac{\mu T V_{Bias}}{l^2},$$

Equation 5

where $P_{in}$ is the incident power, $\alpha$ is the absorption coefficient, $\mu$ is the charge carrier mobility, $d$ is the thickness of the diamond within the detector, $T$ is lifetime of the charge carriers, $V_{Bias}$ is the bias voltage applied to the PCD (in this work, it was always -100 V), and $l$ is the conduction length of the diamond. All PCDs used in this work were absolutely calibrated, with sensitivities on the order of $10^{-4}$ A/W.

As mentioned, with the PCDs being absolutely calibrated, we can get an accurate measurement of the total x-ray energy emitted in the filtered band (PCD signals discussed in this work were filtered at >2.4 keV and >8 keV). This is done by integrating the signals from the absolutely calibrated PCD over the entire duration of emission and assuming isotropic radiation into 4π steradians, by the following equation,

$$E_{tot} = \frac{4\pi \int V_{PCD} dt}{RSE_{laser}\Omega},$$

Equation 6

where 4π comes from integrating over a sphere (all space), $V_{PCD}$ is the voltage signal detected by the oscilloscope, $R$ is the resistance of the oscilloscope channel, $S$ is the sensitivity of the PCD, and $\Omega$ is the solid angle of the detector. This measurement is useful in determining the efficiency of a load type (both material and design, or in the case of Sparky-HXRS, the anode and cathode combination) on a given machine. This is typically expressed using the coefficient of conversion $\varepsilon$ (Equation 7), which is defined as the ratio of the energy emitted by the plasma ($E_{tot}$) compared to the energy in the machine capacitors ($E_{cap}$),

$$\varepsilon = \frac{E_{tot}}{E_{cap}}.$$

Equation 7

This same method is used to measure the efficiency of other kinds of plasma as well. For example, for a laser produced plasma, you would simply replace $E_{cap}$ with the $E_{laser}$ (the energy of the laser).

For experiments with Sparky-HXRS, the total energy in the >8 keV region was measured and, by integrating the signals on the cross-calibrated Si-diodes in conjunction, this was used to estimate the number of photons in the >8 keV band.

#### *3.3.3.4 Scintillation Detectors*

Scintillation detectors are extremely sensitive x-ray detecting sensors which can record the time history of x-ray emission. The scintillation detectors used in this work

consisted of a Pilot 102 plastic scintillator (50 mm diameter, 20 mm thickness) and an R 928 Hamamatsu fast photomultiplier tube. For this work, the scintillation detectors were implemented on the Sparky-HXRS machine to detect x-rays photons outside of the chamber, in the place that would eventually be taken up by the spectropolarimeter. They were filtered with either an >8.2 keV filter or >15 keV filter made of Al foils. As these are incredibly sensitive detectors, the scintillation detectors used on Sparky-HXRS were shielded with an 8 mm thick W plate placed between the detector and the vacuum chamber (also, testing with the scintillation detector prompted the installation of a Faraday cage around the capacitor bank, as that lowered the noise level on the detector signal).

The high sensitivity of this detector is due to two aspects: the large detector area, and the photomultiplier tube. The large detecting surface allows for more photons to be collected at the detector surface. The photomultiplier tube uses a series of dynodes to increase the initial signal. When an x-ray photon hits the detector surface (a photocathode) electrons are produced, the electrons then travel through a focusing electrode which focusses them on the first dynode. Each dynode is held at a chosen voltage, and when electrons hit the dynode, more electrons are produced, which then move on to the next dynode, on and on until finally reaching the final anode, which then leads to a set of connecting pins that connect the photomultiplier to the signal carrying line. This process allows for very faint signals (very low levels of x-ray photons) to be detected and a larger signal to be analyzed.

#### *3.3.3.5 X-ray Pinhole Cameras*

One of the imaging diagnostics fielded in this work is time-integrated x-ray pinhole cameras (abbreviated as TIPHs). These small cameras provide a compact way to image

plasmas in a broad range of spectral regions by way of x-ray filters. Each camera fielded had three pinholes filtered at different x-ray regions (in this work, the filters used were >0.7 keV, >1.4 keV, and >3.5 keV), meaning each camera was capable of taking three images on each shot. The "detector" used in these cameras was a Kodak Bio-max MS film.

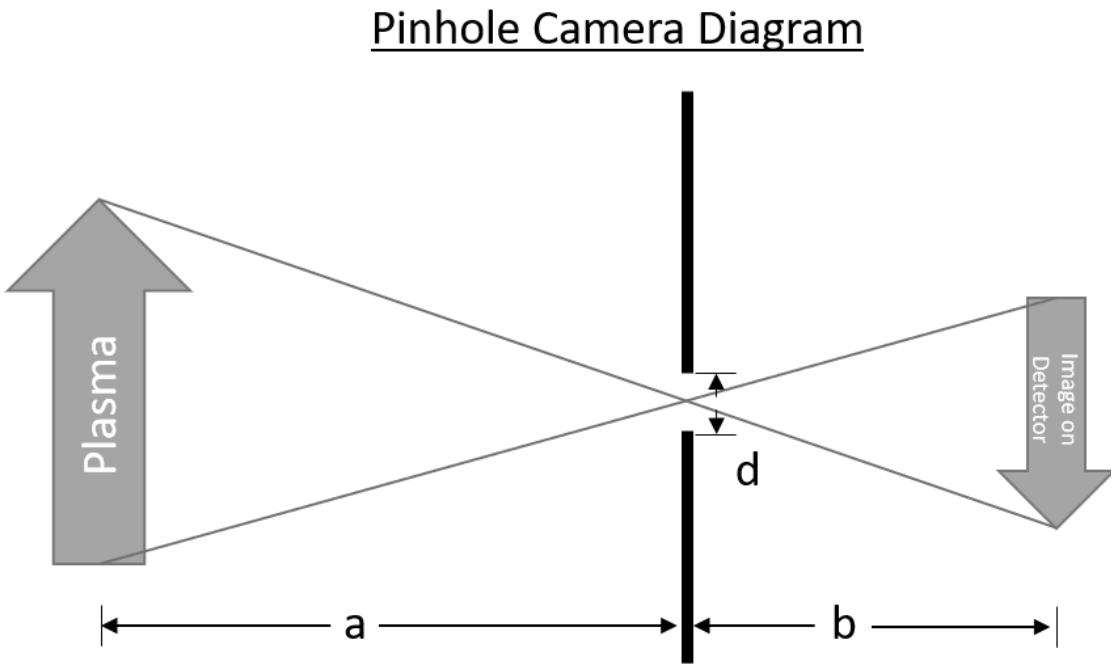


Figure 9: A basic diagram of the pinhole camera scaling. "a" is the distance from the plasma to the pinhole; "b" is the distance from the pinhole to the imaging detector; and "d" is the size of the pinhole itself.

The compact nature of these TIPHs allow us to put the cameras as close to the plasma as necessary; however, while the distance can affect the magnitude of x-rays incident on the detector, the distance has a direct effect on the size of the pinhole image. In fact, the magnification and resolution of the images recorded on the TIPHs depends on three factors: the distance from the plasma source to the pinhole, *a*; the distance from the

pinhole to the detector (film), *b*; and the size of the pinhole itself, *d* (see Figure 9). The magnification (Γ) is given by

$$\Gamma = \frac{b}{a},$$

Equation 8

while the spectral resolution (Δl) is given by

$$\Delta l = d\left(1 + \frac{a}{b}\right).$$

Equation 9

There is a special case in which the wavelength of the radiation is not much less than *d*, in which the diffraction-limited resolution ($l_r$),

$$l_R = 1.22\lambda\frac{a}{d},$$

Equation 10

must be considered. In this case, the full resolution ($\Delta l_{combined}$) of the TIPH becomes,

$$\Delta l_{combined} = \sqrt{\Delta l^2 + l_R^2}.$$

Equation 11

#### *3.3.3.6 Time-integrated X-ray Spectrometers*

A vital diagnostic in the study of plasma physics is the spectrometer, which uses some medium (in this work, that medium was a crystal) to refract the spectra in different angles (based on the photons energy and wavelength), and study the individual spectral

lines. Up to now, in this dissertation, all x-ray detectors were studied with x-ray filters, which only allows for the study of x-rays above the cutoff energy of the filter. With spectrometers, however, the splitting of the spectra by the crystal allows for single spectral lines (photons of like wavelength and energy) to be measured and studied. The incoming spectra is refracted according to Bragg's Law

$$2dsin\theta = m\lambda,$$

Equation 12

where $d$ is the atomic interplanar spacing of the crystal lattice, $\theta$ is the incident angle of the radiation on the crystal, $m$ is the order of the diffraction, and $\lambda$ is the wavelength of the incident photon (see Figure 10). Given these parameters, in order to prepare the spectrometer for experiments we must know what range of x-ray wavelengths ($\lambda$) we are interested in studying, which will determine what kind of crystal will be used (the crystal determines $d$), and it will determine the angle ($\theta$) at which the crystal will be rotated with respect to the incident light from the plasma.

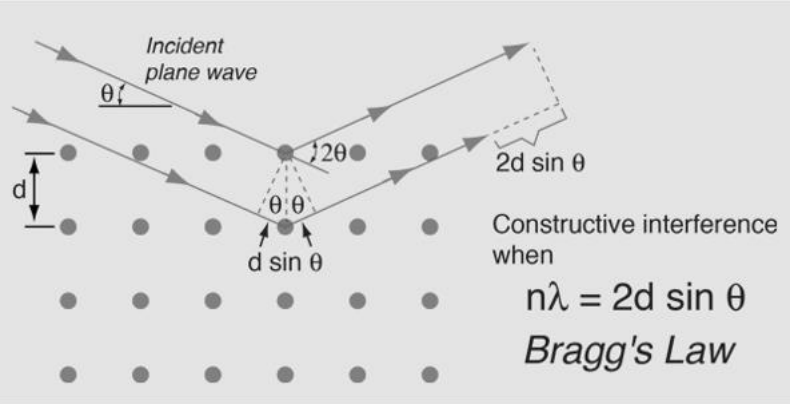


Figure 10: Illustration of Bragg's Law (image courtesy of ref. [61]).

Once the spectrum has been recorded by the detector (for this work, either on x-ray film or a CCD camera), the spectral lines recorded must be analyzed. See Section 3.3.5.2 for a comprehensive discussion of spectroscopic modelling.

For this work, the spectrometers used were convex crystal spectrometers, see Figure 11, which are popular spectrometer designs, due to their relative simplicity and flexibility in implementation. The crystal is bent around a convex holder, while the detector is Kodak Bio-max MS film. These spectrometers have a large spectral range, capable of detecting all wavelengths below '*2d*' from the Bragg Law [62]. The spectrometers in this work were outfitted with a variety of different crystals: a KAP (potassium acid phthalate) crystal was used to detect softer x-rays (between 4 and 13 Å); and a LiF (lithium fluoride) crystal for harder x-rays (between 1 and 2.4 Å). This spectrometer design was used in experiments on Zebra [63], MAIZE [26], [27], [64], and Sparky-HXRS.

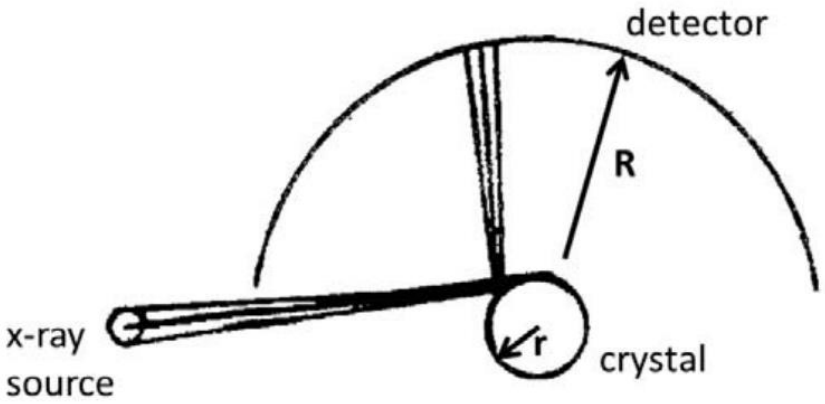


Figure 11: Schematic of a convex crystal spectrometer (image from Cooper 2016 [65]).

### *3.3.3.7 Time-Gated X-ray Spectrometers*

Time-Gated X-ray Spectrometers (TGSP) are very similar to the previously described time-integrated counterparts; however, they are outfitted with a microchannel plate (MCP). The MCP is fitted to the front of the spectrometer (facing the plasma) and cycles in time through a series of gold strips, which allows for time-resolved spectra to be recorded. The gold strips are triggered using a pulsed bias signal, in which the gold strips act as a photocathode. Incident photons are then converted to electrons and accelerated through plate capillaries, causing a plate capillary effect, where the electrons ultimately impact a phosphor screen, which again produces photons to be detected on the x-ray film (see Figure 12). This method also doesn't require a slit for the x-rays to enter the spectrometer; as the MCP strongly limits the exposure time, a slit would heavily inhibit the number of detectable photons. However, the tradeoff in removing the slit is that there is a loss in spatial resolution. Moreover, the MCP itself reduces the wavelength range of the detectable spectra.

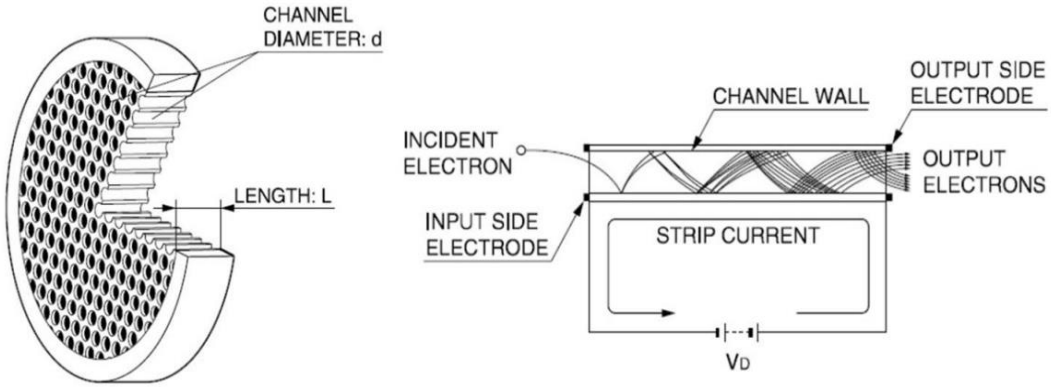


Figure 12: Basic diagram of an MCP detector (image from Chassela *et al.* 2019 [66]).

#### *3.3.3.8 Spectropolarimeters*

Spectropolarimeters are a useful tool in measuring the degree of polarization of x-ray spectra emitted from the plasma. A spectropolarimeter, to build upon what has already been written, can be thought of as being made up of two spectrometers placed perpendicular to each other (see Figure 13 for an example of the first spectropolarimeter developed by our group to study the polarization of x-rays emitted from X-pinch implosions on the Zebra generator [67]). The polarimeter is oriented with respect to the axis of symmetry, which, in our cases, is the axis in which the electron beam is generated. For the purposes of the work discussed in this dissertation, one crystal was always aligned parallel to the axis of symmetry to measure the intensity of the parallel aligned spectra ($I_{\perp}$), while the other crystal was aligned perpendicular to the axis of symmetry to measure the intensity of the perpendicular aligned spectra ($I_{\parallel}$). The measurement of the polarization of spectra under repeatable, controlled circumstances was one of the driving motivations behind the development of the Sparky-HXRS generator. Previous polarization measurements on the Zebra generator are discussed in refs. [33], [67].

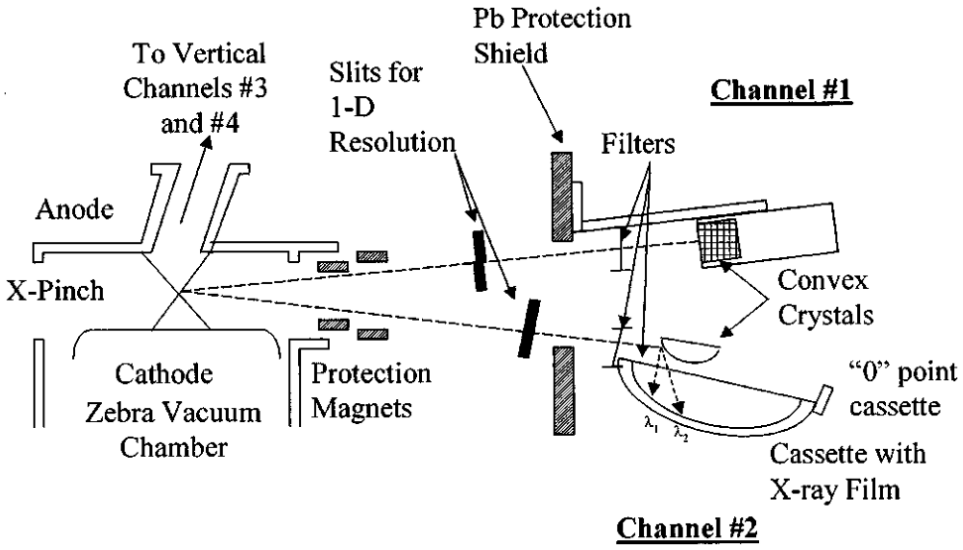


Figure 13: A cartoon model of the spectropolarimeter developed for the Zebra generator to study the polarization of X-pinch emissions, as an example of the basic form of a spectropolarimeter, from ref. [67]. As can be seen in the figure, both crystals (Crystals #1 and #2) record the same x-ray beam with the same line of sight. However, one crystal (Crystal #1) records the perpendicular ($I_{\perp}$) component and Crystal #2 records the parallel intensity component ($I_{\parallel}$), respectively, where the orientation is relative to the electron beam direction (or the axis of symmetry). In the all cases in this work (Zebra, MAIZE, and Sparky-HXRS), the axis of symmetry is the axis from anode to cathode, as that is the direction of the generation of the electron beam.

#### *3.3.3.9 X-ray CCD Cameras*

X-ray CCD cameras are imaging devices specially made to detect x-ray photons of specified energy ranges. Charge-coupled devices (or CCDs) use a thin plate composed of small, semi-conductor capacitors (which make up the pixels) that create a charge when a photon interacts with them. The CCD camera then creates an image based on the pixels' reaction to the oncoming photons. These CCD cameras are similar to a digital camera, in that they create a digital image based on the detection of photons on their imaging surface, however, CCDs are more accurate and, often, more sensitive than a typical digital camera,

this makes them ideal for use in scientific experiments, where precise measurements are needed.

The x-ray CCD camera used in this work was the high-sensitivity SOPHIA®-XO x-ray CCD from Teledyne Princeton Instruments [68]. The SOPHIA®-XO camera is sensitive to x-rays ranging from ~5 eV to 30 keV, and has a standard operating temperature in vacuum of -90° C. This camera was used on experiments with Sparky-HXRS to study Fe K-shell spectra (~6.4 - 7.1 keV), which was within the camera's sensitivity range, however, the camera was to be operated outside of the vacuum chamber, which meant that cooling it down to the proper temperature could, at atmosphere, cause damage to the CCD. For this reason, a special flange was created to affix to the front of the camera, and allow for dry nitrogen to be slowly pumped into the camera cavity during operation. The dry nitrogen would not cause damage to the CCD at low temperatures; however, the camera was only cooled to a temperature of -80° C, which proved to be just fine for the acquisition of our desired Fe K-shell spectra (see Section 5.4).

### 3.3.4 Electron Beam Diagnostics

#### *3.3.4.1 Faraday Cup*

Faraday cups are a useful diagnostic to measure the electron beam generation during a z-pinch. In experiments on Zebra and MAIZE, a Faraday cup was placed directly above the load to measure the electron beam generated by the z-pinch (see Figure 4 and Figure 6). In a z-pinch, the electron beam is generated upwards towards the anode and confined to a concentrated beam by the magnetic fields, but these diagnostics are also

useful in detecting electron beams generated in other plasmas as well, such as laser-irradiated gas puff experiments [69], as well of laser plasma foils [70].

The Faraday cup diagnostic itself is made up of a small metal disk that covers the end of a copper cup, which acts as a detecting surface. As electrons strike the detecting surface and generate a charge proportional to the number of incident electrons, the cup, which is connected to an oscilloscope through a cable and resistive network, generates a voltage signal which the oscilloscope can measure. The current generated in the circuit is then given by

$$I = \frac{Ne}{t},$$

Equation 13

where $I$ is the current (amperes), $N$ is the total number of incident electrons, $e$ is the charge of an electron ($1.69 \times 10^{-19}$ C), and $t$ is the observation time (seconds). Foil filters are placed in front of the detecting surface to filter electrons of different energies [71].

### 3.3.5 Theoretical Diagnostics/Modelling

#### *3.3.5.1 Wire Ablation Dynamics Model*

The Wire Ablation Dynamics Model (WADM) is used to theoretically model the implosion dynamics of different wire array loads. This information is crucial when planning wire array experiments on Zebra and MAIZE, as it can predict the performance of wire array implosions, such as the time of implosion, the velocity of the plasma, densities, energies, and other implosion dynamics, based on the design of the load, such as the wire material, thickness, number of wires, interplanar gap and interwire gap, and the current of the machine. This information is also useful in determining where to place

certain diagnostics to record the best possible data (and prevent potential damage to the diagnostics). The WADM was created to satisfy these experimental needs, as outlined by Esaulov *et al* [31], [72].

The WADM was used throughout the research in this dissertation (both in the planning phase of experiments and in the data processing phase) and features prominently in Section 4.10, discussing the radiative and implosion dynamics of brass DPWAs on the MAIZE generator.

The model works by first inputting the generator and load parameters. The load parameters include: the type of wire array (cylindrical, single planar, double planar, nested, etc.), the thickness of the wires, the total wire mass, the interplanar and interwire gap spacing, and the ablation rate coefficient, which is an intrinsic property of the wire material [31]. The model then calculates the inductive current distribution between the wires and the magnetic field contribution for each individual wire throughout the duration of the pinch. Each wire is taken to be an individual filament, where the model simulates ablated coronal plasma with kinetic energy and acceleration of each filament determined by the calculated magnetic field. The WADM is also capable of modelling mixed wire arrays (wire arrays made up of a mixture of different materials), as well as other useful information like the energy in the precursor region, the energy per length, and the current density, as well as other data that is beyond the scope of this dissertation.

#### *3.3.5.2 Spectroscopic Modelling*

Some of the most important diagnostics implemented in the experiments discussed in this dissertation is x-ray spectroscopy. However, measuring spectral lines means little without a means to analyze what those lines tell us about the plasma. The S-UNR code, a

spectral analysis code created by out theoretical group at UNR, provides a way to obtain the plasma parameters, electron temperature ($T_e$) and density ($n_e$), through the analysis of the collected spectral lines. The code operates by generating synthetic spectra based on the plasma conditions input into the code; the parameters and, in turn, the synthetic spectra are then modified until they best match the measured spectra.

Specifically, the S-UNR code is a Non-Local Thermodynamic Equilibrium (non-LTE) code. When a plasma is in LTE conditions, the rates of electron impact ionization and the corresponding reverse process, three-body recombination become equal. This typically only happens in plasmas of sufficiently high electron densities ($>10^{23}$ $cm^{-3}$), where the collisional effects dominate over the radiative effects. The plasmas in this work, however, reach electron densities on the order of $10^{19}$-$10^{20}$ $cm^{-3}$, so a non-LTE model is required. The basic principle of non-LTE modelling is determining the populations of different states for the various ions in a plasma by solving a system of equations that balance the populating of the states with the depopulating of the states through various atomic processes. Those processes are collisional excitation and de-excitation, radiative decay and resonant photo-absorption, collisional ionization and three body recombination, dielectronic recombination and Auger decay, and photoionization and radiative recombination. For the spectral models used in this work, the Flexible Atomic Code (FAC) [73] calculates the energy levels and atomic rates of the processes. These calculations are then used by the S-UNR code, which is adapted from an earlier version of the Spectroscopic Collisional-Radiative Atomic Model (SCRAM) first developed by Stephanie Hansen [74], and later modified by Nicholas Ouart [75] and Austin Stafford [76] to calculate the level

populations and generate synthetic spectra. The S-UNR model is discussed in detail in ref. [74], [75].

For this work in particular, K- and L-shell models were used. The K-shell models were applied to describe radiation from Al loads and L-shell models to analyze radiation from brass loads. K-shell radiation involves radiative transitions that end in the K-shell of the atomic levels, or the n=1 level. There are two types of transitions to be analyzed here. The first is ionic transitions in thermal plasmas, which comes from ions with very few remaining electrons, and they usually originate from relatively hot plasmas. The second are characteristic transitions from non-thermal plasmas, which occur in ions that are less ionized. This occurs when an electron in the K-shell gets excited to a higher level, mostly by non-thermal electron beams, causing a vacancy in the K-shell. This vacancy gets filled by an electron from a higher level dropping down to fill the K-shell vacancy, and a photon is emitted matching the difference in energy. This change in energy is characteristic to the element and energy levels, hence the name “characteristic radiation,” or “characteristic x-rays.” The emitted photon is lower in energy than similar transition that occur in hotter plasmas, as the higher electron density can shield the nucleus, which lowers the energy difference between states. As these transitions are more often observed and more easily studied in colder plasmas (often colloquially referred to as “cold plasmas”), these transitions can be difficult to study in HED pulsed power plasmas. There is an effort being made to produce cold plasmas, which was a driving motivation behind the development of the Sparky-HXRS machine (see Section 5). The other important models for this work were L-shell models of Cu and Zn, to describe line radiation from brass loads. L-shell radiation refers to radiation produced from transitions that end in the L-shell, or the n=2 level.

#### *3.3.5.3 MAIZE Inductance Model*

As the MAIZE LTD driver is a low-impedance (0.1 Ω) machine, the current trace throughout the implosion is strongly dependent upon the load inductance, which changes throughout the implosion. Combined with a proper understanding of the driver and transmission line circuit parameters, this dependence allows us to extract information about the time evolution of the inductance of a load from a measurement of current. Understanding the behavior of the inductance will help us to better optimize future loads as well as measure the strength of the pinch. To calculate time-dependent inductance, we first find the initial inductance of the load. The initial inductance of each load is determined from calculations of the partial self-inductance of each wire/foil, the partial mutual inductance between each wire/foil, and the partial mutual inductance between each wire/foil and the six axial return posts of the load hardware. Other partial mutual inductances vary negligibly between shots and are accounted for in the series inductance of the load adapter hardware in the MAIZE circuit model. Changing the wire radii or foil thicknesses (as opposed to positions) in these calculations produced minimal changes in the load inductance (<0.3% for factor of two expansion). Therefore, the wire/foil explosion prior to the pinch is assumed to have a negligible effect on the inductance, so the load inductance prior to bulk motion of load material is taken to be constant [27], [42]. Under these simplifying assumptions, we match the portion of the measured current in which the current is rising and when the load is in the plasma phase, but has not yet begun pinching, to a simulated current pulse using the initial load inductance to find a suitable time-averaged resistance of the load at the onset of radiation emission. The time at which the load enters the plasma phase can be seen on the measured current trace as a “notch” in

which the slope of the measured current trace decreases, around 30-50 ns after the start of current; this timing is also typical of calculated ablation times using temperature-dependent resistivity and integrated electrical power [43].

Using the calculated initial load inductance and characteristic resistance, a simulated current is calculated in which the pinch does not occur and the load is static. In previous calculations (refs. [27], [42]), the time-dependent inductance was calculated by finding the difference in the simulated and measured traces, and computing

$$L(t) = L(0)\frac{I_{sim}^2}{I_{meas}^2},$$

Equation 14

where L(t) is the *effective* time-dependent inductance associated with the total driver-load circuit, L(0) is the initial inductance of the circuit prior to the start of current, $I_{sim}$ is the simulated current pulse, and $I_{meas}$ is the measured current pulse. However, this effective inductance ignores the power associated with the mechanical energy driving the load implosion [77]. Therefore, a modified calculation was implemented to solve for the inductance iteratively which accounts for this energy-transfer mechanism and more closely approximates the true load inductance as a function of time. In this method, the initial guess for L(t) is calculated in the previous manner, but the notation is changed to allow for future iterations,

$$L(t) = L(0)\frac{I_{sim}^2}{I_{meas}^2} \Rightarrow L(t) = \frac{L_0 I_{sim\_0}^2}{I_{meas}^2} = \frac{2E_0}{I_{meas}^2},$$

Equation 15

where $E_0$ is the energy stored in the magnetic field. Then, we calculate the implied change in the electromagnetic energy stored in the cavity as a function of time,

$$\Delta E(t) = -\frac{1}{2}\int \frac{dL_i}{dt} I_{meas}^2 \, dt \,,$$

Equation 16

and L is then recalculated by,

$$L_{i+1}(t) = \frac{2(E_0 + \Delta E(t))}{I_{meas}^2},$$

Equation 17

to get the next iteration. The inductance is then calculated by comparing $L_{i+1}(t)$ and $L_i(t)$, finding the maximum error over the interval of interest, and continuing to iterate with Equation 16 and Equation 17 until the error falls below a specified convergence criterion. In these calculations, the convergence criterion used was 0.1 nH. Note that we choose this iterative calculation method rather than numerically solving a nonlinear system of circuit equations for the inductance L(t) because it is less sensitive to calibration errors in the measured current. This time-dependent inductance calculation of the plasma load throughout the pinching process can be considered a measurement of pinch strength. The experimentally determined changes of load inductance on Al, brass, and W DPWAs and Al DPFLs exhibited correlations in both magnitude and time with measurements of x-ray bursts on shots that demonstrated strong Al and W plasma pinching processes.

Due to the sensitivity of the MAIZE LTD current pulse to switch jitter and dynamic load inductance, there can be a small, but relatively significant, variance between current risetime and load implosion times of even identical load geometries. This is unlike what is seen on "stiffer," high-impedance machines, where identical load types have highly repeatable implosions, such as data seen on the high-impedance UNR Zebra driver (1.9 Ω). For this reason, we have selected data that demonstrate a strong difference in simulated vs. measured current (i.e. data that demonstrate a large inductance change due to an implosion that is cleanly detected), where these data were also selected from shots with low switch jitter, as determined by risetimes that are within the expected range for the total inductance of the loads and load adapter hardware.

# 4 MAIZE Load Implosion Dynamics and Characteristics with Comparisons to Zebra

The plasma dynamics of implosions on pulsed power machines is heavily dependent upon the current carrying load type and configuration used. Planar Wire Arrays (PWAs) [Single Planar Wire Arrays (SPWAs) and Double Planar Wire Arrays (DPWAs)] have proven to be excellent x-ray radiators on both university-scale pulsed power generators [24] and at Sandia National Laboratories (SNL) on the multi-MA Saturn machine [16]. Among the loads tested on the UNR Zebra generator, planar wire arrays (PWA) were found to be the most efficient compact x-ray radiators at the 1–2 MA scale [24], [34], [78]. In comparison with cylindrical wire arrays (CWA), the PWA is characterized by a unique combination of: (1) larger resistive energy deposition [24]; (2) higher radiated output powers [24], [34], [78]; (3) small (mm) scale size [24], [35]; (4) the possibility of radiation pulse shaping [25]; (5) the ability to study plasma flows and spectroscopy from two and even three planes of different wire materials in one shot [79], [80]; and (6) overall good diagnostics access to inner plasmas [24]. As an example of the efficient radiation output, DPWAs (particularly those made from tungsten or other mid-atomic-number elements) have demonstrated radiation pulses of up to 30 kJ and >1 TW on the UNR Zebra generator, which stores 150 kJ in its capacitor banks [81]. In addition to being excellent radiators of x-rays, PWA sources have applications in inertial confinement fusion (including the new compact multisource hohlraum design [16], [78]), astrophysical studies [82], and lasing research [83].

As a possible alternative to PWAs and CWAs on future >30-MA generators, Planar Foil Liners have been proposed. The continuous foil load is thought to be a useful replacement for discrete wires at >30-MA current levels because when the CWAs and/or PWAs are scaled to such currents, the interwire gap spacing decreases, and the coronal plasma surrounding each individual wire expands and significantly overlaps with the coronal plasmas from neighboring wires [35]. Previously, encouraging results with Double Planar Foil Liners (DPFLs) have been obtained in experiments using the high-impedance UNR Marx bank Zebra generator [35], [36], where it was found that the Al DPFL electron temperature ($T_e$), electron density ($n_e$), and x-ray yield were comparable to Al DPWAs with similar mass. However, almost no data on DPFL x-ray sources has been collected on low-impedance drivers, such as a single-cavity Linear Transformer Driver (LTD). As a result, very little is known about the implosion and radiative performance of these load types on low-impedance drivers.

Low-impedance LTD accelerators are a relatively new technology, and they have been theorized to be capable of reaching higher currents and powers more efficiently than the widely-used Marx-driven generators. Because of this, LTDs have been proposed for future petawatt-class Z-pinch generator designs [84], [85]. Recently, Al DPWAs were successfully imploded on the low-impedance (0.1 Ω), low-stored-energy (7.9 kJ at ~70-kV charge voltage) MAIZE LTD at the University of Michigan [26]. By contrast, this dissertation presents the first experimental results of Al DPFL implosions on the low-impedance MAIZE facility. The DPFL results obtained on MAIZE are compared to the more well understood Al DPWAs and W DPWAs configurations on MAIZE [26], [27] and to Al DPFLs on the Zebra generator [35], [79].

## 4.1 Experimental Details

Experiments were performed using the Michigan Accelerator for Inductive Z-Pinch Experiments (MAIZE) at UM, which is a single-cavity Linear Transformer Driver (LTD) [7]. MAIZE is a single-stage, low impedance (0.1 Ω), 1 MA class LTD with 100 ns risetime into an impedance-matched load. The load is housed in the center of a circular, 1-m-diameter vacuum chamber located in the center of the 3-m-diameter cavity. Experimental diagnostics were located inside and outside the vacuum chamber. The setup inside the chamber is shown in Fig. 2. Diagnostics included various filtered x-ray diodes; x-ray spectrometers and x-ray pinhole cameras; a filtered Faraday cup placed above the load for measurement of the electron beam [26]; an ultra-fast, intensified, 12-frame camera for use in shadowgraphy/self-emission imaging; and B-dot loops at four azimuthal locations on the radial transmission line for measurement of the time-resolved current pulse. Results of electron beam measurements made with the Faraday cup above the anode will be the subject of a future publication.

The time-resolved x-ray output throughout each shot was measured using a side-on absolutely calibrated photoconducting diamond detector (PCD) with a time resolution of 0.5 ns. The PCD was filtered to detect photons with energies above a cutoff energy of 2.4 keV. The cutoff energy E is defined as the energy where the transmission through the filter drops to a value of 1/e, where e is the base of the natural logarithm. Three side-on, cross-calibrated AXUV-HS5 Si-diodes with a time resolution of 1 ns and filtered to detect >1.4, >3.5, and >9 keV x-rays were also used to measure the time-evolution of the x-ray output in different energy bands. All of these diode detectors were placed such that the line of

sight would be within 15° or less with respect to the planes of the arrays for DPWAs and DPFLs (i.e. the line of sight that looks into the gap between the planes). The oscilloscopes used featured a sample rate of 5 GS/s, capable of resolving the PCD time resolution.

The two side-on x-ray pinhole cameras (spatial resolution of 90 μm) were placed approximately 90° apart from each other to view the load from both the "front" and "side" view; the first was placed within 15° or less with respect to the planes of the arrays, while the second was placed at approximately 95°-105°. Each pinhole was capable of taking three independent, time-integrated x-ray images (filtered to detect >1.4, >1.6, and >3.5 keV x-rays) onto Kodak Biomax MS X-ray film, with grain size 0.12±0.03 μm [86]; the use of this film for x-ray imaging and spectroscopic measurements is discussed in detail in ref. [87]. Two side-on time-integrated x-ray spectrometers were applied to estimate electron temperature ($T_e$), electron density ($n_e$), and opacity effects of the Al Z-pinch plasmas, using non-local thermal equilibrium (non-LTE) kinetic models [26], [88]. The two spectrometers were employed to measure x-rays in two different x-ray bands: a softer x-ray spectral region between 4 and 13 Å and a harder region between 1 and 2.4 Å. The softer x-ray spectrometer had a convex potassium acid phthalate (KAP) crystal with a double lattice spacing 2d = 26.63 Å, a radius of curvature of 51 mm, a 1-D axial spatial resolution of 4 mm, and a spectral resolution $R=\lambda/\Delta\lambda=500$. The harder x-ray spectrometer had a convex lithium fluoride (LiF) crystal with a double lattice spacing 2d = 4.027 Å, a radius of curvature of 25.4 mm, and a 1-D axial spatial resolution of 4 mm. The spectrometers were equipped with 7.5-μm-thick Kapton film together with 3-μm-thick Mylar (aluminized on both sides with 0.15-μm-thick Al layers) to protect the inside film from unwanted outside light. Previous results of these diagnostics are discussed in detail in refs. [26], [27].

An intensified, ultra-fast 12-frame camera was employed to collect self-emission images prior to and throughout the Z-pinching process to study the plasma evolution. In previous experiments, this ultra-fast camera was paired with a 532-nm, 2-ns, frequency doubled Nd:YAG pulse, split into optical beams with a 10 ns delay between each beam for use as a backlighting source for shadowgraphy images [41]. Shadowgraphy images of DPWA implosions on MAIZE are presented in refs. [26], [27]. For self-emission imaging, shots were performed without the laser backlighting, and the images taken were only of the light emitted by the Z-pinching load. Previous experiments using cylindrical foil liners on MAIZE showed only small variations in the observation of the plasma-vacuum boundary between self-emission and laser-backlit shots [47], [48].

Four B-dot probes, radially located approximately 0.4 m from the load at the center of the chamber and equally spaced azimuthally (90° between adjacent probes) were used to measure the time-resolved current trace throughout the Z-pinch. As the MAIZE LTD is a low-impedance machine, the change in inductance of the plasma load throughout the Z-pinching process has a larger effect on the current trace compared to stiff (high impedance) drivers like the Zebra Marx generator at UNR. The effect that the load inductance has on the current trace can be explored by comparing the measured current trace to a simulated, static inductance (non-imploding) load to calculate an effective inductance of the load throughout the Z-pinch as a function of time. This method is explained in detail in ref. [42] and is expanded in Section 3.3.5.3 to more closely approximate the time-dependent load inductance.

In these experiments, the DPWAs consisted of two parallel wire planes, while the DPFLs consisted of two parallel foil planes. The DPWA masses were calculated from the number of wires, the diameter of the wires, and the wire material, while the DPFL masses were calculated from the width of the foil, the thickness of the foil, and the foil material. In ref. [25], it was observed that DPWA implosion dynamics depend strongly upon the aspect ratio φ, defined as the ratio of the array width to the interplanar gap. In the following sections, we present results from two DPWAs (one made of 5-μm-diameter W wires, and another made of 12.7-μm-diameter Al wires) and one DPFL (made of 1.8-μm-thick Al foil) imploded using the MAIZE LTD generator. The anode-cathode gap was 1 cm for both the DPWAs and the DPFLs, while the interwire spacing was 0.7 mm for the DPWAs.

Due to the relatively large inductance of the DPWA/DPFL load hardware, the MAIZE LTD was limited to 70% of the maximum charge voltage in an effort to prevent damage to the main (central) insulator and to minimize voltage reversal on the capacitors. Under such operating conditions, the peak current was typically between 450 kA - 600 kA and the risetime ranged from 200 - 300 ns.

## 4.2 Total Radiated Energy Output Analysis

The x-ray yields of the imploded DPWAs were approximated by integrating the signals from the absolutely calibrated PCD over the entire duration of emission and assuming isotropic radiation into 4π steradians. The anisotropy of total x-rays for DPWAs was previously found to be small (~10-20%) for similar DPWA configurations [89]. Table 2 combines recent data from ref. [64] on high-atomic-number tungsten (W) and low-atomic-number aluminum DPWAs on the MAIZE LTD with the new data presented from

brass DPWAs. The previous data on Al and W DPWAs were chosen to represent similarly low- to mid-ranging aspect ratio DPWAs ($\phi = 0.58$ for Al and $\phi = 1.05$ for W) to MAIZE Shot 1249. By comparing the x-ray outputs, it was found that the total radiated energy in the >2.4 keV band increases with atomic-number. Low-atomic-number Al produced the lowest yield, mid-atomic-number brass produced the next highest, and high-atomic-number W produced the highest yield.

| MAIZE Shot | Material | Load | Aspect Ratio | Mass (μg/cm) | Current Max (kA) | Current Risetime (ns) | Implosion Time (ns) | Energy over 4π (J) |
|---|---|---|---|---|---|---|---|---|
| 1315 | Al | DPWA | 0.58 | 41 | 585 | 260 | 220 | 0.067 |
| 1320 | Al | DPFL | 1.17 | 340 | 565 | 215 | 140 | 0.033 |
| 1334 | W | DPWA | 1.05 | 76 | 475 | 200 | 245 | 1.6 |
| **MAIZE Shot** | **Material** | **Load** | **Aspect Ratio** | **Mass (μg/cm)** | **Current Max (kA)** | **Current Risetime (ns)** | **Implosion Time (ns)** | **Energy over 4π (J)** |
| **1249** | Brass | DPWA | 1.67 | 57 | 462 | 180 | 224 | 0.53 |
| **1250** | Brass | DPWA | 2.33 | 76 | 475 | 210 | 230 | 0.77 |

Table 2: Experimental parameters tested on MAIZE. The implosion times are measured relative to the start of the current pulse. The radiated energies are for the >2.4 keV band, integrated over the duration of the experiment. The error in energy calculations was 35% [27]. Asynchronous LTD switch firing times and current loss in the MITL region are factored into an estimated error of approximately 50 kA in the maximum currents listed. Al and W data was previously published in ref. [64].

## 4.3 Radiative Properties of Low-Atomic-Number DPFLs and DPWAs on MAIZE

During these experiments, a relatively massive Al DPFL was imploded (340 μg/cm). Multiple shots with this load were conducted to understand the reproducibility of the implosion. The DPFL data presented have been selected from these shots to best represent the DPFL implosion. As can be seen in Figure 14, the Al DPFLs generated radiation bursts throughout the implosion. The radiation output from the Al DPFLs is characterized by

longer lasting bursts compared to the mass-optimized Al DPWA and the W DPWA on MAIZE, which will be discussed later. The most intense radiation bursts from the Al DPFL were measured to last approximately 70 ns for the >3.5 keV band and much longer (about 160 ns) for the >1.4 keV band. Three distinct peaks can be seen in the PCD signal, occurring between 100 and 150 ns, as well as two smaller peaks from 150-180 ns that concur with noticeable peaks in the >3.5 keV signal. Another interesting observation to note is that the load began radiating shortly after the start of the current pulse (approximately 80 ns) and long before peak current occurred at approximately 250 ns.

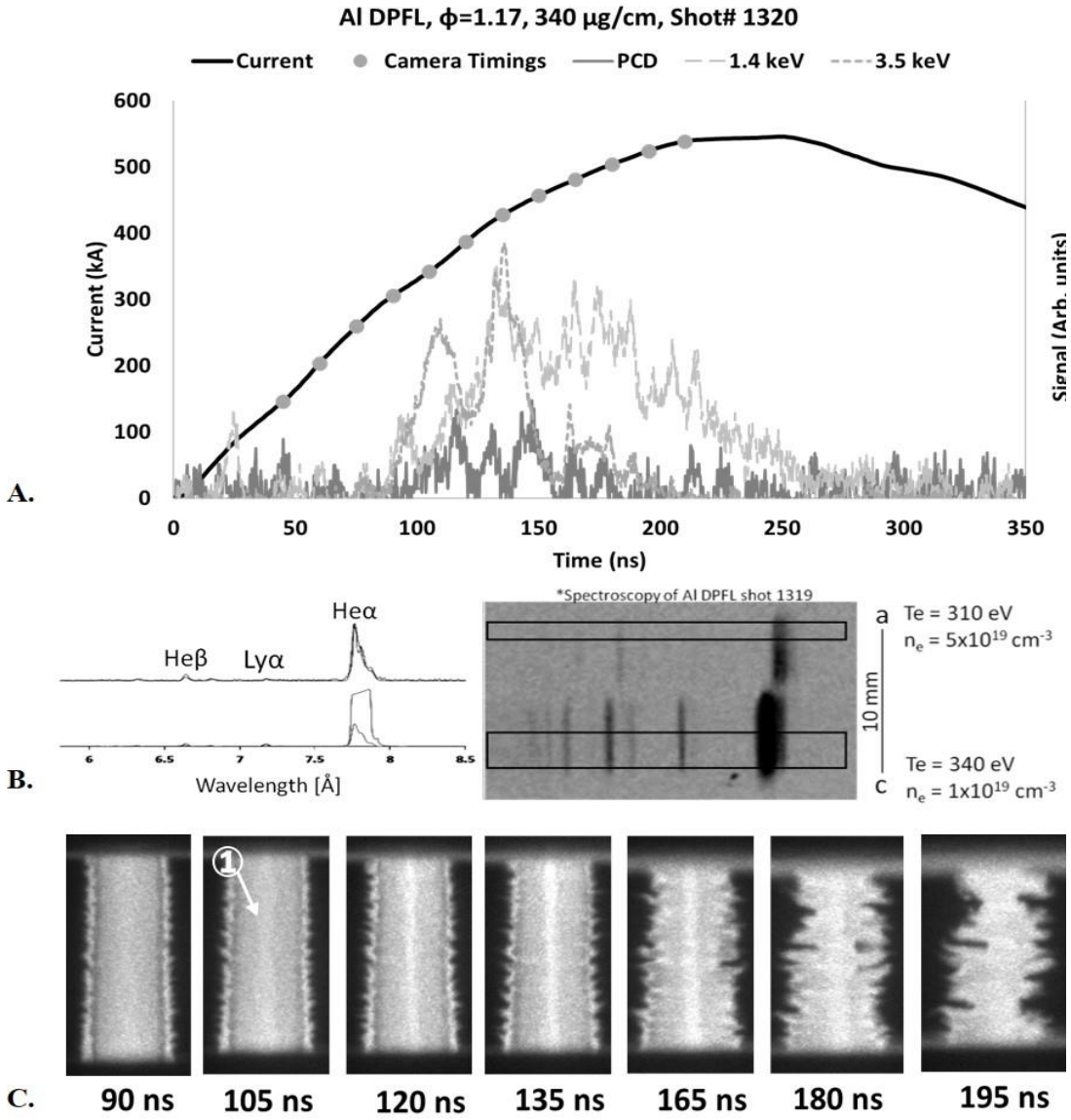


Figure 14: Al DPFLs on MAIZE. A. Radiation output from MAIZE Shot 1320 (interplanar gap = 3 mm, planar width = 3.5 mm, aspect ratio $\phi$=1.17, mass = 340 µg/cm). The PCD signal (dark grey) shows radiation in the >2.4 keV region, while the Si-diode signals (light grey long dashes and grey dashes) shows radiation signals in >1.4 and >3.5 keV spectral bands, respectively. Current (black) risetime was 250 ns with the major implosion occurring at 135-145 ns from the start of current. Grey dots correspond to moments when a self-emission image was taken. B. MAIZE Shot 1319 (an identical load configuration to Shot 1320). The 1D spatially resolved, time integrated X-ray spectra are compared to theoretical modelling to find plasma conditions. C. Self-emission images from MAIZE Shot 1320 shows the implosion evolution in time from the start of current. Formation and position of the primary precursor column is marked by "1."

The initial x-ray burst measured from the radiation signals (Figure 14A) occurs simultaneously with a significant increase in the brightness of the central column seen in the self-emission images (Figure 14C) at 105-120 ns. Likewise, the second and most powerful burst occurs shortly after at 130-140 ns, followed by two smaller bursts at 155-165 and 175-185 ns. The load continues to produce measurable x-ray signals up to 250 ns after the start of current. Altogether, the Al DPFL demonstrates a longer, more drawn-out pinch process, with multiple radiation peaks, than is typically observed in DPWA configurations tested on MAIZE, which usually demonstrate a more definable peak of x-ray emission. This may be due to the additional mass of the DPFL (relative to the less massive DPWAs tested on MAIZE). As can be observed in the self-emission images, mass accumulation along the central axis formed a central "precursor" column at 90-105 ns. However, no standing shocks appear to have formed by this time (see Figure 15C and Figure 16C in this paper, and Fig. 5 in ref. [27] for images of standing shocks, as well as ref. [25] for a detailed explanation of how they form); instead, a steady stream of mass continuously contributed to the central plasma column. This drawn-out z-pinching process is also likely enhanced by MAIZE's relatively high sensitivity to changes in load inductance throughout the process. That is, as the precursor plasma is advected to the central column, some of the drive current is likely transported to the column as well. This makes the load more inductive, which reduces the drive on the remaining foil material and thus extends the time required to implode the bulk of the foil material. This phenomenon will be addressed in more detail in Section 4.6 when discussing the inductance modelling.

As is understood for DPWA implosions, due to the initial current distribution through the load, the outer wires ablate first [24]–[26]. Similarly, it is believed that the outer regions

of the foil planes will ablate prior to the inner parts of the foil planes. This was modelled in ref. [24], which showed preliminary calculations for a double planar load with an even mass distribution, analogous to a foil plane. As such, with the heavy mass of the DPFL, the material on the outer parts of the foil planes likely imploded and pinched earlier than the inner parts of the foil planes. With the higher mass of the DPFL, this process is extended in time, leading to the longer radiation period observed (relative to the less massive DPWAs tested on MAIZE). The radiation traces presented in Figure 14 (with multiple bursts spread out in time) are similar to those observed for DPFL shots on Zebra (see ref. [35]), which demonstrated a higher number of radiation bursts spread out over a longer duration in time when compared to DPWA shots on the same generator, albeit with a shorter overall pinching time than on MAIZE (60 ns on Zebra versus 150 ns on MAIZE).

Using spatially resolved spectroscopic analysis, including modelling of K-shell Al transitions from the high Rydberg states for the Al DPFL [26], [88], the electron temperature ($T_e$) and density ($n_e$) were modeled near the anode and cathode (Figure 14B): $T_e$ was 310 eV, $n_e$ was 5 x $10^{19}$ $cm^{-3}$ near the anode, and $T_e$ was 340 eV, $n_e$ was $10^{19}$ $cm^{-3}$ near the cathode. Also, the modeling indicated an optically thin plasma near the anode (Figure 14B), which is very unusual for pulsed power Al plasmas on Zebra.

For comparison, less massive Al DPWAs (41-76 μg/cm) were also imploded on the MAIZE LTD generator. MAIZE Shot 1315 was selected for analysis as it demonstrated the most pronounced and integrable signal on the PCD, such that the overall energy output could be measured (see Table 2). Additionally, a shot featuring an identical load configuration was modeled in ref. [26] using the Wire Ablation Dynamics Model (WADM) [72], [90]. In contrast to the more massive Al DPFL, the less massive Al DPWA showed a

more typical radiation burst behavior (Figure 15A); however, the main burst still occurred prior to peak current (at 205-215 ns). The total x-ray duration (which includes multiple bursts) is 35-45 ns. The main x-ray burst (i.e., the first burst, which is less than 5 ns in duration) was followed by two smaller bursts at 225 ns and 235 ns. These subsequent bursts had peak magnitudes that were ~1/3 of that from the main burst, as measured in both the >2.4 keV band (PCD) and the >3.5 keV band (Si-diode). There is a small amount of radiation in the >3.5 keV region beginning at 80-90 ns, which coincides with the early formation of standing shocks appearing in Figure 15D. These shocks are the bright structures that appear in the 95 and 125-ns frames of Figure 15D. Time-integrated pinhole images show the primary sources of x-ray emission were nearest the electrodes (see Figure 15B).

Further observations of the self-emission images in Figure 15C show that around 155-185 ns, the two independent plasma flows begin to merge along the central axis, forming the precursor plasma column. The formation of a precursor column is rare for DPWA loads with such low aspect ratios ($\varphi<0.7$); this phenomenon was first reported on the MAIZE LTD in Ref. [84]. The main z-pinch begins around 215 ns, after the wire material has fully ablated and is flowing towards the central column, which corresponds well in time with the main radiation burst. Spectroscopic analysis of the Al DPWA shows that near the anode, $T_e$ was 380 eV and $n_e$ was $10^{19}$ $cm^{-3}$, while near the cathode, $T_e$ was 375 eV and $n_e$ was 3 x $10^{19}$ $cm^{-3}$ (see Figure 15C).

The x-ray yields of both the more massive Al DPFL and the less massive Al DPWA were approximated by integrating the signals from the absolutely calibrated PCD over the entire duration of emission and assuming isotropic radiation into $4\pi$ steradians. The

anisotropic distribution of total x-rays for DPWAs was found to be small (~10-20%) for similar DPWA configurations [89]. The Conversion Factor (ε), defined as the ratio of the total x-ray output in a certain energy range (>2.4 keV in this work) to the energy initially stored in the generator capacitors (7.8 kJ, in this work), is a measurement of the efficiency of the machine. As shown in Table 2, the x-ray yield in the >2.4 keV band of the more massive Al DPFL was 3.3 x $10^{-2}$ J, and thus $\varepsilon_{Al\ DPFL}$ = 4.2 x $10^{-6}$, while the optimized, less massive Al DPWA was only twice as large at 6.7 x $10^{-2}$ J, and thus $\varepsilon_{Al\ DPWA}$ = 8.5 x $10^{-6}$. This is an intriguing result, as the mass optimized DPWA only outperformed the much heavier DPFL by a factor of two. This could imply that a mass optimized DPFL could match or possibly outperform a DPWA of similar mass on the MAIZE LTD. The experimental error in the total x-ray output was 35% [27].

Spectroscopic modelling of both the Al DPFLs and DPWAs showed comparable electron temperature ($T_e$) and density ($n_e$): $T_{eDPFL}$ = 310-340 eV, $n_{eDPFL}$ = (1-5) x $10^{19}$ $cm^{-3}$ (I = 0.56 MA), and $T_{eDPWA}$ = 375-380 eV, $n_{eDPWA}$ = (1-3) x $10^{19}$ $cm^{-3}$ (I = 0.59 MA). It was found that the Al DPFL plasma on MAIZE was cooler near the anode and hotter near the cathode. Additionally, the Al DPFL plasma on MAIZE was found to be optically thin near the anode, a rarity amongst Al plasmas on the Zebra generator [80], [88].

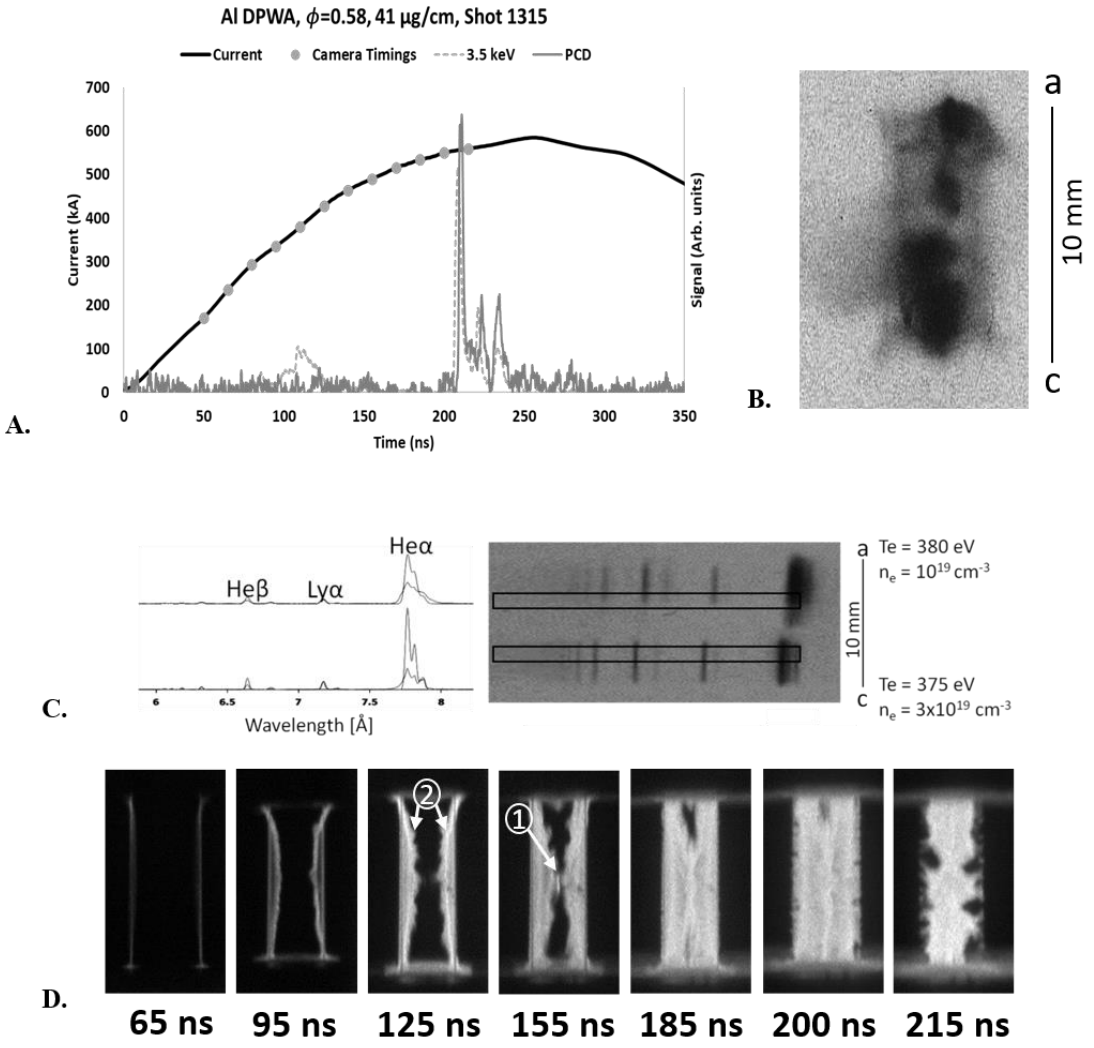


Figure 15: Al DPWA from MAIZE Shot 1315 (N=6/6, interplanar gap = 6 mm, interwire gap = 0.7 mm, aspect ratio $\phi$=0.58, mass = 41 µg/cm). A. The PCD signal (dark grey) shows radiation in the >2.4 keV band, while the Si-diode signal (grey dashes) shows radiation in the >1.4 keV band. The current pulse (black) had a risetime of 260 ns with the implosion occurring at 205-215 ns from the start of current. Grey dots correspond to moments when a self-emission image was taken. B. Time-integrated pinhole image in the >1.4 keV x-ray region from Pinhole camera #2 (looking between the planes). C. The 1D spatially resolved, time integrated X-ray spectra are compared to theoretical modelling to find plasma conditions. D. Self-emission images showing the implosion evolution in time from the start of current. The formation and position of the primary precursor is marked by "1," and the formation of the standing shocks is marked by "2."

## 4.4 Radiative Properties of High-Atomic-Number DPWAs on MAIZE

In addition to Al DPWAs, W DPWAs were imploded to examine how a higher-atomic-number wire load performs on the MAIZE LTD. The W DPWA successfully imploded, which again presented the first results of its kind on a low-impedance LTD generator [27]. The diameter of the W wires was chosen such that the mass of the W DPWAs (61-76 μg/cm) would be comparable to the Al DPWAs. The most massive of such W DPWAs (76 μg/cm, MAIZE Shot 1334) was used here as the closest comparison in mass and aspect ratio to the high mass Al DPFL (although the DPFL was still a factor of ~4x higher in mass). The W DPWA implosion was characterized by a well-defined signal from the x-ray burst, with a sharp main peak on the PCD (>2.4 keV) signal of 25-30 ns duration, followed by a 25-30 ns secondary burst, in which the plasma load was still radiating, but with lower power (Figure 16A). The time-integrated pinhole image in the >1.4 keV band shows a relatively uniform emission throughout the whole of the implosion (see Figure 16B). Radiation in the >1.4 keV region begins emitting earlier than the main radiation burst (approximately 80 ns), which corresponds to the formation of the precursor column and standing shocks, as can be seen in the self-emission images of Figure 16C. A peak in the >1.4 keV region occurred at approximately 140 ns, which directly corresponds to a noticeable increase in self-emission brightness of the precursor column. The PCD signal (>2.4 keV) and the Si-diode signal (>1.4 keV) show two distinct peaks in that same time period (the PCD around 110 ns and the >1.4 keV around 100 ns and 140 ns). The x-

ray yield in the >2.4 keV region of the W DPWA was 1.6 J, and $\varepsilon_{W\ DPWA}$ = 2.1 x $10^{-4}$, far larger than the Al DPFLs and DPWAs tested.

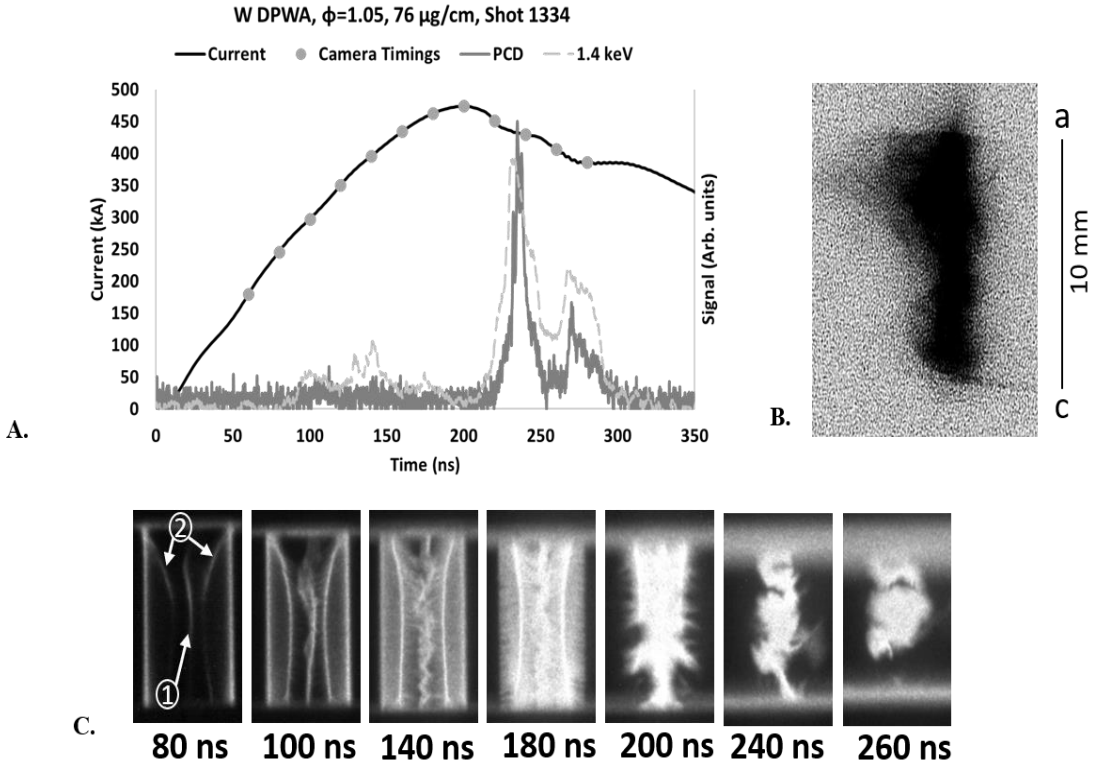


Figure 16: W DPWA from MAIZE Shot 1334 (N=10/10, interplanar gap = 6 mm, interwire gap = 0.7 mm, aspect ratio $\phi$=1.05, mass = 76 μg/cm). A. The PCD signal (dark grey) shows radiation emission in >2.4 keV band, while the Si-diode signal (light grey dashes) shows radiation emission in the >1.4 keV band. The current pulse (black) had a risetime of 200 ns with the implosion occurring at 235-245 ns from the start of current. Grey dots indicate camera timings for self-emission images. B. Time-integrated Pinhole image in the >1.4 keV x-ray region from Pinhole camera #1 (looking from the side, ~90° from the space between the planes). C. Self-emission images from MAIZE Shot 1334 showing the implosion evolution in time from the start of current. The formation and position of the primary precursor is marked by "1," and the formation of the standing shocks is marked by "2."

## 4.5 Discussion of MAIZE LTD Performance

The implosion dynamics of loads on the MAIZE LTD are heavily dependent upon LTD machine performance. Table 4 illustrates this by showing the differences in peak current, current risetime, and implosion time of similar and identical Al DPWA loads imploded on MAIZE in different campaigns. When compared to the measurements taken throughout the 2016 campaign, the shots performed during the 2017 campaign are characterized by a slightly higher average peak current, a longer average current risetime, and a much shorter average load implosion time. On average, the peak of x-ray emission occurred nearly 100 ns earlier in the 2017 campaign than in the 2016 campaign. The variation between the 2016 and 2017 campaigns is not fully understood, but we believe that machine performance likely played a significant role (i.e., some of MAIZE's 40 switches were likely firing late and thus asynchronously). Based on an analysis of the data, these performance inconsistencies were likely present during the 2017 campaign, as the variation in switch firing time likely led to the implosions occurring earlier in time. Nevertheless, we note that the shots performed within a given campaign were reproducible and reliable. Therefore, in an effort to minimize the variance in data due to machine performance, all shot comparisons in this article were performed using shots taken in the 2017 campaign, as DPFL experiments were only performed during this campaign.

| MAIZE Shot | Campaign | Material | Diameter (μm) | Load Type | Number | Interwire gap (mm) | Interplanar gap (mm) | Aspect Ratio | Mass (μg/cm) | Current (kA) | Current Risetime (ns) | Implosi Time (r |
|---|---|---|---|---|---|---|---|---|---|---|---|---|
| 1239 | 2016 | Al | 15 | DPWA | 6/6 | 1 | 3 | 1.67 | 57 | 535 | 275 | 200 |
| 1242 | 2016 | Al | 15 | DPWA | 8/8 | 1 | 3 | 2.33 | 76 | 535 | 275 | 220 |
| 1257 | 2016 | Al | 12.7 | DPWA | 8/8 | 0.7 | 6 | 0.82 | 55 | 510 | 215 | 260 |
| 1258 | 2016 | Al | 12.7 | DPWA | 8/8 | 1 | 6 | 1.17 | 55 | 555 | 215 | 250 |

| MAIZE Shot | Campaign | Material | Diameter (μm) | Load Type | Number | Interwire gap (mm) | Interplanar gap (mm) | Aspect Ratio | Mass (μg/cm) | Current (kA) | Current Risetime (ns) | Implosi Time (r |
|---|---|---|---|---|---|---|---|---|---|---|---|---|
| 1311 | 2017 | Al | 15 | DPWA | 8/8 | 1 | 3 | 2.33 | 76 | 490 | 195 | 80 |
| 1313 | 2017 | Al | 12.7 | DPWA | 8/8 | 1 | 6 | 1.17 | 55 | 545 | 325 | 140 |
| 1314 | 2017 | Al | 12.7 | DPWA | 6/6 | 1 | 3 | 1.67 | 41 | 590 | 260 | 120 |
| 1315 | 2017 | Al | 12.7 | DPWA | 6/6 | 0.7 | 6 | 0.58 | 41 | 585 | 260 | 220 |

Table 3: Selected Al DPWAs from experimental campaigns on MAIZE in 2016 and 2017. Issues with LTD switch firing times and inconsistent B-dot probe readings result in an estimated error of order 50 kA to the peak current values listed.

## 4.6 Dynamic Load Inductance of Low-Atomic-Number DPFLs on MAIZE

As shown in Figure 17 for the Al DPFL, L(t) is strongly correlated with the timing and relative intensity of x-ray emission, confirming that some pinching took place in the precursor column as early as 90-100 ns after the current began. For the Al DPFL, an initial plasma phase inductance was 1.6 nH at 50 ns. As the load begins to implode and material flows towards the center of the load, the difference between the simulated and measured current becomes greater, with the measured current becoming less than the simulated, which corresponds to a rise in inductance. As material begins to form a central precursor column and pinching processes start to occur (Figure 14C), the inductance reaches a local peak (Figure 17B). The start of radiation emission can be seen to correlate in time with the beginning of the rise in inductance, beginning around 80-90 ns, just around the time when the simulated and measured current traces begin to diverge. The first and greatest maximum in load inductance occurs at 115-125 ns, reaching a maximum inductance of 3.5 nH; this first peak corresponds to the first radiation burst in the >3.5 keV band; the

following x-ray burst is likely due to the increase in radiation of the central precursor column, which occurs before the bulk foil material has imploded (as can be seen in the self-emission images in Figure 14C). The inductance peaks at 160-170 ns and at 180-190 ns correlate to bulk foil implosion and weaker x-ray bursts, which are more pronounced in the >3.5 keV signal. The inductance then proceeds to decrease as the pinching process comes to an end, at 245-255 ns, making for a total implosion and x-ray emission duration of >150 ns.

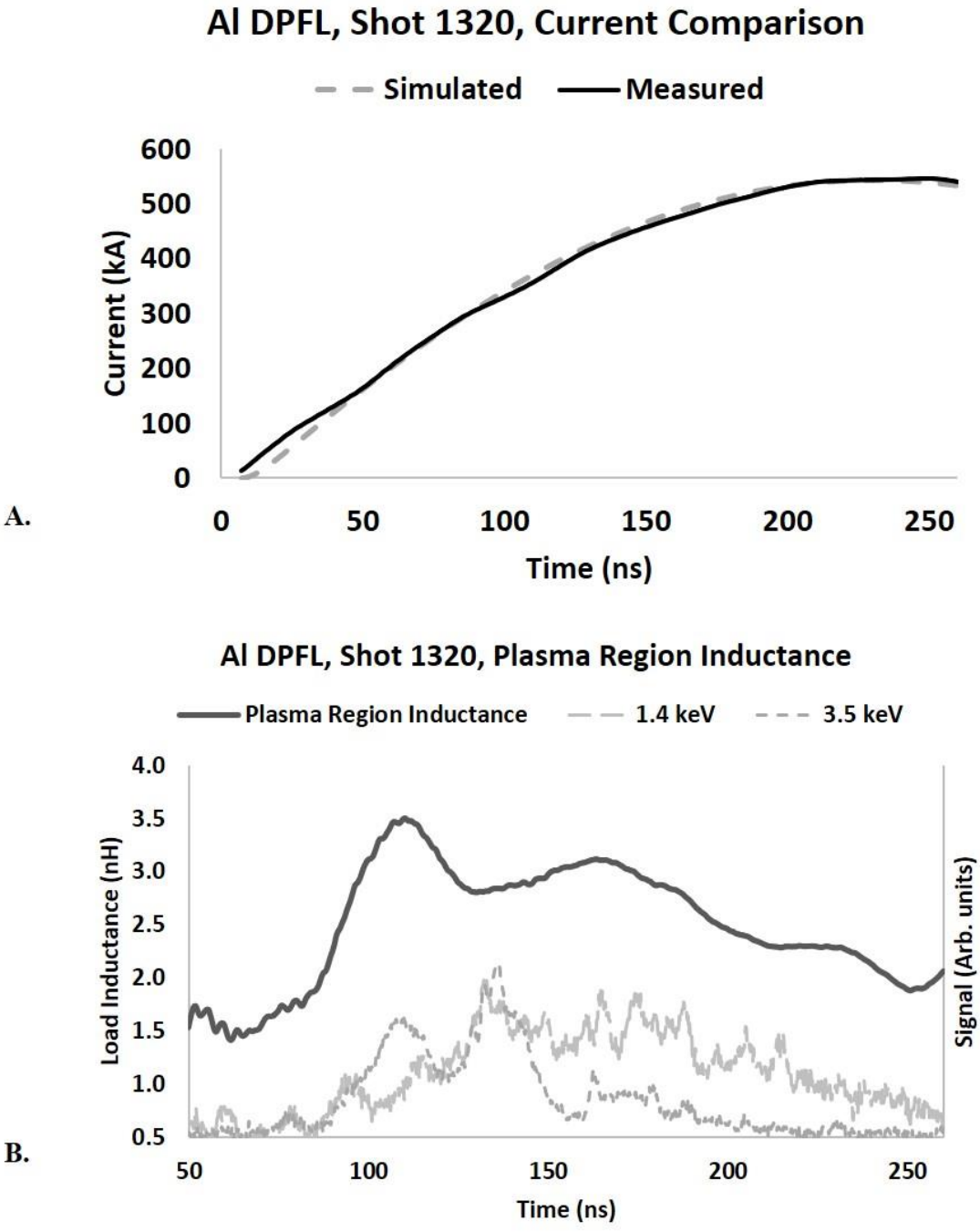


Figure 17: Al DPFL from MAIZE Shot 1320 (interplanar gap = 3 mm, planar width = 3.5 mm, aspect ratio $\phi$=1.17, mass = 55 µg/cm). A. Comparison of simulated current (grey dashes) to the experimentally measured current (black). B. Time-dependent load plasma region inductance throughout the implosion (thick dark grey), plotted with >1.4 keV (light grey longer dashes) and >3.5 keV (grey shorter dashes) x-ray signals.

## 4.7 Dynamic Load Inductance of Low-Atomic-Number DPWAs on MAIZE

Figure 18 shows the inductance modeling for MAIZE Shot 1315. For the AL DPWA (MAIZE Shot 1315), an initial plasma phase inductance was 1.8 nH at 50 ns. As can be seen from both the current trace and inductance calculations in Figure 18, the Al DPWA had different implosion characteristics from those of the Al DPFL presented in Figure 17. By examining the simulated vs. measured current in Figure 18, we see that the measured current begins to deviate at 80-90 ns, which corresponds with the formation of the standing shocks (Figure 15C) and the slight production of radiation in the >3.5 keV band (Figure 18B), concurrent with a noticeable increase in the brightness of the self-emission images from 95-125 ns (Figure 15C), and corresponds to the initial peak in inductance at 105-115 ns (Figure 18B). The maximum peak in the inductance history (corresponding to the main x-ray burst) was 4.5 nH, which is nearly 30% higher than the maximum inductance of the Al DPFL. Although the duration of the increasing plasma load inductance (~80 ns) appears more drawn out than the duration of the radiation burst (~40 ns), the maximum inductance still corresponded well in time with the main x-ray burst (at 205-215 ns). In contrast to the Al DPFL, which had an initial rise to its peak of inductance and then a steady decline, the Al DPWA demonstrated an initial rise in inductance correlating to the formation of the standing shocks, before a momentary decline, and then another rise to the peak inductance, correlating to the main pinch and maximum x-ray burst. Also, a higher peak inductance generally correlates to a higher x-ray yield (see Table 2).

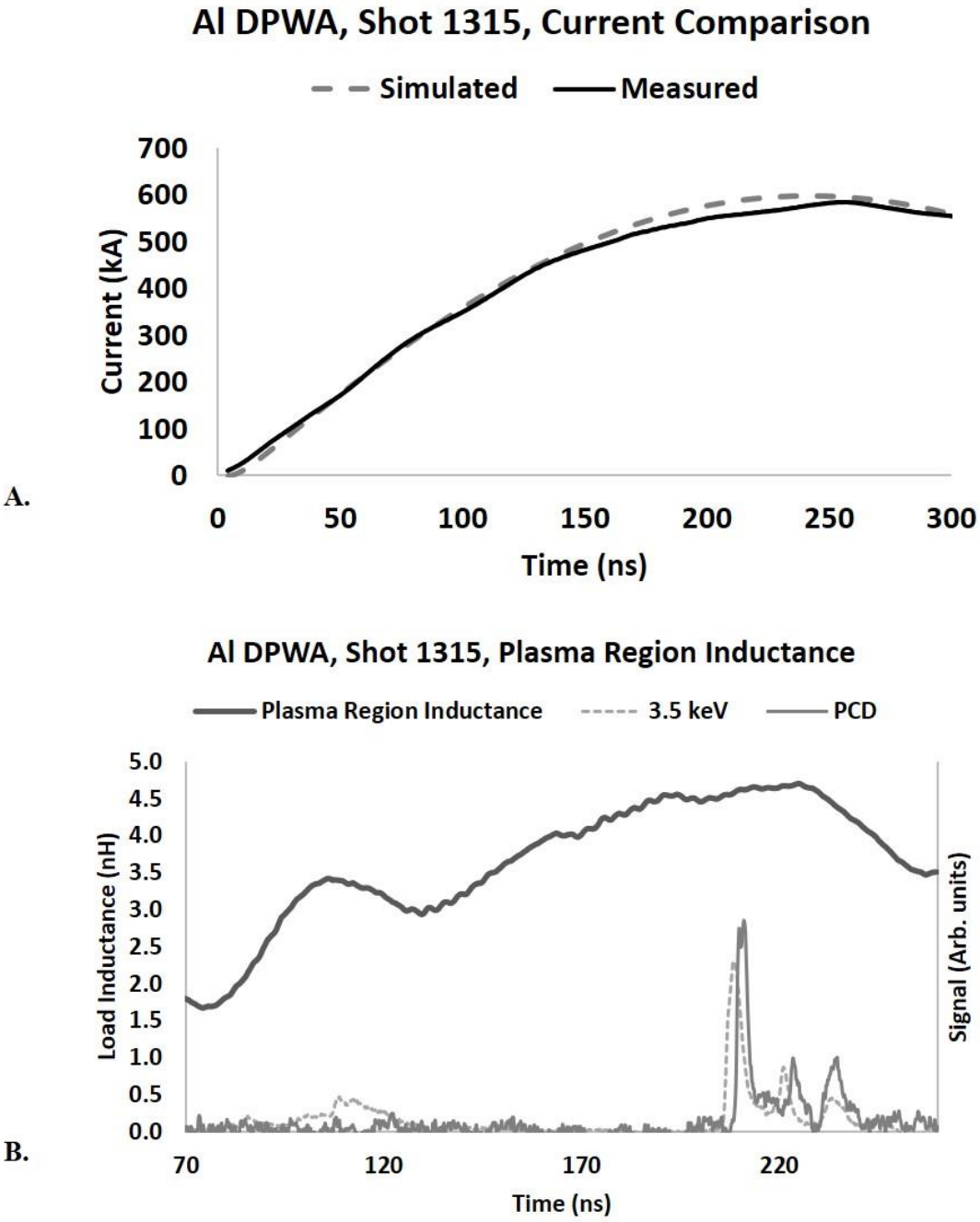


Figure 18: Al DPWA from MAIZE Shot 1315 (N=6/6, interplanar gap-6 mm, interwire gap-0.7 mm, aspect ratio $\phi$=0.58, mass-41 μg/cm). A. Comparison of simulated current (grey dashes) to the experimentally measured current (black). B. Time-dependent load plasma region inductance throughout the implosion (thick dark grey), graphed with PCD (dark grey) and >3.5 keV (grey dashes) x-ray signals.

## 4.8 Dynamic Load Inductance of High-Atomic-Number DPWAs on MAIZE

The W DPWA (Figure 19) imploded after peak current. As expected, the maximum inductance peak is strongly correlated with the main x-ray radiation burst. For the W DPWA (MAIZE Shot 1334), an initial plasma phase inductance was 3.8 nH at 50 ns. At 220-230 ns, the inductance history reaches a local plateau of 7 nH, which correlates with the peak in x-ray emission. At 265-275 ns, the inductance history reaches its peak value of 9 nH, which correlates with the smaller, secondary peak of the main x-ray burst.

Of all the load configurations tested, the W DPWA had the largest inductance at the time of the pinch. This implies more current transfer to the central pinch column and thus a stronger pinch. This is further supported by the x-ray emission measurements in which the W DPWA radiated 25x more energy than the Al DPWA and DPFL. The total duration of primary radiation emission was approximately 60 ns, which corresponds well with the duration of the peak inductance, seen in Figure 19B. The time-dependent inductance of the W DPWA performed similarly to the Al DPWA, in that we see an initial rise in inductance corresponding to an early x-ray burst in the >3.5 keV band, proceeded by a momentary lowering before the inductance rises again to its peak value corresponding to the main pinch and x-ray burst. The W DPWA loads also proved to be very reproducible (for a more detailed description of the implosion dynamics of W DPWAs on the MAIZE LTD, see ref. [16]).

Both the Al DPFL and the Al DPWA reached peak inductance prior to maximum current. Also, the maximum inductance of the Al DPFL was lower than both the Al DPWA and the W DPWA, implying less current transfer to the central column and thus weaker pinching. However, the duration of occurrences of local maxima throughout the primary x-ray emission period for the Al DPFL (135-145 ns) was longer than in the Al DPWA and the W DPWA experiments. This is reflected in the longer emission duration seen in Figure 14A and Figure 17B. The Al DPWA demonstrated a stronger pinch than the Al DPFL, while the W DPWA demonstrated the strongest pinch overall, reaching a maximum inductance of 9 nH. For all of the loads tested, the time-dependent plasma inductance was strongly correlated (in both timing and magnitude) with the measured x-ray signals.

These inductance calculations, coupled with the x-ray emissions presented in Section 4.3-4.4, showcase the differences in the implosion dynamics of the tested Al DPFLs, Al DPWAs, and W DPWAs. The Al and W DPWAs demonstrated multiple quick X-ray bursts with one main pinch, whereas the Al DPFL exhibited slower material movement producing long-duration emission at low intensity. It should be noted that the peak of the plasma region inductance came at the start of x-ray emission for the Al DPFL (around 100 ns), whereas the peak plasma region inductance for the Al and W DPWAs occurred with the primary pinch and nearer to the peak of the current (around 200 ns for the Al DPWA and around 250 ns for W DPWA).

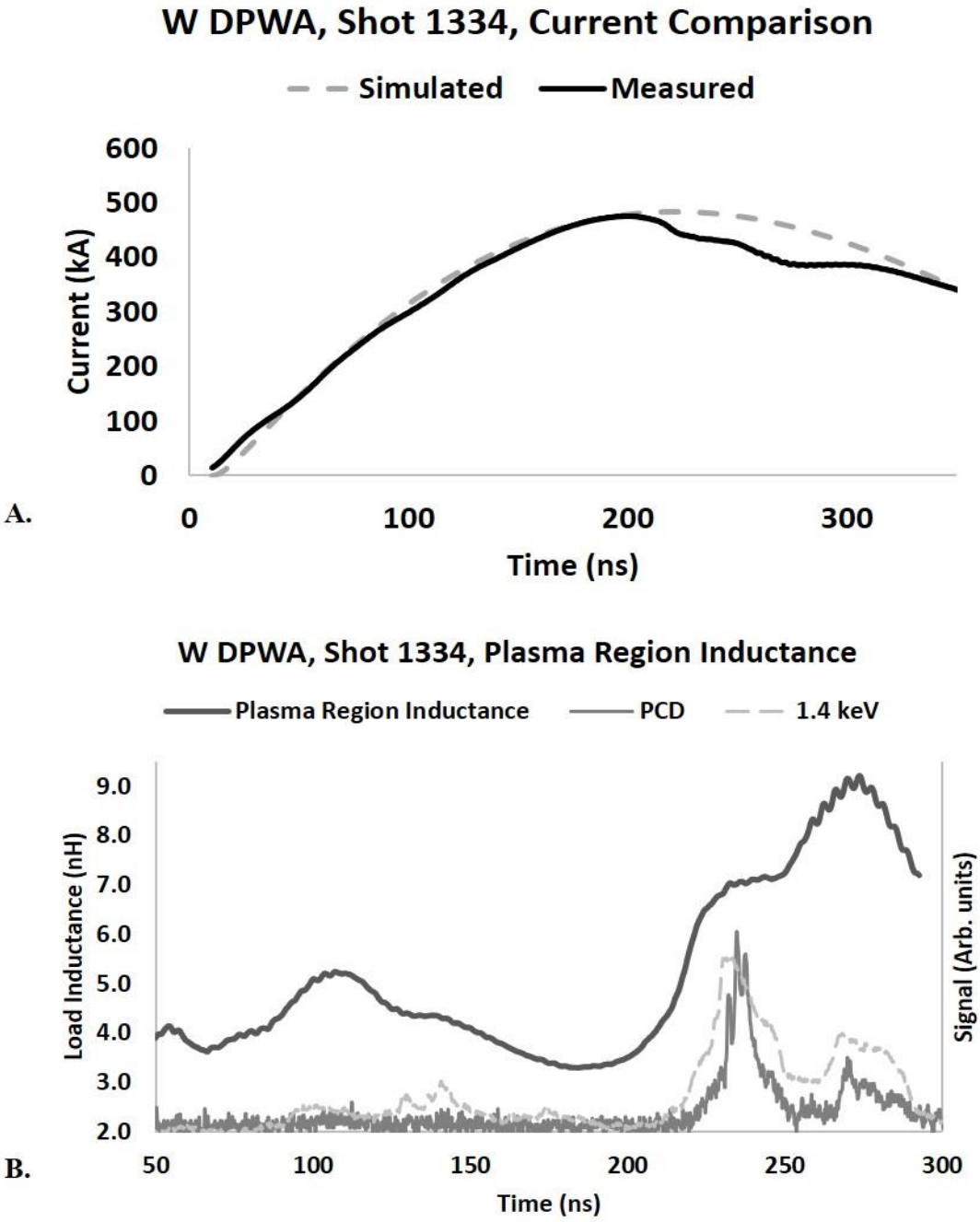


Figure 19: W DPWA from MAIZE Shot 1334 (N=10/10, interplanar gap = 6 mm, interwire gap = 0.7 mm, aspect ratio $\phi$=1.05, mass = 76 μg/cm). A. Comparison of simulated current (grey dashes) to the experimentally measured current (black). B. Time-dependent load plasma region inductance throughout the implosion (thick dark grey), plotted with the PCD x-ray signal (dark grey) and the >1.4 keV Si-diode x-ray signal (light grey long dashes).

## 4.9 Implosion and Radiative Properties of Mid-Atomic-Number DPWAs on Zebra

In ref. [63], the radiative characteristics and implosion dynamics of two brass DPWAs (Zebra Shot 1036 and Zebra Shot 1257) were presented. Both brass DPWAs had identical array configurations (8/8 wire arrays, aspect ratio $\phi = 1.63$, and 124 μg). The brass DPWA Zebra Shot 1036 (see Figure 5 in ref. [63]) was successfully imploded on the Zebra Marx bank, though it had an uncharacteristically long current risetime for Zebra, of approximately 170 ns. The radiation burst began around 170 ns, approximately the same as the risetime, and lasted until 220 ns, making for a total emission time of roughly 50 ns, as measured by the PCD, which, in that work, was filtered at >0.75 keV [63]. The time-gated spectroscopic analysis showed good correlation with the x-ray burst, with the plasma reaching a maximum electron temperature $T_e$ of 450 eV in time with the peak of x-ray radiation burst, and an electron density $N_e$ on the order of $10^{19}$ $cm^{-3}$. Zebra Shot 1257 also imploded successfully, and featured a similar current risetime and radiation burst timing to Zebra Shot 1036 (see Figure 8 in ref. [63]), as measured by the PCD. The spatially resolved, time-integrated spectra from Zebra Shot 1257 showed an electron temperature of 450 eV near the anode and 400 eV near the cathode. In addition to the good correlation with the x-ray signal, analysis of the time-gated spectra showed good correlation with maximum values from the time-integrated spatially resolved spectra, being hottest at the peak of x-ray emission. The non-LTE spectral modelling for brass DPWAs showed evidence of

strong opacity effects in the most intense L-shell Cu and Zn lines, notably the Ne-like lines: Cu 3C, Cu 4C, Cu 4D, and Zn 3C [63].

## 4.10 Radiative Properties of Mid-Atomic-Number DPWAs of Different Aspect Ratios on MAIZE

Multiple brass DPWAs of different configurations were successfully imploded on the MAIZE LTD Generator. The shots presented in this paper represent two different aspect ratios (ϕ=1.67 and 2.33), and featured relatively high x-ray output. MAIZE Shot 1249, shown in Figure 20, was chosen to display the results of the lower aspect ratio, ϕ=1.67, brass DPWAs, and MAIZE Shot 1250 was chosen to display results of the higher aspect ratio, ϕ=2.33, brass DPWAs.

As can be seen in Figure 20A, the lower aspect ratio, $\phi = 1.67$, brass DPWA MAIZE Shot 1249 (6/6, interplanar gap = 3 mm, interwire gap = 1 mm, aspect ratio $\phi$=1.67, array mass = 57 μg/cm), featured a current risetime of 180 ns, with the initial implosion and radiation burst beginning around 200 ns, which corresponds to a dip in the current trace. This dip in current is attributed to a drastic change in load inductance during the pinch, which will be discussed further in Section 4.11. The implosion featured two distinct radiation bursts, which were detected by both the Si-diode (SiD) measuring in the >1.4 keV band, as well as the PCD measuring in the >2.4 keV band. The first burst reached its peak at 225 ns after the start of current with the second burst reaching its peak at 265 ns. The first burst began radiating around 200 ns and finished at 250 ns, while the second began radiating soon after at 255 ns and radiated up to 275 ns, making for a total x-ray

emission time of approximately 75 ns in the >2.4 keV band for the main pinch. It should be noted that both bursts reached relatively the same peak maximum. The >1.4 keV band also featured two distinct peaks, but radiated longer, the second burst radiating until approximately 300 ns, making for a total emission time of approximately 100 ns in the >1.4 keV band. The load also began radiating in the >1.4 keV band earlier than the main pinch, starting at approximately 80 ns and radiating up to 180 ns.

The TIPH (Figure 20B) shows heavy x-ray production nearest the electrodes. The spatially resolved time-integrated x-ray L-shell spectra of Cu and Zn were analyzed using the S-UNR code, a non-Local Thermodynamic Equilibrium (non-LTE) code developed at UNR [63], [74]. The spectral analysis from MAIZE Shot 1249 (Figure 20C), revealed an electron temperature ($T_e$) of 360 eV and density ($N_e$) of $5x10^{19}$ $cm^{-3}$ near the anode, and demonstrates evidence of optically thick Cu 3C and Zn 3C Ne-like lines.

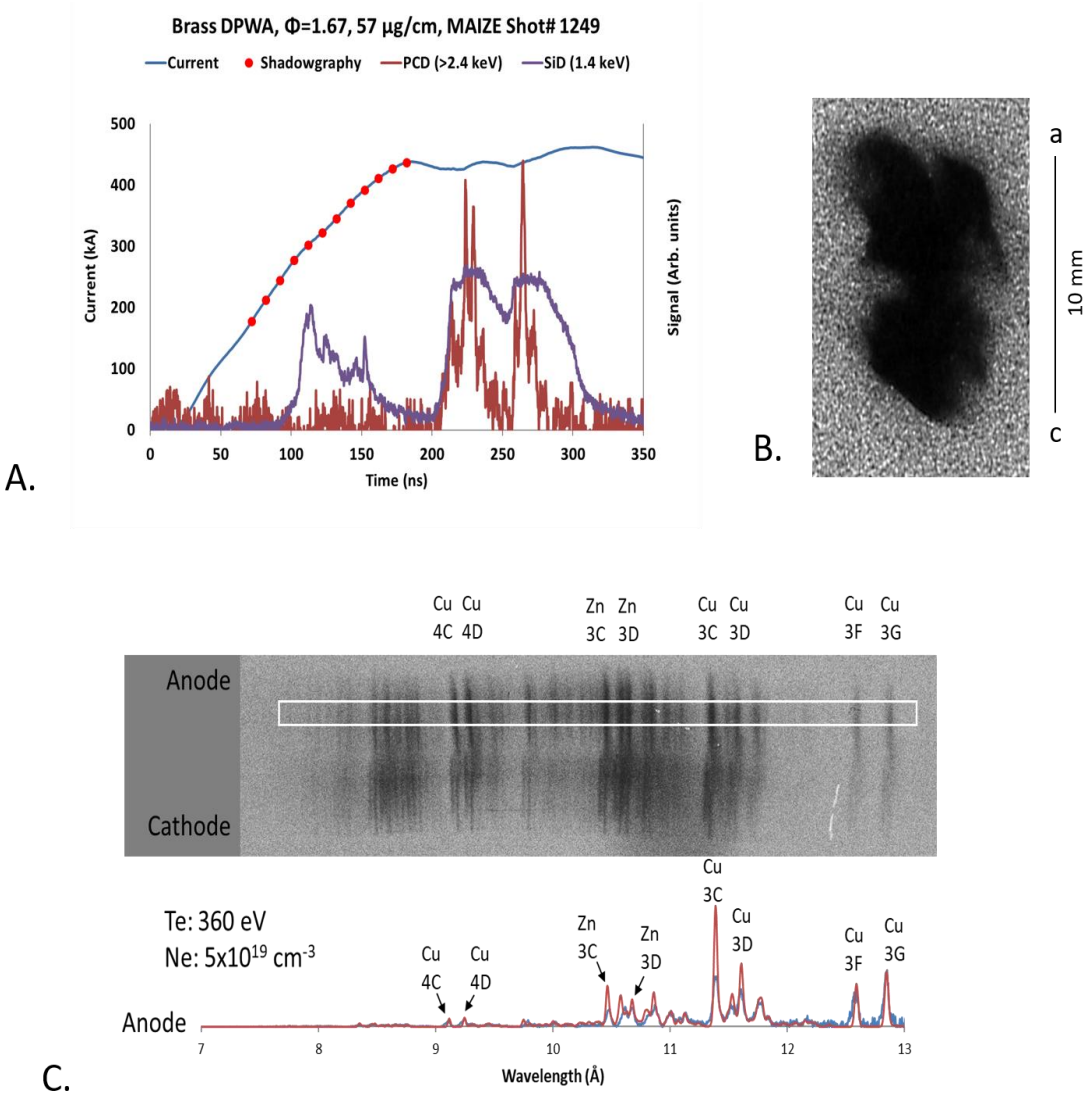


Figure 20: Brass DPWA, $\phi = 1.67$, MAIZE Shot 1249. A. Radiation output from MAIZE shot 1249 (6/6, interplanar gap = 3 mm, interwire gap = 1 mm, aspect ratio $\phi$=1.67, array mass = 57 µg/cm). The PCD signal (dark red) shows radiation in the > 2.4keV region, while the Si-diode signal (purple) shows the radiation signal in >1.4 keV spectral band. Current (blue) rise time was 180 ns with main implosions occurring at 200–240 ns and at 255-280 ns from the start of current. Red dots correspond to moments when a shadowgraphy image was taken (see Figure 21). B. Time-integrated pinhole image in the >1.4 keV x-ray region from pinhole camera #1 (looking from the side, ~90° from the space between the planes). C. 1D spatially resolved, time integrated x-ray spectrum is compared to theoretical modeling to find plasma conditions of $T_e$=360 eV and $N_e$=5x10$^{19}$ cm$^{-3}$ near the anode.

Figure 21 shows the shadowgraphy images taken throughout the implosion of MAIZE Shot 1249, from 72 ns to 182 ns after the start of current, alongside WADM simulations of the same time. From these images it can be seen that mass accumulation along the central axis formed a central "precursor" column (the precursor column is the accumulation of early ablated mass that gathers along the central axis prior to the pinch), beginning around 82–92 ns after the start of current. However, it can also be observed that the other precursor column "bent" towards one side of the load. The cause of this asymmetrical earlier formation is not yet fully understood. It can also be observed that there is a noticeable rise in the brightness of the central precursor column, beginning at 102 ns, as the central column began to draw some current away from the planes. This can be perceived in the shadowgraphy images as the background (the brighter areas not consisting of the ablating wires and central column) becomes noticeably darker, as the radiating column becomes a source of light, impeding the laser light source. This also corresponds to the beginning of the earliest (and lowest magnitude) radiation burst in the >1.4 keV band (see Figure 20A). Standing shocks can also be observed, forming around the 102 ns mark (see ref. [25] for a detailed explanation of standing shocks and how they form]. WADM modelling showed good correlation with the shadowgraphy images as well. The WADM showed mass accumulation along the central axis beginning around 82 ns, and drastically increasing around 102-112 ns. Likewise, the WADM model shows an increase in mass accumulation around the central precursor column beginning around 102-112 ns, correlating to the formation of the standing shocks. The mass accumulation along the central axis beginning to draw current from the outer ablating wires into the central axis

causes a noticeable “dip” in the current trace (though not as drastic as the main pinches), which corresponds to a raise in the load inductance.

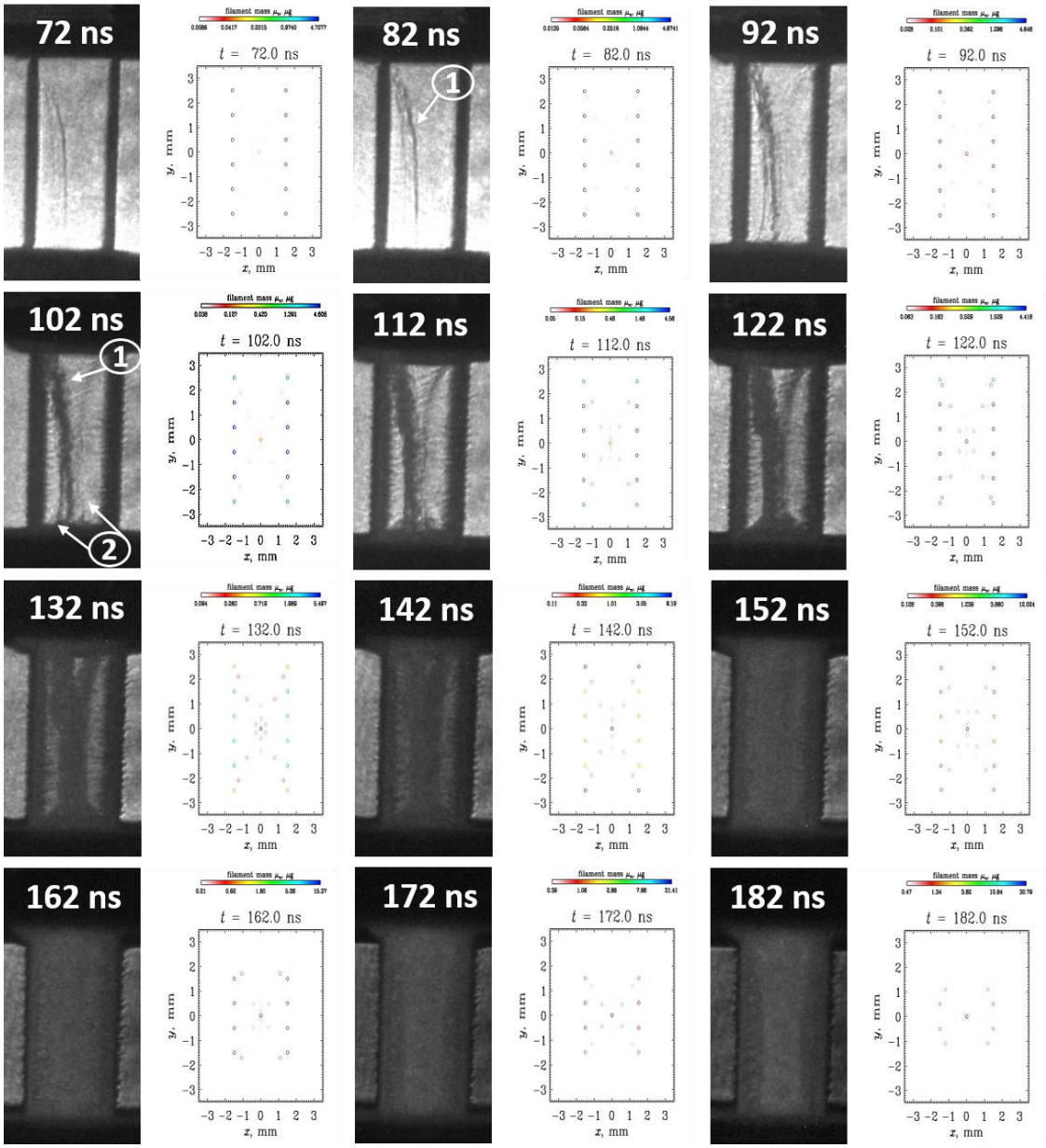


Figure 21: Side-by-side comparison of shadowgraphy images and WADM modelling from MAIZE shot 1249 show the implosion evolution in time from the start of current. The central precursor column is highlighted with a ①, while the standing shocks are labelled with a ②. Note the drop in background brightness at the 102 ns mark.

The x-ray diode signals and current trace for the higher aspect ratio Shot 1250 (8/8, interplanar gap = 3 mm, interwire gap = 1 mm, aspect ratio $\phi$=2.33, array mass = 76 μg/cm), are shown in Figure 22A. Similar to the lower aspect ratio load, the higher aspect ratio load featured two distinct radiation bursts which were detected in both the >1.4 keV band by a filtered Si-diode, and the >2.4 keV band, detected by the PCD. However, the first x-ray burst in the >2.4 keV region reached a much higher relative peak than the second, later burst in the >2.4 keV band. The current risetime was slower than on the lower aspect ratio, with the current reaching its peak at 210 ns after the start of current. The first x-ray burst in the >2.4 keV region followed soon after, beginning at approximately 220 ns and radiating up to 245 ns. The second burst in the >2.4 keV band began radiating much later, at about 280 ns and continued radiating up to 300 ns. Unlike in the lower aspect ratio load, the first burst was much more intense than the secondary burst, reaching a much higher relative maximum peak. This is likely due to the additional mass imploded, as Shot 1250 was more massive than Shot 1249. There was a large break between the two distinct peaks, from 245 ns to 280 ns, in which the load was not radiating, or radiating very little, in the >2.4 keV band. However, the load continued to radiate in the >1.4 keV band consistently from 225 ns to 315 ns, reaching relative peaks at 235 ns and 285 ns, which corresponded to the relative maximum peaks in the >2.4 keV band as well.

The TIPH images shows a fairly uniform x-ray emission in the >1.4 keV spectral band, with the majority of x-rays emitting from the central column (see Figure 22B). The non-LTE modeling of L-shell spectra of Cu and Zn from MAIZE Shot 1250 (Figure 22C) revealed an electron temperature of 360 eV and density of $5x10^{19}$ $cm^{-3}$, and evidence of

optically thick Cu 3C and Zn 3C Ne-like lines near the anode, with similar parameters ($T_e$ = 350 eV and $N_e = 3x10^{19}$ $cm^{-3}$) and a less optically thick Cu 3C line near the cathode.

We see a small burst early in time, from 75 ns to 150 ns from the start of current. Once again, this less intense, early x-ray burst in the >1.4 keV band corresponds to the formation of the precursor column (see Figure 23). Again, once the precursor column has accumulated enough mass, a portion of the current begins to flow through the column, resulting in low levels of radiation. It can also be observed that standing shocks form around the 74 ns point, however these seem to have dissolved by the 104 – 114 ns point. This is an interesting phenomenon, as these standing shocks have not been observed in DPWAs of this high of aspect ratio on the Zebra generator, as the wide array width makes it difficult for the global magnetic field to penetrate into the interior of the array, causing mass to accumulate along the saddle points [25]. While the shocks are short lasting, their formation indicates that the global magnetic field was able to penetrate the interior of the load during the current rise. This is likely due to the lower current and energy of the MAIZE machine, as the current going through each plane created magnetic fields that operated, somewhat, independently from the each other. Once the current was suitably high, however, this seemed to have dissolved the standing shocks as the magnetic fields from each plane were joined into one global magnetic field. This has likely not been observed on the Zebra generator for this high of aspect ratio, as the high current, energy, and risetime of the Zebra generator do not allow for this to occur on higher aspect ratio loads, as it does for low- and mid-range aspect ratios. The WADM modelling showed good correlation with the formation of the precursor column, as it demonstrates an increase in the mass accumulation along the central axis beginning around the 74 ns point.

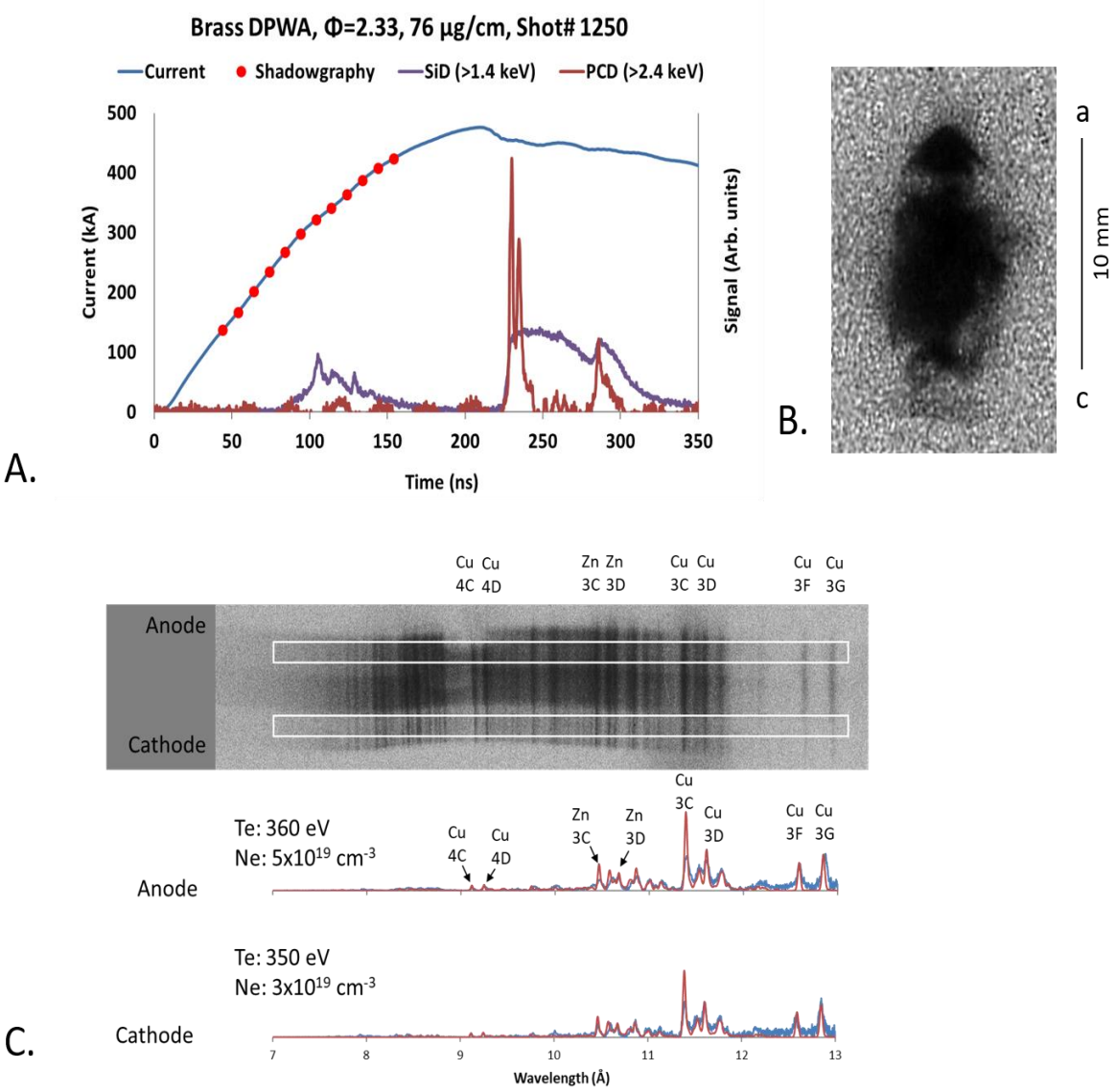


Figure 22: Brass DPWA, ϕ=2.33, MAIZE Shot 1250. A. Radiation output from MAIZE shot 1250 (8/8, interplanar gap = 3 mm, interwire gap = 1 mm, aspect ratio $\phi$=2.33, array mass = 76 µg/cm). The PCD signal (dark red) shows radiation in the > 2.4keV region, while the Si-diode signal (purple) shows the radiation signal in >1.4 keV spectral band. Current (blue) rise time was 200 ns with the main implosion occurring at 220–245 ns and a smaller, secondary implosion occurring at 280-300 ns from the start of current. Red dots correspond to moments when a shadowgraphy image was taken. B. Time-integrated pinhole image in the >1.4 keV x-ray region from pinhole camera #1 (looking from the side, ~90° from the space between the planes). C. 1D spatially resolved, time integrated x-ray spectra are compared to theoretical modeling to find plasma conditions of $T_e$=360 eV and $N_e$=5x10$^{19}$ cm$^{-3}$ near the anode and $T_e$=350 eV and $N_e$=3x10$^{19}$ cm$^{-3}$ near the cathode.

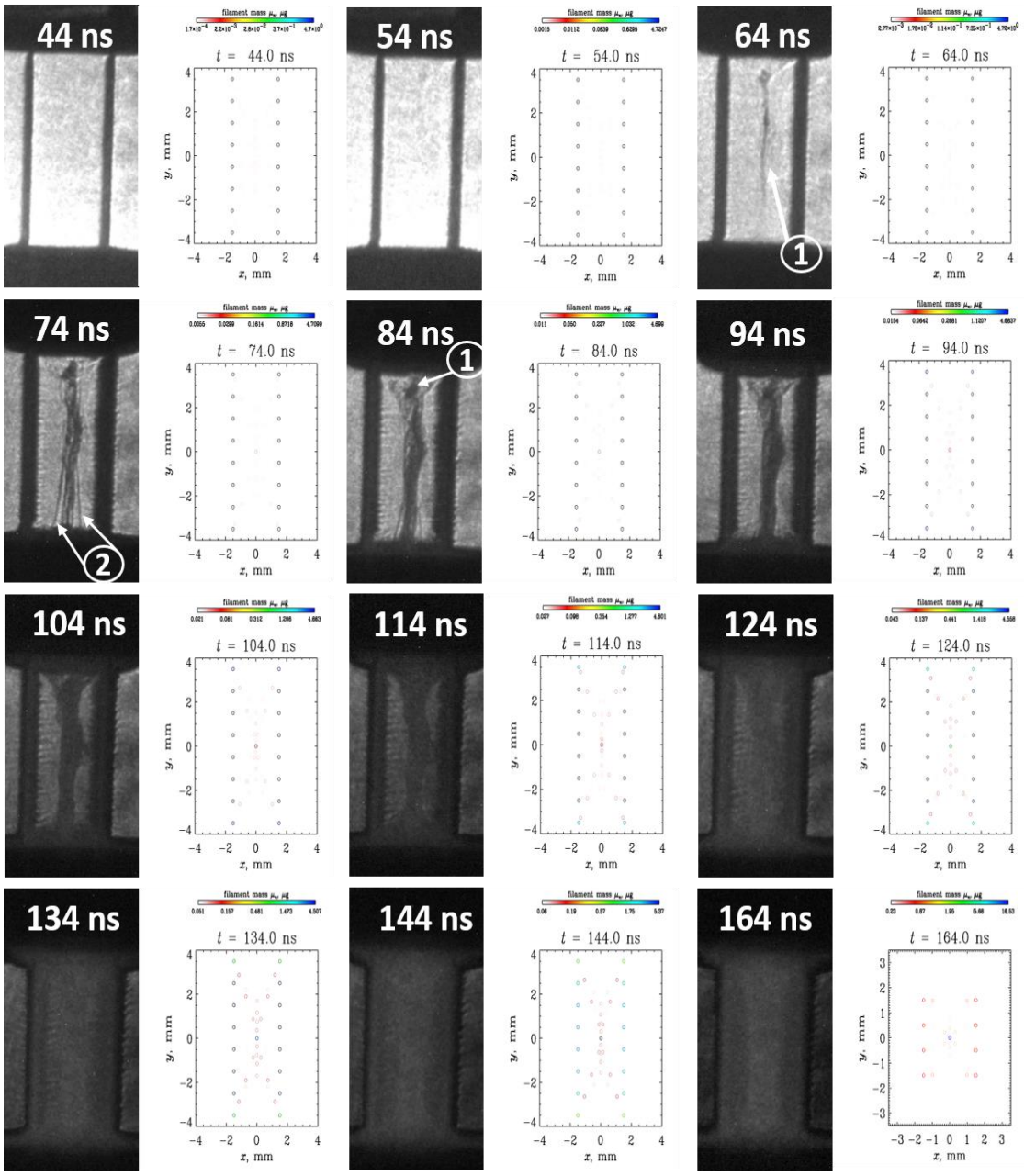


Figure 23: Side-by-side shadowgraphy images and WADM simulations from MAIZE shot 1250 show the implosion evolution in time from the start of current. The central precursor column is highlighted with a ①, while the standing shocks are labelled with a ②. Note the drop in background brightness at the 74 ns mark.

## 4.11 Inductance Modelling of Mid-Atomic-Number DPWAs of Different Aspect Ratios on MAIZE

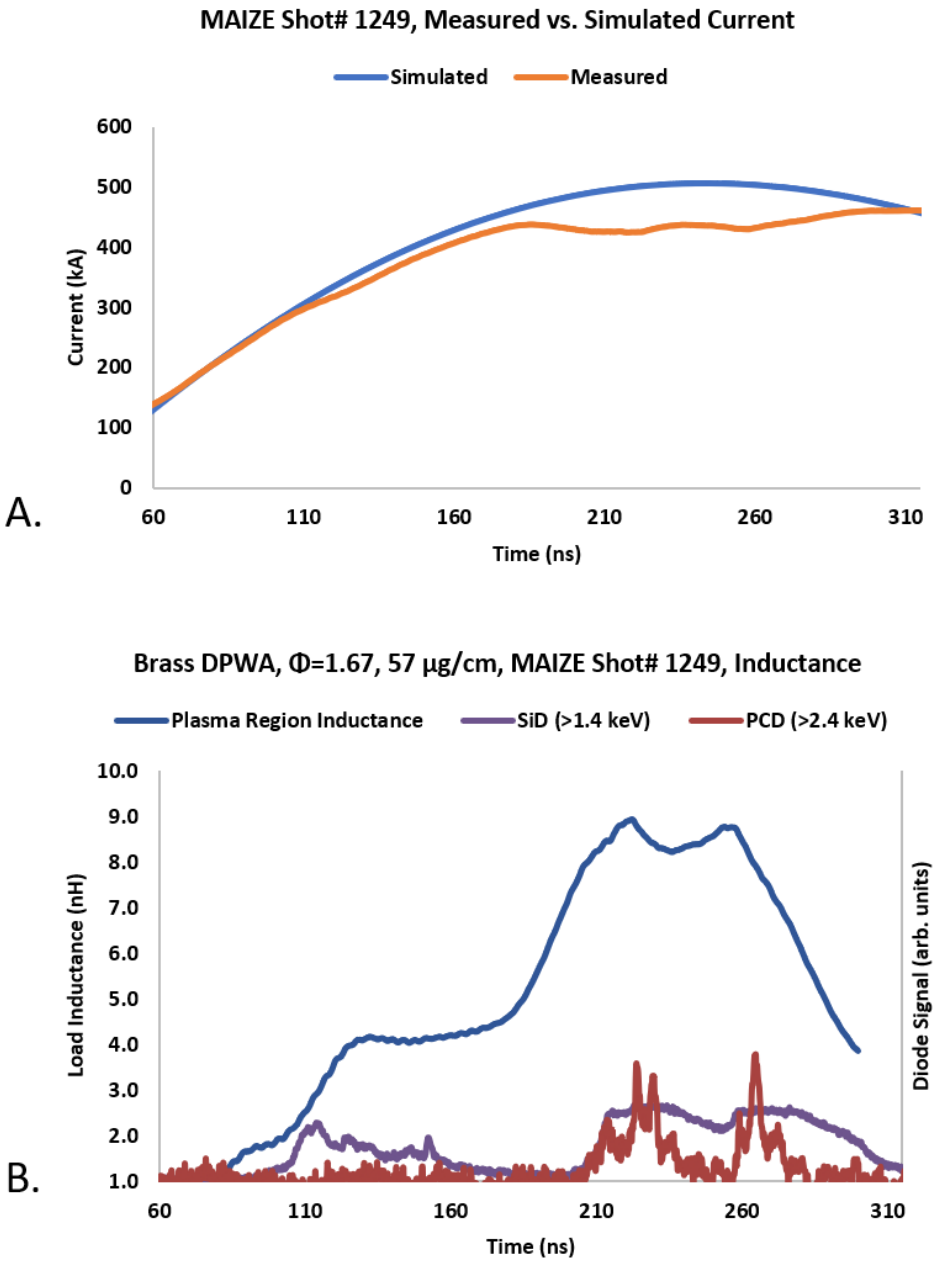


Figure 24: Inductance calculations from brass DPWA MAIZE Shot 1249. (A) Comparison of simulated current (blue) to the experimentally measured current (orange). (B) Time-dependent load plasma region inductance throughout the implosion (dark blue), plotted with >1.4 keV (purple) and >2.4keV (dark red) x-ray signals.

As is shown in Figure 24, the relative maxima in the inductance showed good correlation with the timing of x-ray bursts. The inductance begins to rise sharply around 90 ns after the start of current, coinciding with the formation of the standing shocks. The first relative maxima of 4 nH is reached at approximately 125 ns after the start of current, which corresponds well to the first, less intense x-ray burst in the >1.4 keV band, and the formation of the precursor column. Similar to the x-ray bursts, the inductance also reached two relative maxima at 220 ns and 255 ns. The first inductance peak of the main bursts, occurring at 225 ns, reached an overall maximum of 8.9 nH, while the second inductance peak reached a relative maximum of 8.7 nH at 255 ns. Typically, the peak inductance correlates with the strength of the pinch, which coincides with the intensity of the x-ray burst, as the inductance if directly correlated to the effective current carrying radius. A smaller pinch radius typically correlates to a hotter and denser plasma, and a higher x-ray output. It should be noted that, while both peaks of the main x-ray bursts reached approximately the same peak amplitude, the first x-ray burst (occurring at 225 ns) had a much longer duration of x-ray emission than the proceeding, final burst, making for a higher overall x-ray flux, thus it makes sense that the overall maximum inductance peak occurred simultaneously with the first peak of the main x-ray burst at 225 ns.

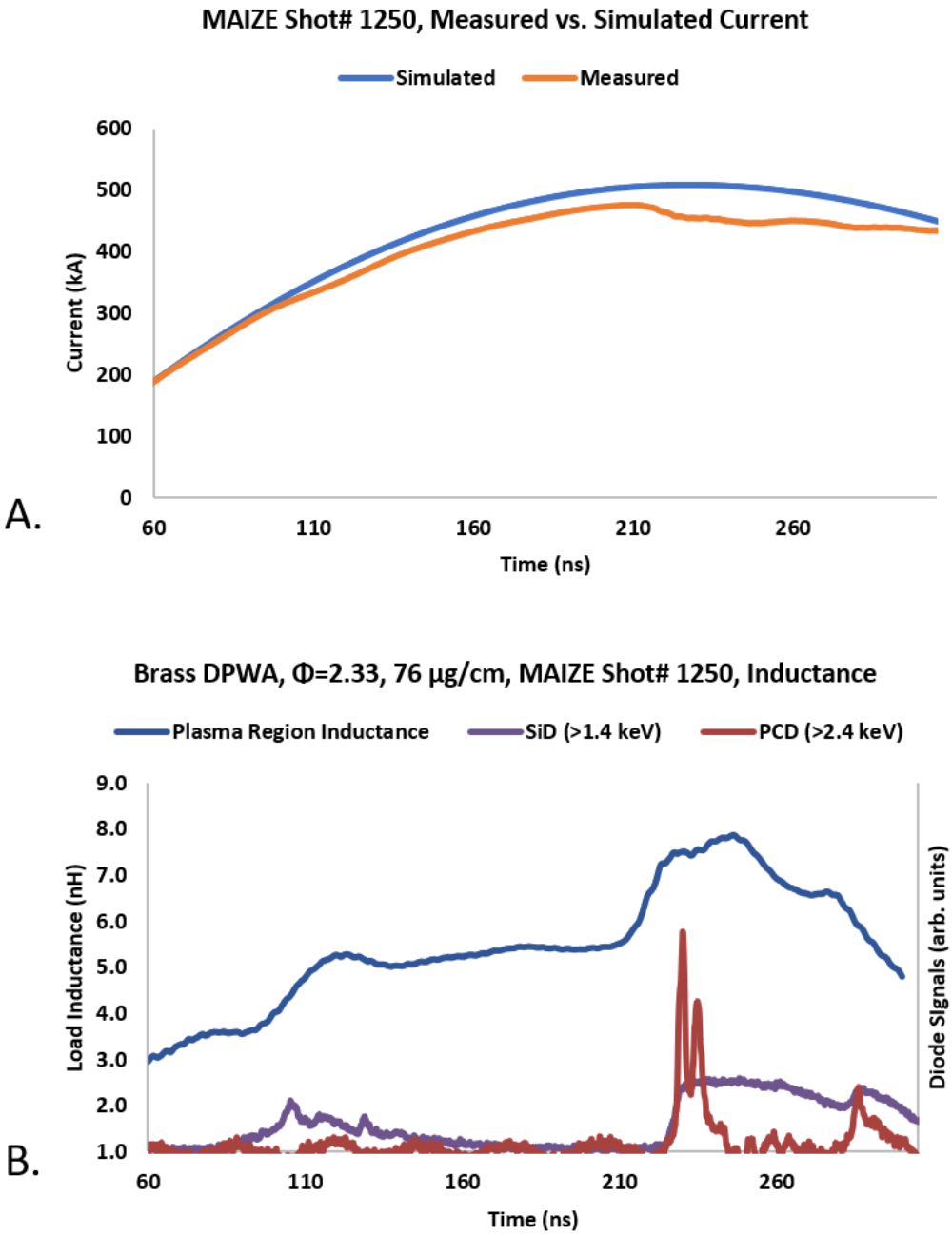


Figure 25: Inductance calculations from brass DPWA MAIZE Shot 1250. (A) Comparison of simulated current (blue) to the experimentally measured current (orange). (B) Time-dependent load plasma region inductance throughout the implosion (dark blue), plotted with >1.4 keV (purple) and >2.4keV (dark red) x-ray signals.

From Figure 25, we can see that the higher aspect ratio, $\phi = 2.33$, brass DPWA MAIZE Shot 1250 followed a similar inductance time-development as the lower aspect ratio, $\phi = 1.67$, MAIZE Shot 1249. In MAIZE Shot 1250, the inductance began rising sharply at 90 ns, around the time when the precursor column began to form. The inductance reached its first relative maximum of 5.3 nH at 125 ns, around the time when the precursor column fully formed. The inductance then decreased and remained nearly constant before rising again for the main pinch. During the first x-ray burst of the main pinch, at approximately 230 ns, the inductance reached a short-lived relative maximum of 7.5 nH at 230 ns, before quickly rising to its overall maximum of 7.8 nH at 245 ns, which correlated well in time to the main x-ray burst. The inductance then decreased before reaching its final relative maximum of 6.6 nH at 280 ns, coinciding with the final, less intense x-ray burst. It is interesting that the lower aspect ratio MAIZE Shot 1249 reached a higher maximum inductance of 8.9 nH, almost 1 nH higher than the maximum reached by the higher aspect ratio MAIZE Shot 1250, despite the x-ray burst being of lower intensity than the main x-ray burst of MAIZE Shot 1250. While this phenomenon is not fully understood, it could have been caused by a non-uniform plasma column in Shot 1249, where a region of the plasma column may have reached a smaller radius, causing a spike in the inductance, while Shot 1250 may have had a more uniform radius throughout the pinch, causing it to be more emissive of >2.4 keV radiation, but not to reach as high of an average inductance. While unconfirmed, the theory of an asymmetric pinching column during the implosion for MAIZE Shot 1249 could have been caused by the early development of one plane beginning to implode sooner than the other (this can be observed in Figure 21, as the precursor column appears to be “bent” more towards one imploding plane).

## 4.12 Conclusions and Discussion

It was predicted that LTD generators allow for greater efficiency than previous machines designed around Marx bank technology [84], [85]. In order to measure the efficiency, the x-ray yield must be measured. The x-ray yield of the more massive Al DPFL, the less massive Al DPWA, and the W DPWA were measured using the absolutely calibrated PCD x-ray detector. In these experiments on the MAIZE LTD generator, the x-ray yield in the >2.4 keV band of the more massive Al DPFL was $3.3 \times 10^{-2}$ J, and thus the conversion efficiency was $\varepsilon_{\text{Al DPFL}} = 4.2 \times 10^{-6}$. The optimized, less massive Al DPWA was only twice as large at $6.7 \times 10^{-2}$ J, and thus $\varepsilon_{\text{Al DPWA}} = 8.5 \times 10^{-6}$. Spectroscopic modelling of both the Al DPFLs and Al DPWAs showed comparable electron temperatures ($T_e$) and densities ($n_e$): $T_{e,}^{\text{DPFL}} = 310\text{-}340$ eV, $n_{e,}^{\text{DPFL}} = (1\text{-}5) \times 10^{19}$ cm$^{-3}$ (I = 0.56 MA), and $T_{e,}^{\text{DPWA}} = 375\text{-}380$ eV, $n_{e,}^{\text{DPWA}} = (1\text{-}3) \times 10^{19}$ cm$^{-3}$ (I = 0.59 MA). Additionally, the Al DPWA was found to be optically thin near the anode, in contrast to typical Al plasmas on the Zebra generator [80], [88]. Also, the electron temperature was measured to be hotter near the cathode and cooler near the anode.

The W DPWA was the strongest radiator by far, with the total energy emission (1.6 J) and efficiency ($\varepsilon_{\text{W DPWA}} = 2.1 \times 10^{-4}$) being almost 25 times higher than the Al DPWA on the MAIZE machine.

The result of the heavy, mass-unoptimized Al DPFL producing a comparable overall x-ray output to the mass-optimized Al DPWA, suggests that a mass-optimized DPFL could perform as well as, if not better than, a DPWA of similar mass. This would suggest that DPFLs could still serve as promising replacements for wire array configurations, as was theorized in ref. [35], but more experiments are needed to say for sure.

Both the Al DPFL and the Al DPWA reached peak inductance prior to maximum current. The maximum load inductance of the Al DPFL never reached as high of a peak as the Al and W DPWAs, implying less current transfer to the central plasma column and thus weaker pinching. The duration of occurrences of local maxima throughout the primary x-ray emission period last much longer in the Al DPFL experiments than in the Al DPWA and W DPWA experiments. The Al DPWA reached a maximum load inductance of 4.5 nH and an x-ray yield of 67 mJ, implying a stronger pinch than the Al DPFL, which reached a maximum inductance of 3.5 nH and a >2.4-keV x-ray yield of 33 mJ. The W DPWA demonstrated the strongest pinch overall, reaching a maximum load inductance of 9 nH (slightly after peak current) and a >2.4-keV x-ray yield of 1.6 J. The time-dependent inductance histories of all three loads tested were strongly correlated with the waveforms from the measured x-ray emissions. These promising results warrant future studies of both foil liners and wire arrays on LTD generators and will help in optimizing future load configurations. We note in particular that the longer emission history from the DPFL could be useful for x-ray pulse shaping applications, if we can demonstrate better control over the waveform in future experiments. This will require significant computational design work as well as experimental validation.

In addition to the low-atomic-number Al DPWA and DPFL, and the high-atomic-number W DPWA, two mid-atomic-number brass DPWAs of different aspect ratios ($\Phi$=1.67 and $\Phi$=2.33) were also imploded on the MAIZE LTD generator; both began radiating in the >1.4 keV band around 105-115 ns, when the precursor formed, and both demonstrated two distinct radiation bursts in both the >1.4 keV band and the PCD (>2.4 keV) at the time of implosion, and featured an approximately 200 ns current risetime prior

to implosion. The lower aspect ratio, MAIZE Shot 1249 had a total energy output in the >2.4 keV band of 0.53 J and reached a maximum load inductance of 9 nH, while the higher aspect ratio, MAIZE Shot 1250, had a total energy output of 0.77 mJ and reached a maximum load inductance of 8.5 nH.

Similar loads imploded previously on the high-impedance Zebra Marx bank generator demonstrated one main burst lasting approximately 60 ns, immediately preceding the current peak ~90 ns from the start of current. The slower current rise-time and "bursty" x-ray behavior on the MAIZE LTD is attributed to the low-impedance of the machine, while the high-impedance Zebra Marx bank has a much faster rise-time and well-defined main x-ray burst.

Due to the low impedance of the MAIZE LTD generator, the change in inductance of the load throughout the implosion had a significant effect on the current trace throughout the implosion. This effect was exploited to estimate the time-dependent inductance of the load through the implosion, which correlated well in time with the radiation bursts. Implementation of this technique on the Zebra generator is in development, however the current trace of the high-impedance Zebra machined is less impacted by the changes of the load inductance throughout the implosion; and the complexity of the accurately modelling the full circuit model of Zebra presents further complications to be addressed in future publications.

WADM modeling on the brass DPWAs on MAIZE showed good correlation with shadowgraphy images and radiation bursts, as did previous WADM modelling on brass DPWAs on the Zebra machine. Spectral modelling of the brass DPWAs on MAIZE revealed relatively uniform electron temperatures on the order of 360 eV and density of

$5x10^{19}$ $cm^{-3}$, which is cooler than similar loads on the Zebra generator (400-450 eV), but on a similar order of density ($10^{19}$ $cm^{-3}$) [63]. This cooler plasma temperature on MAIZE is due to the lower maximum current (~500 kA on MAIZE vs. ~1 MA on Zebra). However, the most intense L-shell Cu and Zn lines were optically thick in experiments on both Zebra and MAIZE.

These results demonstrate many significant findings. The first, is that the overall physical processes of DPWA implosions (development of standing shocks, precursor development, radiation burst, and primary implosion) are consistent over a variety of metals, and across different MA-class drivers of different architectures [63], [64]. Second, the tendencies to radiate from non-LTE K- and L-shell emission as a function of atomic-number are similar between MAIZE and Zebra, from measurements of X-ray energy in several bands. Lastly, an electrical, rather than optical, diagnostic has been developed on MAIZE to estimate the plasma region inductance throughout a wire array pinch, which accurately captures pinch timing, and is somewhat informative on pinch strength (verified by optical diagnostics over a variety of DPWA dimensions and materials), enabling future experiments designed to investigate x-ray emission amplitude and duration to be fielded with minimal and easily realizable diagnostic capabilities. These findings help to show that wire array experiments across both larger and smaller university-scale pulsed power facilities yield similar results, which, in turn, demonstrates that experiments on university-scale machines like these could help to inform experimental designs on larger facilities.

# 5 Sparky tabletop Hard X-Ray Source (Sparky-HXRS)

## 5.1 Introduction and Motivation

Experiments were performed using the newly developed table-top "Sparky Hard X-ray Source" (also called "Sparky-HXRS") a modified version of Sparky III [91] at the University of Nevada, Reno. The Sparky-HXRS device is a newly developed table-top hard x-ray source, based off the concept of a vacuum discharge with a laser triggering (see Figure 26 and Figure 27). The development of the Sparky HXRS with a moderate-current vacuum diode with laser-plasma cathode triggering has been performed for the study of x-ray characteristic radiation and spectropolarimetry. Sparky-HXRS was extensively used for development of x-ray diagnostics, and training of students in pulsed power sciences. Important results of experiments with this device are shown and discussed in this manuscript. High-atomic-number atomic number L-shell (tungsten) and mid–atomic-number K-shell (stainless steel and brass) spectroscopic measurements have been focused on studying the atomic properties and polarization characteristics of hard x-ray radiation in the >6-15 keV spectral region. The Sparky-HXRS is designed modularly, such that it can, theoretically, study bremsstrahlung and characteristic radiation from a variety of metals, depending on four primary experimentally chosen criteria: the anode material, the cathode material, the size of the laser focusing spot, and the chosen anode voltage.

The vacuum diode consists of a planar slab as a cathode and a conical anode placed in a vacuum chamber evacuated to $10^{-5}$ Torr. An electrical circuit of the HXRS consists of the grounded cathode, the anode, and the capacitor that were placed between the anode and the ground. A pulsed Nd:YAG laser beam was focused on the cathode to produce the laser

plasma, which expands towards the anode. In contrast to cathodes with explosive electron emission or field emission, laser-plasma cathodes can work with any accelerating voltage. Particularly, under optimal voltage, they provide for an increased degree of monochromatization and decreased production of Bremsstrahlung radiation. Electrons from the sheath region of the expanding plasma are accelerated towards the tip of the conical anode, which leads to generation of bremsstrahlung and characteristic x-ray radiation. The x-ray emission from the anode starts with the formation of plasma on the cathode and stops with the shortening of the diode gap with the arrival of the plasma boundary at the anode. At this stage, high current flows into the diode and the anode voltage falls rapidly.

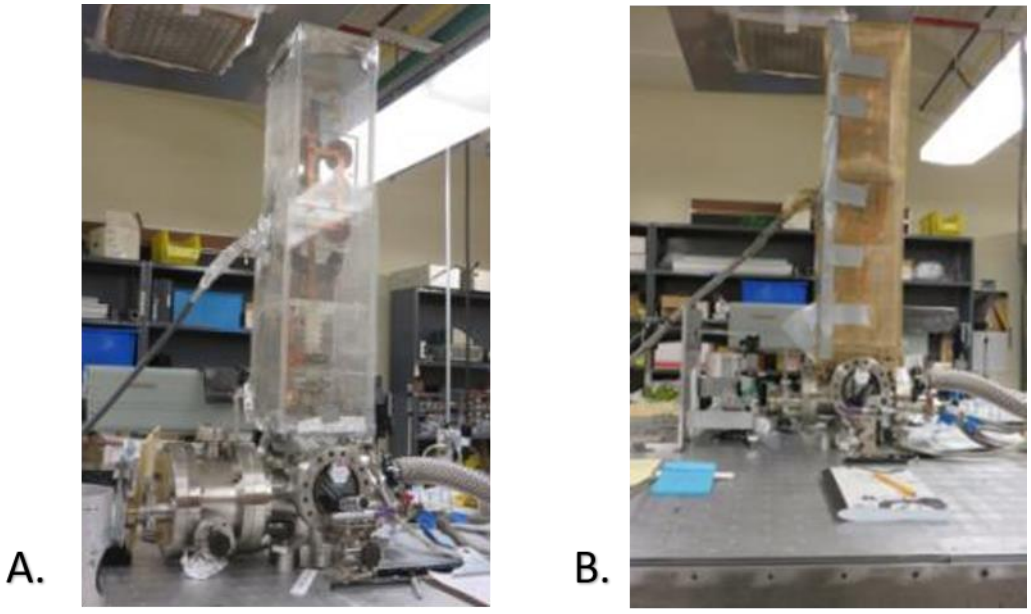


Figure 26: Sparky-HXRS hard x-ray source. A. First configuration (FC) with current up to 1.2 kA. B. Second configuration (SC) with current up to 12 kA.

An analysis of the processes in this hard x-ray source must include several other aspects. It is well established (see refs. [92], [93]) that characteristic x-ray emission from

multiply charged ions is produced in a high-current vacuum spark, in which the plasma is produced due to electrode erosion. It is commonly believed that the micrometer-size regions of a high-temperature plasma (‘hot spots’) are the source of ion generation, reaching an electron temperature of up to several kiloelectronvolts [94]. These hot spot regions are attributed to small regions of pinching in the *current-carrying* plasma column withing the electrode gap. Commonly referred to as micropinches, these are formed at a sufficiently high voltage (a 20-50 kilovolts) and a high current (about 40-100 kA) [95]. The *current free* plasma jet that is formed under irradiating of a target with a laser pulse is another source of x-ray emission and accelerated particles. In which, the absorption of the light pulse energy from the laser is a source of heating and acceleration of plasma particles in the jet [96].

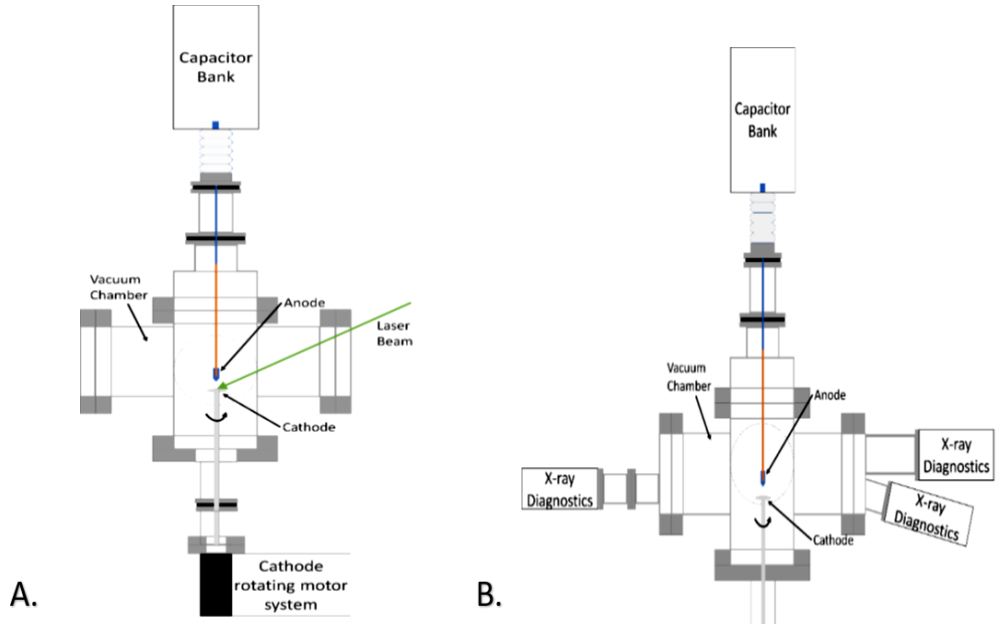


Figure 27: Structure of the Sparky III-HXRS source. A. View of the vacuum chamber from the laser beam window. B. View of the top part of the vacuum chamber with x-ray diagnostics.

It should be emphasized that production of local hot plasma areas in both types of sources mentioned above requires a lot of energy contributions and can be a rather expensive process. However, a promising and efficient way of producing local plasma heating is integration of both types of these sources (vacuum spark and laser plasma) into a laser triggered vacuum discharge. In refs. [97]–[100], it was demonstrated that if a bias voltage was applied between a target (acting as a cathode) and a specified electrode (acting as the anode), and a laser pulse striking the cathode was used to initiate a laser plasma, then hot spots were formed within the laser triggered, *current-carrying* plasma jets. It was suggested that the formation of these hot spots was due to the pinching of plasma in the cathode microjets, and it was these micropinches that presented the sources of x-ray emission with energies in the range 0.1–10 keV. These micropinches were found to radiate mainly in the soft x-ray regions, and the x-ray emission was relatively weak compared to the x-rays emitted from the anode. However, the micropinches were found to emit electron beams of abnormally high energy (the highest even reaching energies as high as 100 keV, which was an order of magnitude higher than the discharge voltage of the anode-cathode gap). These abnormal electron beams could contribute to the formation of plasma on the anode surface, and could be the source of some irregular activity in the emission of hard x-ray spectra from the anode [101].

In previous publications, hot spots were shown to be formed in the cathode microjets in the immediate vicinity of the cathode surface. These microjets were investigated at discharge currents of 1-10 kA, and were presented in ref. [102], where experimental laser triggered vacuum discharges with relatively low current (1-10 kA, 10-20 kV voltage, and 5-100 J of capacitor energy) were investigated. These hot spots were

found to be formed within micropinches, which form in the initial stage of the discharge as thew initial laser plasma jet from the cathode is expending out into the interelectrode gap.

A micopinch can form in the case where a laser-induced plasma jet expands into a vacuum from a cathode leading to an anode. However, the successful formation of a micropinch depends on the conditions of the experiment: both the discharge current and the initiating laser energy must lie within a specified range of values, which are determined by the interelectrode gap [102]. Evidently, the conditions of the laser-initiated pre-plasma has a large effect on the formation of micropinches in the cathode plasma jet of a vacuum discharge [103]. Both experiments and simulations have shown that the higher production of pre-plasma causes the micropinch to form farther away from the cathode, which, in turn, causes the output energy of the micropinch to decrease. In the case where the pre-plasma is over-produced, the micropinch has no time to form because the neck, formed by magnetic compression, gets carried away by the plasma flows beyond the interelectrode gap, preventing any possibilities for a micropinch [103].

In ref. [104], it was found that, for fixed laser energy and pulse duration, an increase in the focal spot size on the cathode surface led to an increase in the ablation mass of the cathode material, which then led to an increase in the subsequent discharge plasma. This was confirmed with work presented in ref. [105], which found that the parameters of a low-powered laser-induced micropinch plasma in a vacuum discharge were increased by expanding the focal spot of the laser beam on the cathode. It was found that the defocusing of the laser beam transformed the laser-induced plasma on the cathode from a spherical expansion to a jet expansion at the ignition stage of the discharge. This change formed the

most optimal conditions for effective pinching, leading to an increase in plasma density and temperature [105].

Both the laser-pulse energy, determining the mass of evaporated plasma-producing material from the cathode, and the discharge current, determining the plasma pinching rate, were found to have a large effect on the soft x-ray generation efficiency in a laser-triggered vacuum discharge [106]. If the laser-produced jet material mass is too small, the plasma produced will not meet the conditions, compression and heating, withing the micropinch to facilitate the steady generation of soft x-rays. However, if the produced mass is too high, the current is inhibited, preventing the current from reaching a high enough level to facilitate the necessary compression and heating [106]. Essentially, when trying to experimentally form a micropinch in a laser-triggered vacuum discharge, the main determining factors include the laser pulse energy, the laser focusing spot size on the cathode, the laser-pulse duration, and the current pulse through the laser-induced discharge.

## 5.2 Experimental Details

To date, multiple cathode materials have been tested, including aluminum (Al), titanium (Ti), copper (Cu), and tungsten (W). The cathode slab revolved on a rotating motor system.

The anode materials tested included stainless steel (SS304, mainly composed of Fe – 72%, Cr – 18 %, Ni – 8%, and Mn – 2%), brass (mainly composed of Cu – 70% and Zn – 30%), Ti, and W. Two different anode structures were tested as well: the first design was a conical tip, which consisted of a metal tipped (W or brass) with another metal (brass) as a holder (see Figure 28A); the second design, which consisted of a metal as a holder (Ti,

brass, SS304) and an extended conical tip of another metal (W, Ti, SS304) (see Figure 28B).

The electrical circuit consists of the grounded cathode, the anode (biased at +10 kV to +27 kV, for the purpose of these experiments), and capacitor/s that was placed between the anode and the ground. Two different capacitor configurations were used on this machine. The first configuration (First Configuration-FC) was with a $C_1$ = 12 nF capacitor bank (made up of six 2 nF high voltage capacitors placed in parallel) which was operated up to a maximum voltage of $V_1$ = 27 kV, energy collected in capacitor bank was up to $E_1$ = 4.6 J, total low inductance of the discharge circuit was near $L_1$ = 0.53 μH, the period of the current oscillations was of $T_1$ = 0.5 μs. Typical current was 1 – 1.2 kA. The inductance of the Sparky-HXRS circuit was calculated by approximating it as a simple RLC circuit and using the known relation of current oscillation frequency to inductance and capacitance,

$$T = 2\pi\sqrt{L \times C},$$

Equation 18

where *T* is the period of oscillation, *L* is the inductance, and *C* is the capacitance. The second configuration (Second Configuration-SC) was with a single $C_2$ = 0.6 μF high voltage capacitor operated up to a maximum voltage of $V_2$ = 23 kV, energy collected in capacitor was up to $E_2$ = 157 J, total inductance of the discharge circuit was near $L_2$ = 0.58 μH, the period of the current oscillations was of $T_2$ = 3.7 μs. Typical current was 10 – 12 kA. The anode-cathode gap was set at d = 8 mm in both configurations.

A.  B. 

Figure 28: A. Original conical anode shape tested. B. Updated anode style, with an extended tip.

Triggering of the discharge was performed by a laser beam focused on a flat cathode surface (made from Al, Ti, Cu, or W) in a spot with a diameter of about 1.2 mm and to produce a laser plasma which expands upwards towards the anode. A Nd:YAG laser beam was used to initiate the discharge, which had the following parameters: using various filters the laser energy ranged from $E_l$ ~15 mJ up to 300 mJ (in most experiments $E_l$ was 50 mJ), pulse duration at FWHM ~5 ns, wavelength of 1.064 μm). The intensity of the laser radiation in the focusing spot in most experiments q varied in the interval $10^9 – 10^{10}$ W/cm$^2$. The laser filters used allowed for testing in four different energies: no filter, in which the pulse was at the full ~300 mJ energy; a 1/3 energy filter, which measured ~80 mJ energy; a 1/6 energy filter, which measured ~50 mJ energy; and lastly, a 1/20 energy filter, which measured ~15 mJ energy. All laser pulse energies were measured daily using a calorimeter to avoid potential errors due to laser energy fluctuations.

Experimental diagnostics were located inside and outside the vacuum chamber. Diagnostics included various filtered x-ray diodes, x-ray scintillation detector, x-ray spectrometer, x-ray pinhole camera, and a Rogowski coil for measuring the change in current through the anode. The time-resolved x-ray output throughout each shot was

measured using a side-on absolutely calibrated polycrystalline diamond detector (PCD) with a time resolution of 0.5 ns. The PCD was filtered to detect photons with energies above a cutoff energy of 8.2 keV. The cutoff energy E is defined as the energy where the transmission through the filter drops to a value of 1/e, where e is the base of the natural logarithm. The total x-ray yield in the > 8.2 keV band of a shot was approximated by integrating the signals from the absolutely calibrated PCD over the entire duration of emission and assuming isotropic radiation into 4π steradians. The PCD was placed inside of the vacuum chamber. Three side-on, cross-calibrated AXUV-HS5 Si-diodes with a time resolution of 1 ns and filtered to detect >1.4, > 8.2, and >15 keV x-rays were also used to measure the time-evolution of the x-ray output in different energy bands, and also were placed inside of the vacuum chamber. The diode detectors were aimed in such a way as to view the entirety of the anode-cathode gap. The x-ray scintillation detector (resolution was 2 ns) used to measure the time-evolution of the x-ray output in > 8.2 keV or > 15 keV energy bands.

This detector was placed outside of the vacuum chamber. The special x-ray window (with 125 μm thick kapton filter) was developed for the transportation of the hard x-ray beam (> 6 keV) outside the vacuum chamber of Sparky-HXRS into open air.

The oscilloscopes used featured a sample rate of 5 GS/s, capable of resolving the PCD and another x-ray detectors time resolution. The signals from x-ray detectors were averaged over a series of 10 shots.

Side-on time-integrated x-ray spectrometer (TISP) was applied to record the spectra produced. The TISp was fitted with a convex lithium fluoride (LiF) crystal with a double lattice spacing 2d = 4.027 Å, a radius of curvature of 25.4 mm, which measures the

relatively hard x-ray region between 1 and 3.9 Å. The TISP were equipped with 7.5-µm-thick Kapton film together with 3-µm-thick Mylar (aluminized on both sides with 0.15-µm-thick Al layers) to protect the inside x-ray film from unwanted outside light. The spectra were recorded onto Kodak Biomax MS X-ray film [86], [107]. That x-ray spectrometer was placed inside the vacuum chamber of Sparky-HXRS.

For study polarization characteristics of hard x-ray radiation in >6 keV spectral region side-on time-integrated x-ray polarimeter (TISpP) with two flat crystals has been developed (Figure 29). The TISpP is designed modularly, such that it can, theoretically, study characteristic radiation in different spectral region, depending on the chosen crystals and x-ray filters. For testing this new TISpP polarization measurements of characteristic spectra of K-shell Fe from SS304 anode was performed. In the TISpP two flat topaz crystals (303) with 2d = 2.712 Å were used. The arrangements of the crystals are selected to isolate a single-linear component of the radiation intensity. Crystal #1 transmits the perpendicular ($I_{\perp}$) and Crystal # 2 transmits the parallel intensity components ($I_{II}$) respectively, where the orientation is relative to the anode axis of symmetry (i.e. the electron beam direction) (see Figure 27).

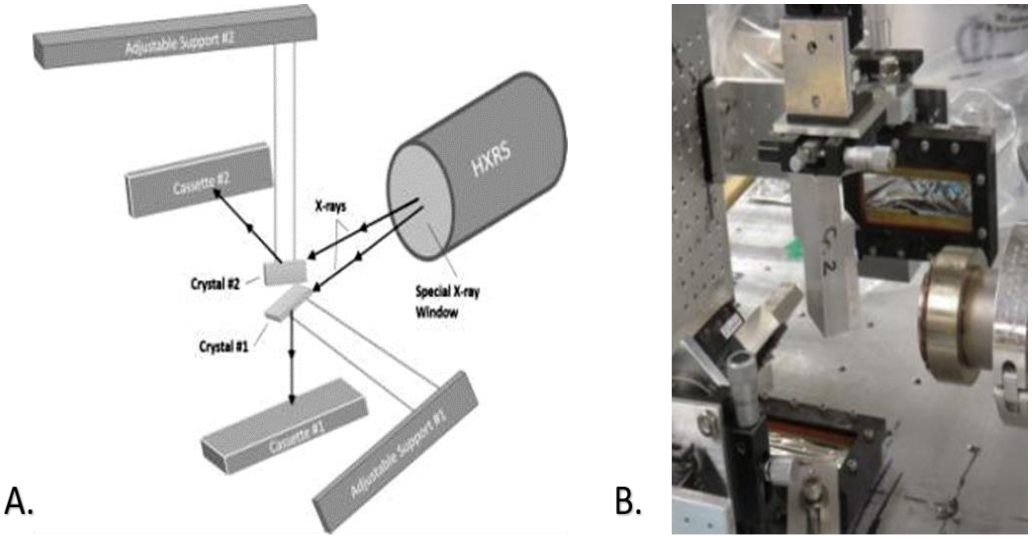


Figure 29: Side-on time-integrated x-ray polarimeter (TISpP) with two flat crystals. A. Scheme of the TISpP. B. The TISpP with cassettes for Kodak Biomax MS X-ray film (at the left and at the center) and the special x-ray window (at the right).

The TISpP was placed outside vacuum chamber with using the special x-ray window that described early in this chapter (Figure 29). The spectra were recorded onto Kodak Biomax MS X-ray film [107]. Both film cassettes were equipped with double 3-μm-thick Mylar filters (aluminized on both sides with 0.15-μm-thick Al layers) to protect the x-ray film from unwanted outside light.

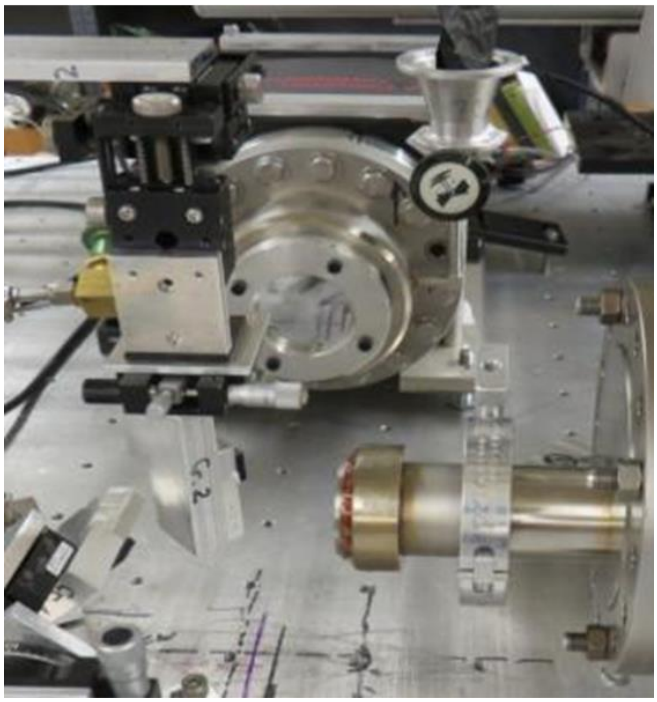

Figure 30: Testing of the TISpP with the x-ray CCD SOPHIA®-XO.

Another detector used in the TISpP was the x-ray CCD SOPHIA®-XO with pixel size -15 x 15 μm, number of pixels - 2048 x 2048, imaging area – 30.7 x 30.7 mm. The x-ray CCD SOPHIA®-XO was placed outside of the vacuum chamber of the Sparky III-HXRS source (Figure 30). The CCD was equipped with double 6-μm-thick Mylar filters (aluminized on both sides with 0.15-μm-thick Al layers) to protect the CCD from unwanted outside light. The aluminized Mylar filters were built into a custom-made vacuum flange, fitted to the front of the SOPHIA®-XO camera. This flange was fitted with a gas leak valve on either side. To ensure the lowest possible noise on the CCD chip, the internal CCD must be cooled to an extremely low temperature, which is usually performed in vacuum. However, as the SOPHIA®-XO had to placed outside the vacuum chamber, a different method had to be performed, as cooling the CCD at atmosphere could cause damage.

Therefore, the flange was constructed such that the aluminized Mylar filter would hold vacuum, and a low-pressure flow of dry nitrogen would be pumped into the camera CCD housing from one side of the flange, and a low leak valve was opened on the other end of the flange for gasses to be pumped out of the camera housing. Prior to experiments, dry nitrogen was pumped into the camera housing for 15-20 minutes, to ensure that atmospheric gasses were evacuated from the housing, and the primary gas inside the chamber was nitrogen, which does not damage to the CCD at low temperatures.

## 5.3 Characterization of the Sparky-HXRS Device and Radiation Measurements

### 5.3.1 Dependence of x-ray output and x-ray pulse width on laser energy.

The Sparky-HXRS generator (in FC mode) was systematically tested with planar Al, Ti, and Cu slabs as cathodes, and a W point-tip anode. The best x-ray yield results (in the >8.2 keV and >15 keV spectral band regions), and maximum stability of x-ray emission were obtained with a combination of planar Al slab as a cathode and a conical W point-tip anode (Figure 31). It was found that, for the W anode and Al cathode combination, the full energy of the laser (300-320 mJ) created a plasma too dense to facilitate the micropinching process, and inhibited the electron beam making contact with and producing plasma at the tip of the anode, which led to a significant decrease in the expected x-ray output. For this reason, optical filters were used to decrease the energy of the laser beam: a 1/3 energy filter (which reduced the beam to ~80 mJ), a 1/6 energy filter (~50 mJ), a 1/9 energy filter (~33 mJ), and a 1/20 energy filter (~15 mJ).

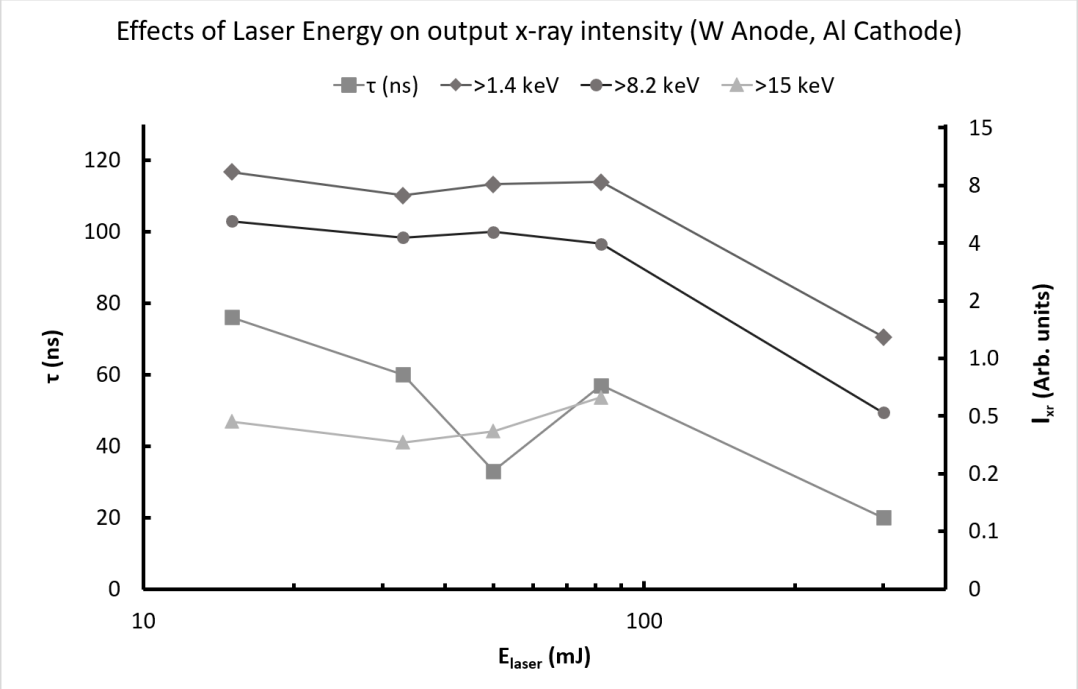


Figure 31: Parameters of the Sparky-HXRS generator operated in FC mode. The x-ray yield in spectral regions >8.2 keV (grey circles), >15 keV (black triangles), and X-ray pulse duration (light grey squares) FWHM on the main peak (the left axis τ in ns) as related to the discharge ignition versus the laser pulse energy (in mJ) at V = 27 kV and d = 8 mm (W - anode, Al - cathode).

The highest output of energy in the >8.2 keV spectral band was found to be in the lower energy regime of the laser, when the laser energy was below 100 mJ. However, in the 80-100 mJ laser energy range, the micropinch was found to produce a large number of >15 keV photons, which was not ideal to out desired x-ray region of study, and meant that the >8.2 keV signal was being increased by the >15 keV photons. The lower laser energies studied were also found to produce >8.2 keV photons efficiently, and the >15 keV photon production decreased with the laser energy. The lowest laser energy tested (15 mJ) was found to produce the best ratio of >8.2 keV photons to >15 keV photons, however the x-ray signals were very messy, often featuring multiple x-ray bursts stretched out over a longer emitting duration (~80 ns). Ultimately, shots done at a laser energy of ~15 mJ proved

to be somewhat unpredictable, and not as repeatable as is necessary for the experiment. Shots performed with the laser energy of ~33 mJ shared the same issues as the ~15 mJ shots, low predictability, but less >8.2 keV x-ray production. Ultimately, ~50 mJ proved to be the ideal energy laser energy, producing a relatively high number of >8.2 keV photons, a short x-ray pulse duration, and high repeatability and predictability in the shots (see Section 5.3.3.2 and Figure 40 for a discussion of example of these x-ray signals).

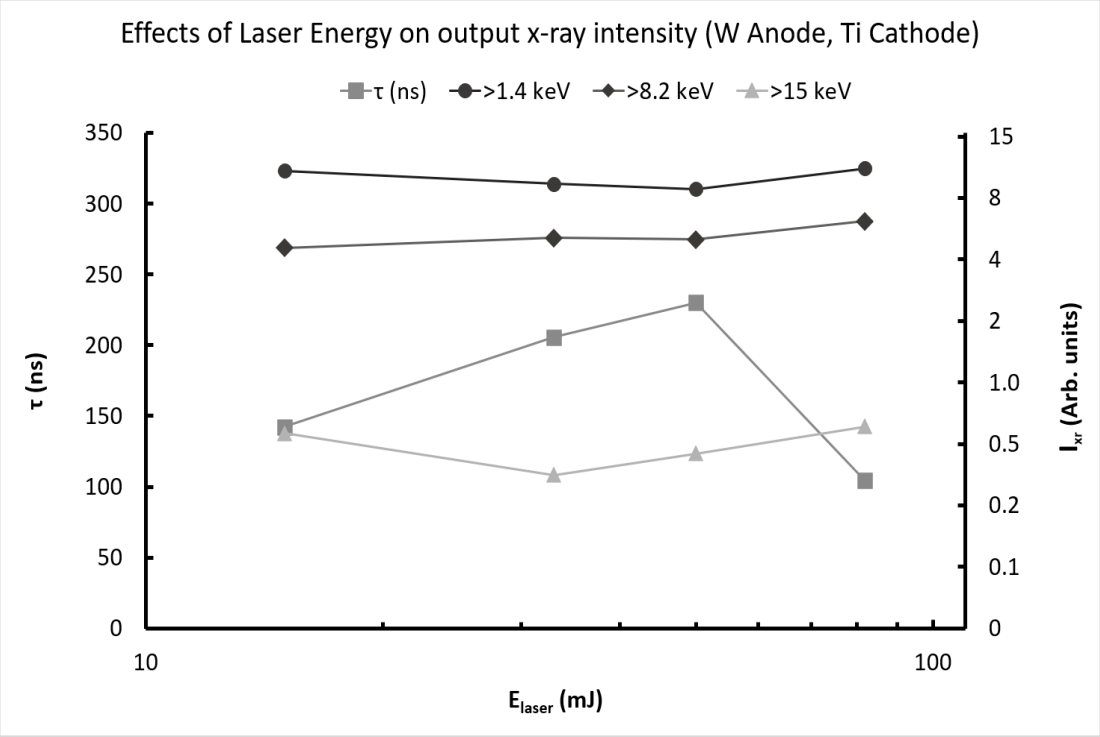


Figure 32: Parameters of the Sparky-HXRS generator operated in FC mode. The x-ray yield in spectral regions >1.4 keV, >8.2 keV, and >15 keV, and X-ray pulse duration FWHM on the main peak (the left axis τ in ns) as related to the discharge ignition versus the laser pulse energy (in mJ) at V = 27 kV and d = 8 mm (W - anode, Ti - cathode).

The effects of the laser energy were also tested on two other cathode materials, Ti and Cu. For the Ti cathode (see Figure 32), the full laser energy of 300-320 mJ didn't

produce enough x-ray emission to see a reliable and repeatable signal, so the data presented is only from a laser energy of 15-85 mJ. Interestingly, the laser energy in this range didn't seem to have a large effect on the x-ray production in the various bands measured (>1.4 keV, >8.2 keV, and >15 keV), but the x-ray pulse duration was affected. A laser energy of ~50 mJ produced the longest x-ray pulse FWHM, around 240 ns on average, while the highest energy tested (~80 ns) produced the shortest x-ray burst FWHM of about 100 ns on average. It should be noted that the Ti cathode produced the longest x-ray pulses (on the order of 150 to 250 ns) of any of the three cathode materials tested with the W anode in FC mode.

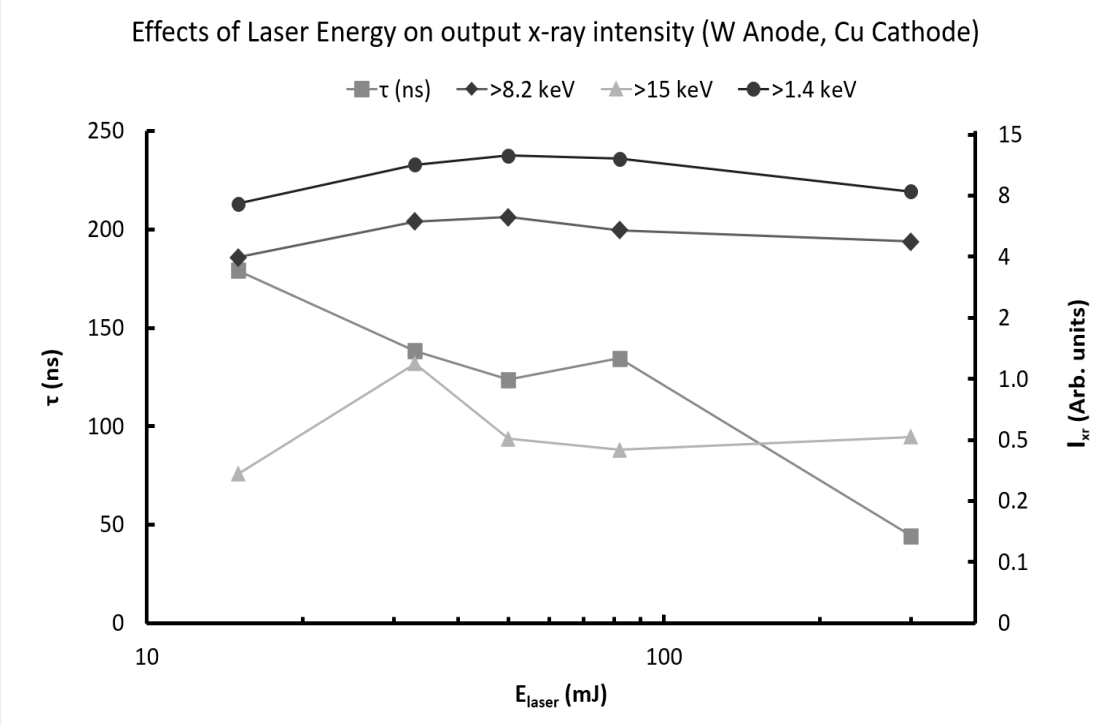


Figure 33: Parameters of the Sparky-HXRS generator operated in FC mode. The x-ray yield in spectral regions >1.4 keV, >8.2 keV, and >15 keV, and X-ray pulse duration FWHM on the main peak (the left axis τ in ns) as related to the discharge ignition versus the laser pulse energy (in mJ) at V = 27 kV and d = 8 mm (W - anode, Cu - cathode).

The Cu cathode and W anode produced the most interesting relationship with the laser energy (see Figure 33), as the full laser energy (300-320 mJ) was still able to produce a significant x-ray burst. Overall, the >1.4 keV and >8.2 keV x-ray production was minimally affected by the laser energy, but did produce the highest number of photons in those bands in the mid-laser energy ranges (33-80 mJ); however, the >15 keV x-ray production seemed to spike (almost doubling the average) at the ~33 mJ of laser energy. As to be expected, the x-ray emission FWHM time was heavily dependent upon the laser energy. As can be seen in Figure 33, the x-ray emission time, for the most part, was inversely related to the laser energy, decreasing as the laser energy increased (with the exception of the small increase at ~80 mJ). While not explicitly shown in these figures, there was also a relation between the laser energy and the time in which the x-ray pulse occurred. This effect will be discussed further in Section 5.3.3, when discussing the x-ray signals. In general, the higher laser energy resulted in the x-ray burst occurring sooner in time (from the time the laser energy is fired). With the full laser energy (300-320 mJ) in FC mode, the x-ray burst could occur as early as 100-150 ns after the laser pulse was fired (see Figure 35). At lower energies, the time of the x-ray burst could occur anywhere from 500-1500 ns after the laser was fired, as the laser plasma plume from the cathode took longer to develop. However, the timing of this x-ray burst was also affected by the condition of the cathode. As the experiment was run, the cathode spot would deteriorate over time, becoming damaged with the number of shots performed in the same place. Typically, the deterioration of the cathode laser spot would lead to a delay in the timing of the x-ray burst, however, if numerous shots were performed in the same cathode spot, the x-ray burst would become unpredictable and less repeatable over time; displaying multiple

x-ray bursts of varying emission duration. This typically occurred after about 8-12 shots in the same cathode position, which was an indication that the cathode needed to be rotated to a new spot. Also, the highest x-ray output was typically found to occur within the first 3 shots in a new cathode location, after which the x-ray emission per shot would typically decrease for the next few shots before becoming unpredictable. For the SC mode, the maximum x-ray emission typically occurred within the first 7-8 shots in a new cathode position, but still saw the x-ray pulse become unpredictable and less repeatable after 10-12 shots in the same cathode position.

### 5.3.2 Comparison of parameters Sparky III-HXRS generator operated in FC and SC modes.

We set out to characterize the main parameters of the Sparky-HXRS machine with a W anode, and, as discussed in Section 5.3.1, the Al cathode proved to be the best material to use with the W anode to produce the highest number of photons in our spectral area of interest (>8.2 keV). The main parameters of the Sparky-HXRS machine when fitted with a W anode and Al cathode are laid out in Table 4. As this combination of anode and cathode was studied in both the FC and SC modes of the machine, this provided essential information on the differences between the two modes. Notably, the addition of the larger capacitor (SC mode) raised the total photon number produced in the >8.2 keV band by an entire order of magnitude, along with the photon production in the >15 keV band. The x-ray pulse duration also increased, from as high as 50 ns in FC mode to as high as 350 ns in SC mode. Also, to prevent damage to the machine, the maximum voltage for SC mode was capped at 23 kV, whereas the capacitors were charged up to 23 kV in FC mode.

| | First Configuration (FC) | Second Configuration (SC) |
|---|---|---|
| **An estimated total photon number in > 8.5 keV region per shot** | **up to $2x10^{11}$** | **up to $1.8x10^{12}$ *** |
| **An estimated total photon number in > 15 keV region per shot** | **up to $9.3x10^{10}$** | **up to $2.8x10^{11}$** |
| **X-ray pulse duration FWHM on the main peak** | **20-50 ns** | **80-350 ns** |
| **Size of x-ray source in > 8.5 keV region** | **1-1.5 mm** | **1.5 mm** |
| **Number of shots per hour** | **150-200** | **24** |
| **Operational voltage** | **up to 27 kV** | **up to 23 kV** |
| **Discharge current** | **up to 1.2 kA** | **up to 12 kA** |
| **Period of the current oscillations** | **0.5 µs** | **3.7 µs** |

Table 4: Main parameters of the Sparky III-HXRS generator are shown below (W – anode, Al – cathode). *This parameter is two orders of magnitude higher than the results presented in refs. [98], [99].

The number of shots that could be performed per hour was decreased in SC mode, from up to 200 shots per hour in FC mode down to 24 shots per hour. The second configuration also increased the maximum discharge current an order of magnitude, from 1.2 kA up to 12 kA, as well as increasing the period of current oscillations from 0.5 µs to 3.7 µs, due to the increase stored capacitor energy as well as in machine inductance in SC mode.

| | Second Configuration (SC) |
|---|---|
| An estimated total photon number in > 8.2 keV region per shot | up to $1.8 \times 10^{12}$ |
| An estimated total photon number in > 15 keV region per shot | up to $8.8 \times 10^{10*}$ |
| X-ray pulse duration FWHM on the main peak | 80-200 ns |
| Size of x-ray source in > 8.2 keV region | 1.5 mm |
| Number of shots per hour | 24 |
| Operational voltage | up to 23 kV |
| Discharge current | up to 12 kA |
| Period of the current oscillations | 3.7 µs |

Table 5: Main parameters of the Sparky III-HXRS generator when operated in SC (SS304 – anode, Al – cathode). It should be noted that the number of >15 keV photons is likely an overestimation of the average amount produced per shot, as the >15 keV signal was only integrable in <5% of the shots. Meaning that, on average, the shots with SS304 anode did not produce enough >15 keV photons to register a signal, and this number is based on the small percentage of shots that produced the highest yield of >15 keV photons.

As the SS304 anode was heavily studied for the TISpP, the parameters of the Sparky-HXRS machine with a SS304 anode and Al cathode were also analyzed in SC mode. Many of the parameters remained the same, including the estimated number of >8.2 keV photons produced. However, the duration of x-ray emission on the main peak ranged from 80-200 ns; a shorter maximum duration than was observed with the W anode. Interestingly, the SS304 anode was found to produce little >15 keV x-ray emission.

### 5.3.3 Study of spectral characteristics of the Sparky III-HXRS source.

#### *5.3.3.1 Combination of the brass anode and Cu cathode.*

The first tests with Sparky-HXRS began with a brass anode and Cu cathode, operated in FC mode at 300-320 mJ of laser energy. A spectrometer was implemented to measure the $K_\alpha$ and $K_\beta$ lines from Cu, and the $K_\alpha$ lines from Zn. Figure 34 displays an example measurement of the brass hard x-ray spectrum of K-shell Cu and Zn produced at the Sparky-HXRS in 159 shots. Being an alloy of both Cu and Zn, brass was an ideal choice to first study on the Sparky-HXRS machine, as brass pulsed power plasmas have been studied extensively on the UNR Zebra machine [63]. While we were able to obtain characteristic spectral lines from both Cu and Zn, it was unclear whether the majority of Cu spectral lines were from the anode material (brass) or the cathode material (Cu). For this reason, all later experiments were performed with an anode and ca`thode composed of entirely different elements.

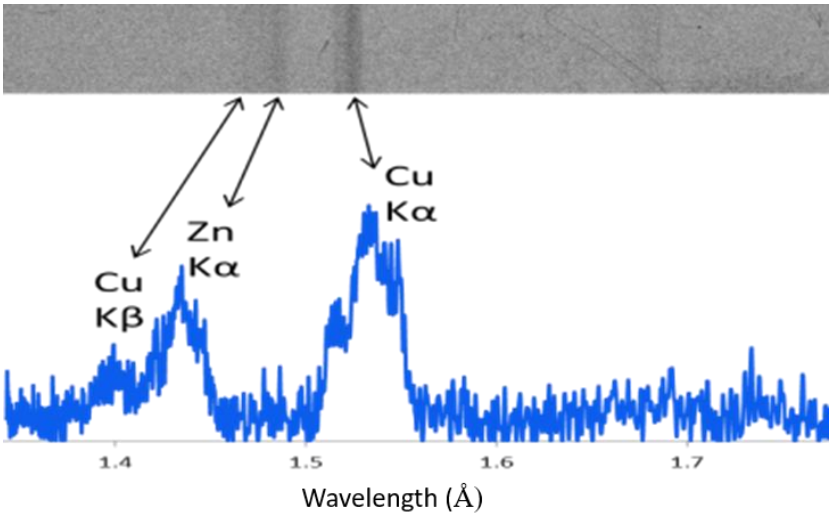


Figure 34: The Sparky-HXRS generator operated in mode FC. Hard x-ray characteristic K-shell Cu and Zn lines (anode – brass, cathode – Cu). Anode voltage – 23 kV, number of shots – 159.

The x-ray signals measured using the SiDs and PCD are shown in Figure 35. Three SiDs were used, filtered at >1.4 keV, >8.2 keV, and >9 keV. The >8.2 keV filter for the SiD and PCD was chosen to study the characteristic $K_\alpha$ and $K_\beta$ lines from Cu (which range from 8.05 to 8.9 keV) and the Zn $K_\alpha$ lines (~8.6 keV), while the >9 keV filter was selected to study the production of Zn $K_\beta$ as well as bremsstrahlung radiation. The SiD filtered at >1.4 keV also detected a significant x-ray emission trace. In general, the emission duration lasted roughly 40 ns, and occurred relatively early in time, about 135 ns after the laser pulse was fired, as the full laser energy was used for the brass anode and Cu cathode combination.

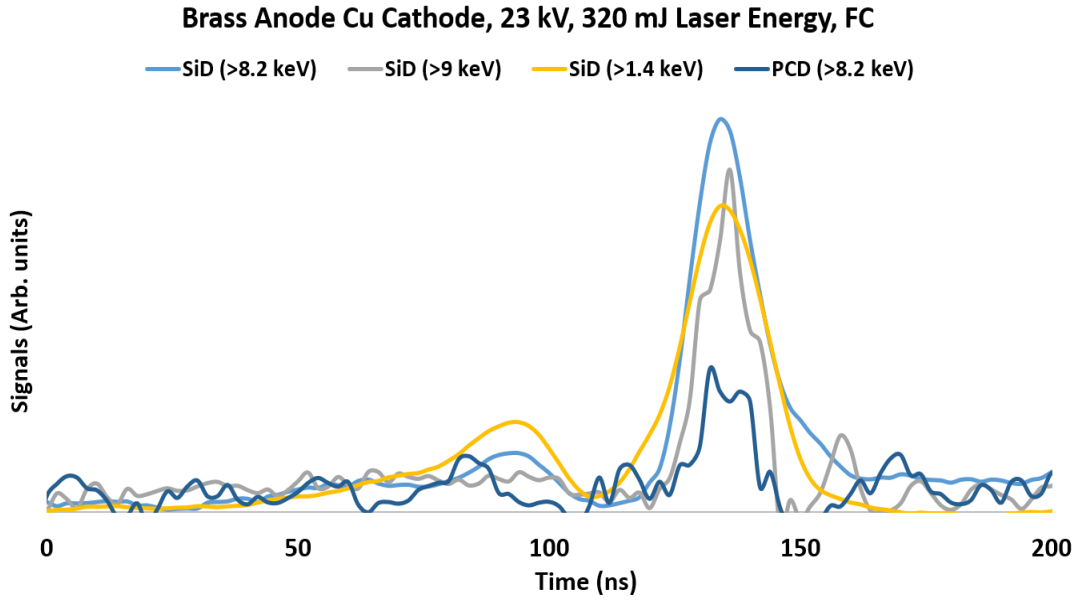


Figure 35: Signals from a Brass Anode and Copper Cathode in FC mode.

### *5.3.3.2 Combination of W anode and Al cathode.*

The most extensively studied combination of anode and cathode material was W and Al, respectively. In combination with the W anode, both the Al and Ti cathodes

produced high yields of x-ray photons in the >8.2 keV spectral bands, and relatively low >15 keV x-ray photons, with relatively good repeatability. Ultimately, Al was chosen as the primary cathode material for experiments with the W anode for two primary reasons: 1) it produced a slightly higher ratio of >8.2 keV x-ray photons to >15 keV x-ray photons; and 2) the characteristic spectra produced from Al (all of which being >7.9 Å) would not appear on the spectrographs, which measured between 1 and 3.9 Å.

A.

| Line | Levels | Transitions | Energy (eV) | λ (Å) | Intensity |
|---|---|---|---|---|---|
| $L\alpha_2$ | $L_3M_4$ | $2p_{3/2} - 3d_{3/2}$ | 8335.3 | 1.487 | 11.22 |
| $L\alpha_1$ | $L_3M_5$ | $2p_{3/2} - 3d_{5/2}$ | 8398.2 | 1.476 | 100 |
| $L\beta_4$ | $L_1M_2$ | $2s_{1/2} - 3p_{1/2}$ | 9525.2 | 1.302 | 3.56 |
| $L\beta_1$ | $L_2M_4$ | $2p_{1/2} - 3d_{3/2}$ | 9672.6 | 1.282 | 55.6 |
| $L\beta_3$ | $L_1M_3$ | $2s_{1/2} - 3p_{3/2}$ | 9818.9 | 1.263 | 5.05 |
| $L\beta_2$ | $L_3N_5$ | $2p_{3/2} - 4d_{5/2}$ | 9964.1 | 1.244 | 22.72 |
| $L\gamma_1$ | $L_2N_4$ | $2p_{1/2} - 4d_{3/2}$ | 11,286.0 | 1.098 | 10.45 |

B.

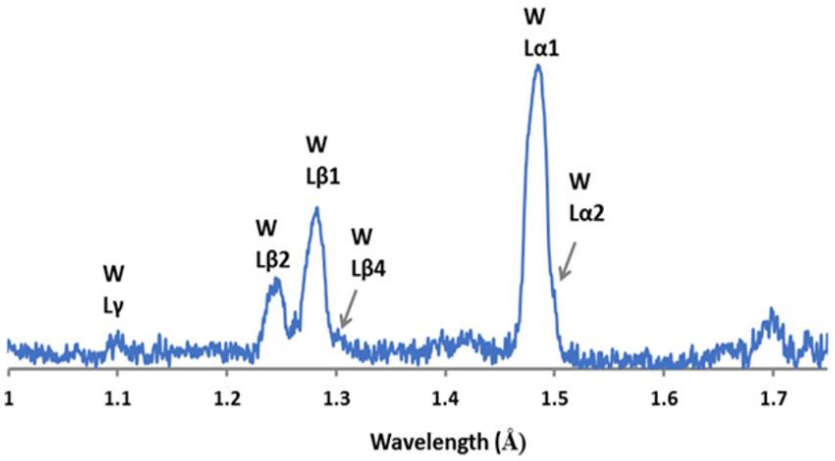


Figure 36: Hard x-ray characteristic L-shell W lines. A) Modified table of atomic data for the most intense transitions from ref. [108]; B) The experimental spectrum produced at the Sparky-HXRS (operated in mode FC) at the voltage of 27 kV in 350 shots.

Figure 36 displays an example of the hard x-ray spectrum of L-shell W produced on the Sparky-HXRS machine over 350 shots in FC mode. The most intense hard x-ray characteristic W L-shell lines occupy the energy range from 8 to 12 keV (in a spectral range between 1.5 and 1.1 Å) and represent the transitions from L-shell ($L\alpha_1$, $L\alpha_2$, $L\beta_1$, $L\beta_3$, and $L\beta_4$). The line identification, energies, wavelengths, and relative intensities of the strongest W L-shell lines are shown in Figure 36A (modified Table 1 from Seely *et al* [108]) as well as a typical L-shell W spectrum produced at the Sparky-HXRS generator in Figure 36B. It is a well-established fact that ionization of atoms (ions) by charged particles and photons leads to the alignment of target inner-shell vacancy with the total angular momentum J > ½. X-rays or Auger electrons emitted in the subsequent de-excitation demonstrates this alignment through the polarization of x-rays or through their anisotropic angular emission. As such, it is important to study the polarization properties of the lines $L\alpha_1$, $L\alpha_2$, and $L\beta_2$ of W, and compare them with the unpolarized lines such as $L\beta_1$, $L\beta_3$, and $L\beta_4$.

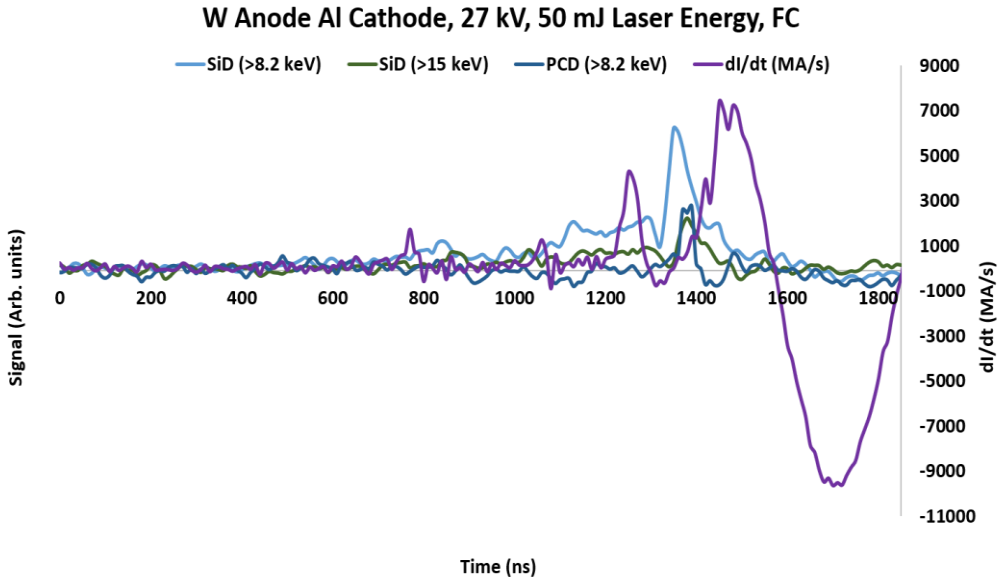


Figure 37: Signals from W Anode and Al Cathode in FC mode.

The x-ray signals for a W anode and Al cathode shot in FC mode with the anode voltage charged to 27 kV and a laser energy of ~50 mJ, are shown in Figure 37. The current shows a significant dip around 1400 ns, corresponding to the moment of the micropinch and primary x-ray emission. The emission duration lasted approximately 80 ns at FWHM, and signals were detected in both the >8.2 keV spectral band by both the SiD and PCD, as well as in the >15 keV band by another SiD.

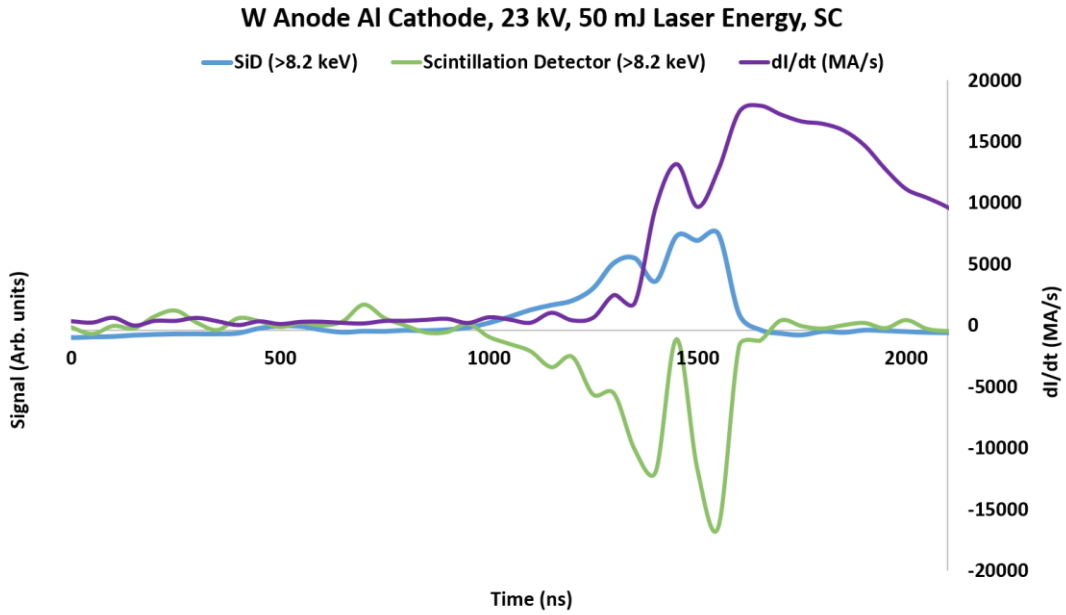


Figure 38: Signals from W Anode and Al Cathode in SC mode.

In comparison, Figure 38 shows the same anode and cathode combination (W and Al, respectively) and laser energy (~50 mJ) performed on the Sparky-HXRS machine in SC mode, and charged to 23 kV. The differences can immediately be seen, as the x-ray emission process lasted much longer and the current reached a much higher peak. For shots in the SC mode with a W anode, a Scintillation Detector was implemented to see the

distance at which x-rays could be detected outside of the chamber. The Scintilation Detector was placed at various distances from the special Kapton window (see Figure 29 and Figure 30) to ensure that a diagnostically significant amount of x-rays would still reach outside the chamber, and extend far enough to be detected by the films implemented in the TISpP.

Once again, we see a significant x-ray emission, as well as a pre-pulse emission prior to the main pulse which is initiated by the laser plasma, prior to the micropinch. The >8.2 keV emission began around 1000 ns as detected by both the SiD and Scintillation Detector, with the main x-ray pulse occurring around 1500 ns.

Ultimately, the SC of the Sparky-HXRS machine was shown to increase the current peak, significantly increase the x-ray output from the micropinch, and increase the emission duration of the x-ray signals.

#### *5.3.3.3 Combination of Titanium (Ti) anode and Tungsten (W) cathode.*

The combination of a Ti anode and W cathode was also tested in FC mode. Having initially done testing with the W anode and Ti cathode combination, it was decided that the reverse should be tested as well, with the anode being made up of Ti and the cathode of W. This was done in an effort to see how much of the x-rays detected were from the cathode material, as the Ti characteristic lines would radiate in the lower x-ray region (between 4 and 5 keV). Figure 39 is an example of the characteristic radiation from Ti obtained on the Sparky-HXRS generator in FC mode, taken over 320 shots. Both Ti $K_\alpha$ and $K_\beta$ lines were extremely prominent, and reliably produced on the machine. W characteristic lines were not detectable on the film, indicating that the primary source of radiation was the anode material.

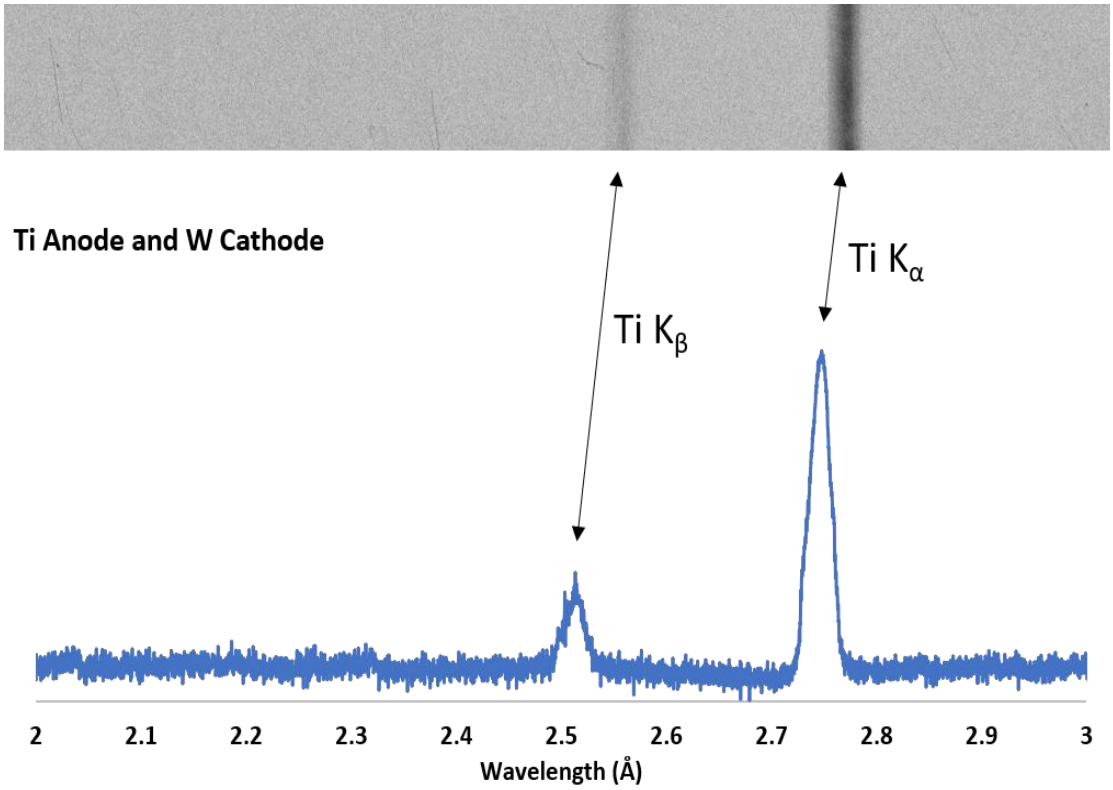


Figure 39: Characteristic spectra of K-shell Ti from Ti anode and W cathode operated in SC mode: $K_\alpha$ (2.748 Å) & Ti $K_\beta$ (2.514 Å) lines are present, taken over 320 shots. No discernable W lines were visible on the spectrograph, indicating the primary source of radiation was the anode material.

The x-ray signals from an example Ti anode and W cathode shot in FC mode are shown in Figure 40. Similar to the W anode shot discussed in Section 5.3.3.2., both the >8.2 keV filtered SiD and PCD as well as the >15 keV filtered SiD detected x-ray traces, however, they were far less intense than what was detected with the W anode. A >1.4 keV filtered SiD was placed in the chamber to detect the characteristic $K_\alpha$ and $K_\beta$ radiation from the Ti anode, which, as expected, proved to be a very prominent signal. The emission duration lasted approximately 90 ns at FWHM for the main pulse.

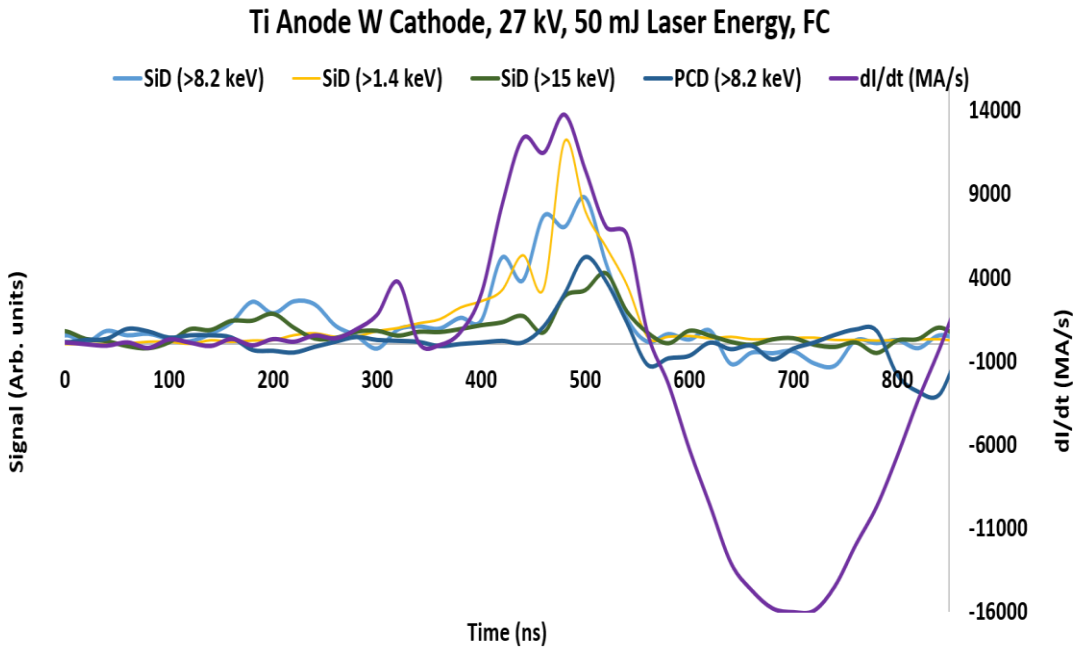


Figure 40: Signals from Ti Anode and W Cathode in FC mode.

#### *5.3.3.4 Combination of SS304 anode and Al cathode.*

The final anode material tested was SS304 (stainless steel) in combination with an Al cathode in SC mode, as the Fe in the SS304 could produce Fe $K_\alpha$ and $K_\beta$ lines to be studied with the topaz crystals used in the TISpP (see Section 5.4). SS304 proved to be an excellent producer of x-rays in the >1.4 keV and >8.2 keV spectral bands. The example x-ray signals and current trace shown in Figure 41 was one of the most powerful x-ray emitting shots we obtained with the Ti anode. The emission was similar to that seen in the W anode, featuring a prominent pre-pulse at 1000 ns, prior to the main pulse at 1250 ns, with an emission time on the main pulse of about 150 ns at FWHM.

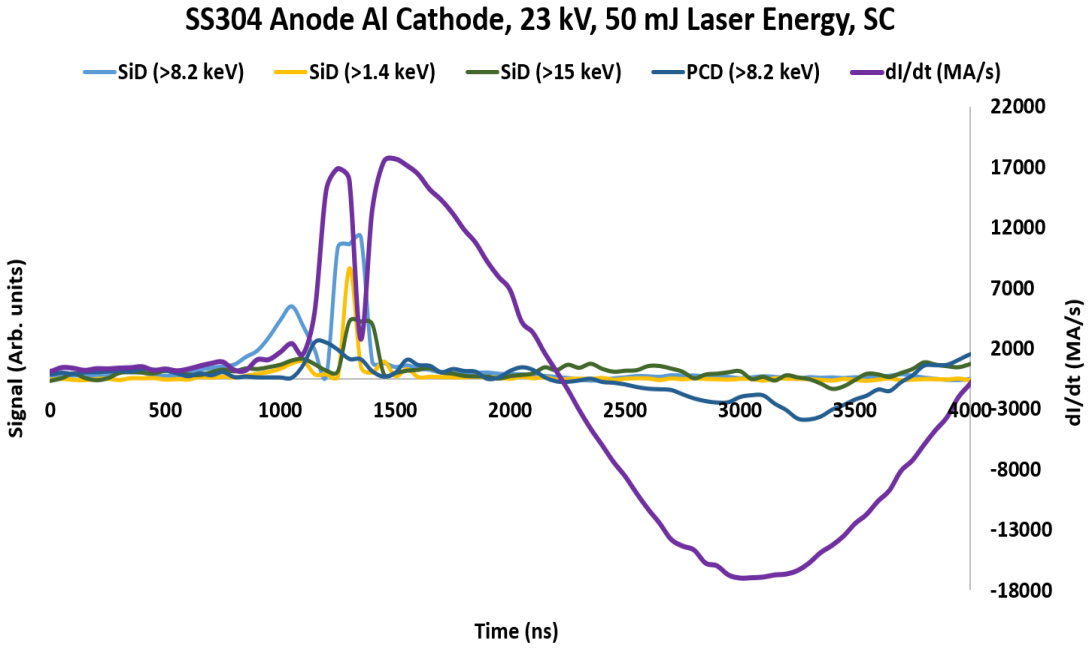


Figure 41: Signals from SS304 Anode and Al Cathode in SC mode.

## 5.4 Testing of the novel TISpP at the Sparky HXRS generator.

For the initial tests on the new TISpP, characteristic spectra of K-shell Fe from a SS304 anode was utilized. In the TISpP, two flat topaz crystals (303) with 2d = 2.712 Å were used. The Sparky III-HXRS generator was operated in SC mode, with anode voltage V = 23 kV. To maximize the potential spectra obtained, the crystals were turned in such a manner as to center the desired spectral lines on the spectrograph detector (films or x-ray CCD camera).

The arrangements of the crystals are selected to isolate a single-linear component of the radiation intensity. The spectra of $K_{\alpha 1}$ (1.936 Å) and $K_{\alpha 2}$ (1.94 Å), and Fe $K_{\beta}$ (1.757

Å) (for $I_{\perp}$ component and $I_{II}$ component) were recorded onto Kodak Biomax MS x-ray film during 80-84 shots on the table-top Sparky-HXRS generator. Examples of the Fe $K_{\alpha}$ and $K_{\beta}$ lines obtained are shown in Figure 42. The $K_{\alpha}$ line was measured over 84 shots. Spectral lines were obtained in both the ∥ and ⊥ components. The $K_{\beta}$ lines were obtained over 80 shots, and the spectra were much less prominent. The TISpP with the film cassettes proved to be a reliable and efficient way of obtaining spectral lines in both polarization directions, however, due to the large number of shots needed to obtain the spectra, this presents calibration difficulties. Also, the magnitude differences between the two components shown in Figure 42 are not necessarily a measure of the polarization, but the current lack of calibration in the TISpP. The establishing experiments discussed and presented in this work represent the development of the Sparky-HXRS machine and TISpP. Future work with the Sparky-HXRS machine will focus on the calibration and analysis of results obtained on the TISpP.

**A.**

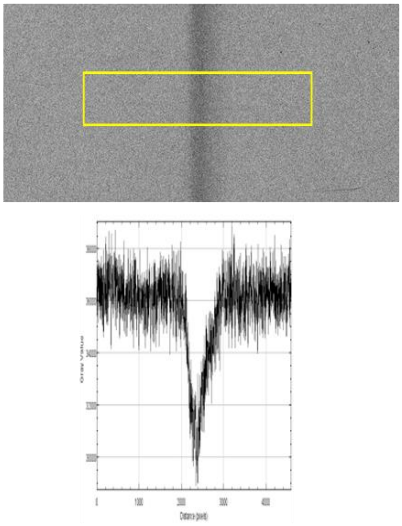

Spectrum of Fe $K\alpha_1$ (1.936 Å) and Fe $K\alpha_2$ (1.94 Å). Topaz crystal #1 ($I_\perp$ component).

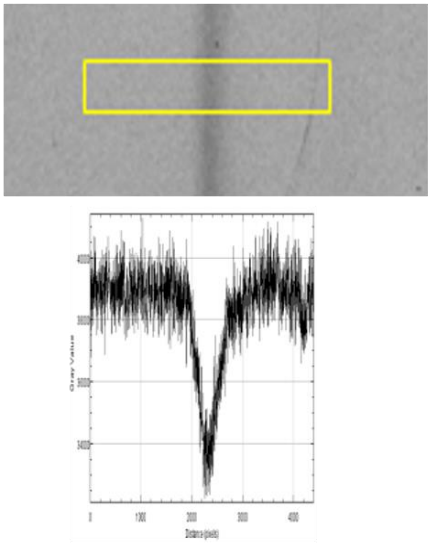

Spectrum of Fe $K\alpha_1$ (1.936 Å) and Fe $K\alpha_2$ (1.94 Å). Topaz crystal #2 ($I_\parallel$ component).

**B.**

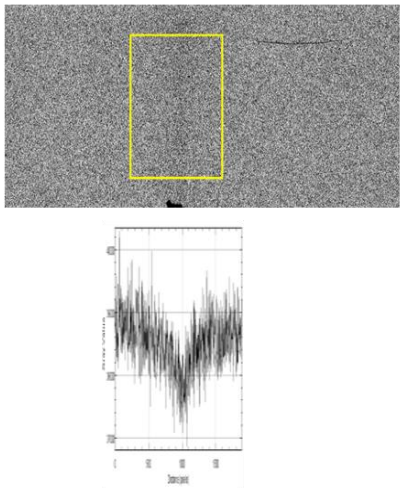

Spectrum of Fe $K_\beta$ (1.757 Å). Topaz crystal #1 ($I_\perp$ component).

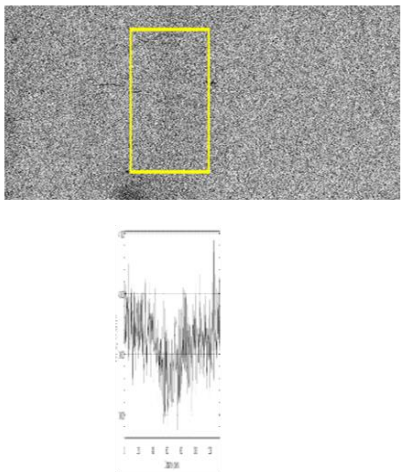

Spectrum of Fe $K_\beta$ (1.757 Å). Topaz crystal #2 ($I_\parallel$ component).

Figure 42: A. Characteristic spectrum of Fe $K\alpha_1$ (1.936 Å) and Fe $K\alpha_2$ (1.94 Å) lines from SS304 anode of obtained in N=82 shots of the Sparky-HXRS generator. B. Characteristic spectrum of Fe $K_\beta$ (1.757 Å) line from SS304 anode obtained in N=84 shots of the Sparky-HXRS generator. Optical density of film is in arbitrary units.

Later experiments were performed with the SOPHIA®-XO Intensified X-ray CCD camera, however, due to the physical limitations of the TISpP and Sparky-HXRS machine, only the parallel (∥) component was capable of being measured (see Figure 30). Future work will be done to modify the TISpP to allow for the ⊥ component to be measured from above instead of below (rotating the crystal #1 holding structure by 180°) to allow for the SOPHIA®-XO camera to be oriented from above, looking down, to measure the ⊥ component. However, for the experiments performed with the SOPHIA®-XO in place to measure the ∥ component, both Fe $K_\alpha$ and $K_\beta$ lines were successfully obtained in single shots (see Figure 43). The SOPHIA®-XO camera drastically reduced the number of shots necessary to obtain spectral lines on the TISpP from >80 shots, to a single shot per line.

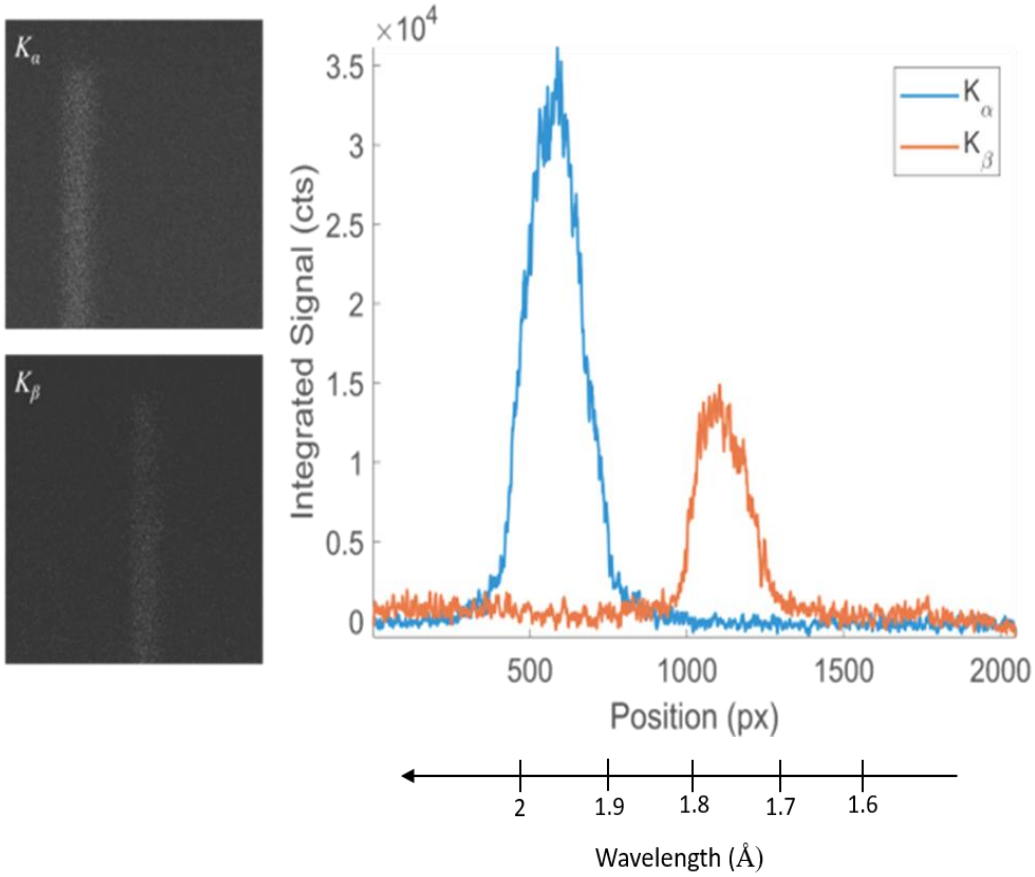


Figure 43: Combined characteristic spectra of K-shell Fe from SS304 anode: $K_{\alpha 1}$ (1.936 Å) & Fe $K_{\alpha 2}$ (1.94 Å) - $I_{\parallel}$ component, and Fe $K_{\beta}$ (1.757 Å) - $I_{\parallel}$ component. Both spectral lines were obtained in different single shots of the Sparky-HXRS generator (operated in SC mode).

## 5.5 Conclusions and Discussion

A table-top hard x-ray source with a laser triggered micropinch, dubbed Sparky Hard X-ray Source (or Sparky-HXRS), was developed and characterized with a multitude of anode and cathode materials at the University of Nevada, Reno. The machine was developed in two different modes: FC mode, which implemented a 12 nF capacitor bank charged to a maximum voltage of 27 kV; and SC mode, which implemented a 0.6 μF capacitor charged to a maximum voltage of 23 kV.

Characteristic K- and L-shell x-rays were obtained from many different materials: Cu $K_\alpha$ and $K_\beta$ lines and Zn $K_\alpha$ lines were obtained from a brass anode; a range of W L-shell lines, including $L_\alpha$, $L_\beta$, and $L_\lambda$ were measured from a W anode; Ti $K_\alpha$ and $K_\beta$ lines were measured from a Ti anode; and Fe $K_\alpha$ and $K_\beta$ lines were measured using the TISpP and a SS304 anode. Experiments found that the energy of the laser pulse had a drastic effect on the micropinch and x-ray emission. The highest laser energy tested (300-320 mJ) was found to produce a very low emission micropinch and an earlier emission time (often producing no measurable x-ray emission at all), while the lower laser energies (<100 mJ) were found to produce higher x-ray emission from the micropinches. The optimal laser energy for our primary configuration of study (a W anode and Al cathode) proved to be ~50 mJ, which was found to produce the highest number >8.2 keV photons and the most stable and repeatable x-ray emission. In the machine's optimal configuration, the average number of >8.2 keV photons produced per shot was on the order of $10^{12}$.

In conjunction with the Sparky-HXRS machine, a side-on time-integrated x-ray polarimeter (TISpP) with two flat topaz crystals was developed to study the polarization of the hard x-ray characteristic lines produced from a SS304 anode. The Sparky-HXRS machine and TISpP was designed such that future experiments could implement different crystals to study characteristic lines from other materials (such as Cu and W, which produce cold characteristic lines that can be difficult to study in higher energy pulsed power plasmas). When fitted with the SOPHIA®-XO x-ray CCD camera, the TISpP was able to record characteristic W L-shell spectral lines from a single shot on the Sparky-HXRS machine.

Ultimately, the Sparky-HXRS machine was capable of reliably producing characteristic x-ray lines from a number of different elements. Although built with the intention of studying the polarization of characteristic W L-shell spectral lines, the modular design of the Sparky-HXRS is capable of studying a large range of characteristic spectra from a multitude of elements. By varying the anode material, cathode material, laser energy, laser focusing spot size, capacitance, and anode voltage, the Sparky-HXRS machine is capable of producing characteristic x-rays with relatively low bremsstrahlung for the study of many characteristic lines that are otherwise difficult to study in pulsed power pinches on machines of higher energy.

# 6 Conclusions and Future Plans

This dissertation described and presented the results gathered from multiple experimental campaigns on various pulsed power machines of differing architecture and current level. Experiments were performed on the high-impedance UNR Zebra Marx bank generator and the low-impedance UM MAIZE LTD and the results were compared between the two machines. The new tabletop Sparky hard x-ray source (Sparky-HXRS) was developed and tested at UNR.

Chapter 2 discussed the essential physics behind a traditional Z-pinch. As the high current begins to flow through the current carrying wire load, the material begins to ablate, causing the material to become very hot and ionize. Simultaneously, magnetic fields generated by the current and the Lorentz forces exerted on the moving charged in the magnetic field begin to push the ablated material towards the geometric center of the load, causing the material to "pinch," creating a very hot dense plasma column. The four stages of a Z-pinch were discussed (current initiation, ablation, implosion, and stagnation), as well as other physical phenomena, such as the precursor column. Also, various types of current carrying load were discussed, the most important for this work being the double planar wire array (DPWA) and double planar foil liner (DPFL).

Chapter 3 gave an overview of the many diagnostics used in the experiments presented. Both experimental and theoretical/modelling diagnostics were discussed. Amongst the some of the most important experimental diagnostics presented were the x-ray diodes, the absolutely calibrated PCD, and the x-ray spectrometers (both standard and the spectropolarimeter built for Sparky-HXRS). The theoretical models discussed were all

of incredible importance for interpreting the experimental data obtained. The S-UNR code was used to interpret the spectrographs obtained during the experiments to calculate the plasma parameters (electron temperature and density) of the plasmas. The MAIZE LTD inductance model used the current trace measurement to estimate the time dependent inductance of the load throughout the pinch, with relative maximas indicating moments of minimum effective current carrying radii of the pinching plasma. The PCD signal was integrated in various multiple spectral regions (>1 keV on Zebra, >2.4 keV on MAIZE, and >8.2 keV on Sparky-HXRS) to estimate the total output energy and/or photon number.

Chapter 4 presented results of experiments on Zebra and MAIZE with DPWA and DPFL load implosions. Experimental data from the UM MAIZE LTD with low-atomic-number Al DPWAs and DPFLs, mid-atomic-number brass DPWAs of varying aspect ratio, and high-atomic-number W DPWAs was presented. These experiments on the MAIZE LTD presented the first successful implosions of both W DPWAs and Al DPFLs on a low-impedance LTD machine. Through spectroscopic analysis, the plasmas created on the MAIZE LTD proved to be cooler in temperature, but on a similar order of density ($10^{19}$ $cm^{-3}$) as similar loads imploded on the Zebra generator, despite being a much lower energy machine (7.9 kJ for MAIZE vs 150 kJ for Zebra). In addition, the Al DPFL revealed an optically thin plasma near the anode, which is a rarity amongst Al pulsed power plasmas. The overall energy output in the >2.4 keV spectral band was measured using the PCD and showed the total x-ray output to be related to the atomic number of the material, with the low-atomic-number Al radiating the least (67 mJ), mid-atomic-number brass radiating the second most (0.53 J and 0.77 J), and the high-atomic-number W being the highest radiator (1.6 J) on the MAIZE machine. Another interesting find was that the Al DPFL, despite

being mass unoptimized for the MAIZE machine and very difficult for the low-energy machine to implode, was still able to produce nearly half the overall energy of the mass optimized Al DPWA. The Al DPFL also displayed different radiative behavior than the DPWAs, with the bulk of x-ray radiation beginning soon after the start of current and continuing to radiate with many small bursts as more mass continued to stream towards the center. This implies that, perhaps, with a more optimized DPFL load (using a thinner, lighter foil) could even outperform the DPWAs, lending credibility and warranting more testing of the theory that foil liners could replace wire arrays load types to the effect of greater x-ray production throughout the pinch. Lastly, the inductance model, first developed by Steiner 2016 [42] and later revised in Butcher 2021 [64], showed good correlation in both timing and magnitude with the x-ray bursts, reaching relative maximas concurrently with x-ray bursts. Between the inductance modelling and the x-ray signals recorded on the PDC and Si-diodes, it can be concluded that the precursor column formation has a significant effect on the current trace, as it seems to draw an impactful amount of current away from the ablating wire planes and prolonging the implosion time of the double planar loads. Further experimentation is needed, but this effect could be mitigated by varying the aspect ratios of the double planar loads, which could lead to stronger and more effective pinching on the MAIZE LTD, and more overall x-ray production. Lastly, and one of the most significant findings, is that, although not necessarily identical implosions, the DPWA implosions on both Zebra and MAIZE demonstrated similar physical processes, despite being performed on machines of varying architecture, peak current, stored energy, and impedance, which implies that these novel load types could be scaled up for use on larger scale pulsed power devices with relatively

predictable outcomes and should be considered good candidates for experiments on such machines. The collaborative experiments between UNR and UM on the MAIZE LTD mark some of the first experiments with DPWAs and DPFLs on university-scale LTD machines, and there is still much to be learned. Continued experimentation with DPWAs and DPFLs on the MAIZE LTD are still needed to fully understand the optimization of load parameters for optimized x-ray output. The x-ray output of the heavier DPFLs shows they could produce more x-ray output than DPWAs with similar parameters on higher energy machines that could more efficiently implode the load.

Chapter 5 discussed the development of the new tabletop Sparky-HXRS machine at UNR, and presented data from experiments performed with it. Characteristic x-ray spectra were obtained from all anode materials tested: K-shell Cu and Zn was obtained from a brass anode; K-shell Ti from a Ti anode; K-shell Fe from a SS304 anode; and L-shell W from a W anode. The machine was operated in two modes: first configuration (FC) which used a bank of six 12 nF capacitors connected in parallel and was charged to a maximum voltage of 27 kV, and second configuration (SC) which used a single 0.6 nF capacitor charged to a maximum of 23 kV. Spectra were obtained in both modes, and the larger capacitor used in SC mode was found to improve the overall >8.2 keV x-ray photon production an order of magnitude from FC mode (up to $10^{12}$ in SC mode, up from $10^{11}$ in FC mode). The number of shots needed to obtain resolvable spectrograms was decreased from around >300 or more in FC mode to around >60 or more, however, the repetition rate of shots decreased from 150-200 shots per hour to about 24 shots per hour. Fe K-shell radiation was measured using the new spectropolarimeter developed especially for Sparky-HXRS. Implementation of the SOPHIA®-XO high intensity x-ray CCD camera reduced

the number of shots required to obtain discernable spectral lines on the detector to a single shot (down from >60 for the Kodak Biomax film).

I have presented the results of this dissertation at numerous conferences (see Table 6). The results of Al and W DPWAs and Al DPFLs imploded on MAIZE were published in Butcher *et al*, 2021 in Physics of Plasmas [64]. The results of brass DPWAs of varying aspect ratios imploded on MAIZE has been submitted for publication in IEEE TPS [109] and also published in IEEE Xplore 2021 [28]. The development and results of measurements with the Sparky-HXRS device is being prepared for submission.

## Presentations

| Presentation Type | Title | Conference | Location | Date |
|---|---|---|---|---|
| **Invited Talk** | *Characteristic Effects of Pulsed Power Generators of Different Architecture on the Implosion Dynamics of Double Planar Wire Arrays and Double Planar Foil Liners* | ZNetUS 2022 | San Diego, CA (Virtual Conference) | Apr. 21-22, 2022 |
| **Invited Talk** | *Characteristic Effects of Pulsed Power Generators Of Different Architecture on the Implosion Dynamics of Mid-$Z_a$ Double Planar Wire Arrays* | IEEE International Conference on Plasma Science (ICOPS 2021) | Stateline, NV (Virtual Conference) | Sept. 12-16, 2021 |
| **Poster** | *Tungsten Z-pinch Behavior on 1 MA Generators of Different Architecture* | 2021 NNSA Stewardship Science Academic Program Symposium (Virtual Symposium) | Virtual Symposium | Feb. 16-18, 2021 |
| **Oral Talk** | *Al Z-pinch Behavior on 1 MA Generators of Different Architecture* | *Z* Fundamental Science Workshop | Sandia National Labs, Albuquerque, NM (Virtual Workshop) | Aug. 3-4, 2020 |
| **Oral Talk** | *Al Double Planar Z-pinch Loads on Various 1 MA Generators* | Annual FWS20 meeting of the APS | Virtual Meeting | Oct. 9-10, 2020 |

| | | | | |
|---|---|---|---|---|
| **Poster** | A study of the generation of hard X-ray characteristic lines from Pulsed Power Sources | 2020 NNSA Stewardship Science Academic Program Symposium | Washington, D.C. | Feb. 26-27, 2020 |
| **Poster** | *Time-Evolution of Z-pinch Plasma Inductance and Effective Current Carrying Radius of Low-Z Al and High-Z W Double Planar Wire Arrays and Double Planar Foil Liners, and Efficiency Comparison of W Double Planar Wire Arrays on University Scale Pulsed Power Generators* | First Z-NetUS Workshop | La Jolla, CA | Jan. 6-8, 2020 |
| **Oral Talk** | *Aluminum double planar wire arrays and double planar foil liners on the UNR and UM pulsed power drivers* | 2019 IEEE Pulsed Power and Plasma Science Conference (PPPS 2019) | Orlando, FL | June 23-28, 2019 |
| **Poster** | *Highlights of radiative properties and implosion characteristics of Al and W Double Planar Wire Arrays and Al Double Planar Foil Liners on the MAIZE LTD Generator* | 2019 NNSA Stewardship Science Academic Program Symposium | Albuquerque, NM | Feb. 19-20, 2019 |
| **Oral Talk** | Highlights *of Experiments with Al and W DPWAs on the University of Michigan's Linear Transformer Driver* | 2018 Annual Meeting of the Far West Section of APS | Fullerton, CA | Oct. 18-20, 2018 |
| **Poster** | *Implosion Dynamics and Radiative Properties of Recent Experiments with W Double Planar Wire Arrays on UM MAIZE LTD* | 45th IEEE International Conference on Plasma Science (ICOPS 2018) | Denver, CO | June 24-28, 2018 |

| | | | | |
|---|---|---|---|---|
| **Poster** | *Implosion characteristics, dynamic plasma radius, and x-ray output of W and Al double planar wire arrays on MAIZE LTD and comparison with Marx bank Zebra generator* | 2018 NNSA Stewardship Science Academic Program Symposium | Bethesda, MD | Feb. 21-22, 2018 |
| **Poster** | *Comparison of X-rays Bursts from pure and mixed Double Planar Wire Arrays at UM LTD MAIZE Generators* | 10th International Conference on Dense Z Pinches | Stateline, NV | Aug. 13-17, 2017 |
| | | | | |

Table 6: Invited Talks, Oral Talks, and Poster Presentations where the work in this dissertation was presented.

# Appendices

## Appendix A: The Basic LC Circuit Model of a Z-pinch and Role of Inductance on the Current

The simplest example of a pulsed power experiment is with the implosion of a cylindrical foil liner (the cylindrical shape allows us to use cylindrical symmetry, which simplifies the math significantly). Assuming we have a cylindrically symmetric vacuum chamber made of a metal, where the cylindrical foil load is located directly in the center of the vacuum chamber. If we apply a high-voltage difference across the electrodes of the cavity (V) we will drive a fast, high-amplitude current pulse (I(t)) through the load. This is most eloquently described in McBride *et al*. 2018 [77], which this description is based on.

First, we will assume that the metal is perfectly conducting (which is a safe assumption in most cases). Second, we will assume that all initial currents and magnetic fields are zero. With these assumptions, the only factor limiting the rise in the current is the inductance of the metal cavity, as we essentially have a voltage applied to a conductor, which can be described by the equation,

$$\frac{dI}{dt} = \frac{V}{L}.$$

Equation 19

Given our assumptions, we can also determine the azimuthal magnetic field surrounding the cylinder as,

$$\boldsymbol{B} = B_\theta(r)\widehat{\boldsymbol{\theta}} = \frac{\mu_0 I}{2\pi r}\widehat{\boldsymbol{\theta}},$$

Equation 20

where r is the distance from the current carrying cylinder. As we now have a current (charges moving) in a magnetic field, **J**x**B** forces (also called Lorentz Forces) will be exerted on the cylinder. Or, we can describe it in terms of the energy density ($\varepsilon_B$), which is equivalent to the magnetic pressure ($p_{mag}$),

$$p_{mag} = \frac{B^2}{2\mu_0}.$$

Equation 21

Substituting Equation 20 into Equation 21 we find that

$$p_{mag} = \frac{\mu_0 I^2}{8\pi^2 r^2} \propto \frac{I^2}{r^2}.$$

Equation 22

From Equation 22 it becomes clear that, if we want the strongest pinching effect, we need a high current and a small radius.

From Equation 2, it is clear that, if we want a fast-current risetime, we need to minimize our inductance. We can solve for the inductance in two different ways. The first method of solving for inductance is through the flux density of our magnetic field,

$$\Phi = \int_A \boldsymbol{B} \cdot d\boldsymbol{A} = \int_{r_{in}}^{r_{out}} \int_0^h \left(\frac{\mu_0 I}{2\pi r}\right) dz\, dr = \frac{\mu_0 I h}{2\pi} \int_{r_{in}}^{r_{out}} \frac{1}{r}\, dr = \frac{\mu_0 I h}{2\pi} ln\left(\frac{r_{out}}{r_{in}}\right),$$

Equation 23

where the inductance can then be expressed as,

$$L \equiv \frac{\Phi}{I} = \frac{\mu_0 h}{2\pi} ln\left(\frac{r_{out}}{r_{in}}\right).$$

Equation 24

The second method is through integrating the magnetic energy density over the entire volume of the vacuum cavity,

$$\varepsilon_B = \int_V \left(\frac{B^2}{2\mu_0}\right) \cdot dV = \int_{r_{in}}^{r_{out}} \int_0^{2\pi} \int_0^h \frac{1}{2\mu_0} \left(\frac{\mu_0 I}{2\pi r}\right)^2 \cdot r\, d\theta\, dr\, dz$$

$$= \frac{1}{2\mu_0} \frac{{\mu_0}^2 I^2}{4\pi^2} \cdot 2\pi h \int_{r_{in}}^{r_{out}} \frac{1}{r}\, dr = \frac{\mu_0 h I^2}{4\pi} ln\left(\frac{r_{out}}{r_{in}}\right).$$

Equation 25

Substituting this expression into the definition of the magnetic energy stored in an inductor, we find,

$$\frac{1}{2} L I^2 \equiv \varepsilon_B = \frac{\mu_0 h I^2}{4\pi} ln\left(\frac{r_{out}}{r_{in}}\right)$$

Equation 26

therefore,

$$L = \frac{\mu_0 h}{2\pi} ln\left(\frac{r_{out}}{r_{in}}\right).$$

Equation 27

You can see that Equation 24 (L derived through the flux density of the magnetic field) is equivalent to Equation 27 (L derived through the magnetic energy density). These derivations show two important facts about the inductance: from the flux density derivation, we see that the inductance opposes a change in current, and from the magnetic energy derivation, we see that the inductance is the ability of the circuit to store energy in the magnetic field.

In the case of a variable inductance, L(t), we have,

$$L \equiv \frac{\Phi}{I} \Longrightarrow \Phi = \text{LI}.$$

Equation 28

Then, using Faraday's Law, we can see that,

$$V_L = \dot{\Phi} = \frac{d}{dt}(LI) = \dot{L}I + L\dot{I}.$$

Equation 29

From Equation 29 we see that the $\dot{L}I$ term (often called the "L-dot" term) effectively acts as the resistance term in Ohm's Law ($V_\Omega = IR$). This also shows why, when discussing the MAIZE Inductance model in Section 3.3.5.3, the code uses a time-averaged resistance of the load, as it would be effectively impossible to solve for both terms on the right-hand-side of Equation 29, independently. So, we have to the assumption that the

resistance is constant, in order to derive an estimate of the inductance throughout the pinch.

## References


[1] Erwin Marx, “Verfahren zur Schlagprüfung von Isolatoren und anderen elektrischen Vorrichtungen,” DE Patent 455,933, Feb. 1923 [Online]. Available: https://www.google.com/patents/ DE455933C?cl=en

[2] Erwin Marx, “Versuche über die Prüfung von Isolatoren mit Spannungsstößen,” Elektrotech. Z., vol. 25, pp. 652–654, 1924.

[3] M. G. Mazarakis and R. B. Spielman, “Compact, high-voltage e-beam pulser,” in Digest of Technical Papers-IEEE International Pulsed Power Conference, 1999, vol. 1. doi: 10.1109/ppc.1999.825498.

[4] A. A. Kim *et al*., “0.75 MA, 400 ns rise time LTD stage,” Digest of Technical Papers. 12th IEEE International Pulsed Power Conference. (Cat. No.99CH36358), 1999, pp. 955-958 vol.2, doi: 10.1109/PPC.1999.823675.

[5] W. A. Stygar *et al*., “Architecture of petawatt-class z-pinch accelerators,” Physical Review Special Topics - Accelerators and Beams, vol. 10, no. 3, 2007, doi: 10.1103/PhysRevSTAB.10.030401.

[6] A. A. Kim *et al*., “Development and tests of fast 1-MA linear transformer driver stages,” Physical Review Special Topics - Accelerators and Beams, vol. 12, no. 5, 2009, doi: 10.1103/PhysRevSTAB.12.050402.

[7] R. M. Gilgenbach *et al*., “MAIZE: A 1 MA LTD-driven Z-pinch at the University of Michigan,” in AIP Conference Proceedings, 2009, vol. 1088. doi: 10.1063/1.3079742.

[8] F. F. Chen, Introduction to Plasma Physics and Controlled Fusion. 2016. doi: 10.1007/978-3-319-22309-4.

[9] D. Smith, “Induction voltage adders and the induction accelerator family,” Physical Review Special Topics - Accelerators and Beams, vol. 7, no. 6, 2004, doi: 10.1103/PhysRevSTAB.7.064801.

[10] A. A. Kim and M. G. Mazarakis, “The Story of the LTD Development,” IEEE Transactions on Plasma Science, vol. 48, no. 4, 2020, doi: 10.1109/TPS.2019.2954210.

[11] Victor Kantsyrev, “Pinch Plasma Sources,” in Handbook of Optics, 3rd ed., vol. 5, M. Bass, C. MacDonald, G. Li, C. DeCusatis, and V. Mahajan, Eds. McGraw-Hill Companies, 2010, pp. 57.1-57.5.

[12] D. B. Sinars *et al*., “Experiments measuring the initial energy deposition, expansion rates and morphology of exploding wires with about 1 kA/wire,” Physics of Plasmas, vol. 8, no. 1, 2001, doi: 10.1063/1.1323759.

[13] S. V. Lebedev *et al*., “Plasma formation and the implosion phase of wire array z-pinch experiments,” Laser and Particle Beams, vol. 19, no. 3, 2001, doi: 10.1017/S0263034601193122.

[14] T. A. Shelkovenko *et al*., “Wire core and coronal plasma expansion in wire-array Z pinches with small numbers of wires,” Physics of Plasmas, vol. 14, no. 10, 2007, doi: 10.1063/1.2786859.

[15] S. V. Lebedev *et al*., “Effect of core-corona plasma structure on seeding of instabilities in wire array Z pinches,” Physical Review Letters, vol. 85, no. 1, 2000, doi: 10.1103/PhysRevLett.85.98.

[16] B. Jones *et al*., “Planar wire-array Z-pinch implosion dynamics and X-ray scaling at multiple-MA drive currents for a compact multisource hohlraum configuration,” Physical Review Letters, vol. 104, no. 12, 2010, doi: 10.1103/PhysRevLett.104.125001.

[17] A. S. Safronova *et al*., “Searching for efficient X-ray radiators for wire array Z-pinch plasmas using mid-atomic-number single planar wire arrays on Zebra at UNR,” High Energy Density Physics, vol. 7, no. 4, 2011, doi: 10.1016/j.hedp.2011.05.008.

[18] I. K. Aivazov *et al*., “Formation of axial foreplasma channel in the initial stage of the compression of a multiwire system by megampere currents (experimental),” Sov. J. Plasma Phys., vol. 14, p. 110, 1988.

[19] S. C. Bott *et al*., “Dynamics of cylindrically converging precursor plasma flow in wire-array Z -pinch experiments,” Physical Review E - Statistical, Nonlinear, and Soft Matter Physics, vol. 74, no. 4, 2006, doi: 10.1103/PhysRevE.74.046403.

[20] S. C. Bott *et al*., “The formation of precursor structures in cylindrical and ‘4 × 4’ wire arrays,” in IEEE Transactions on Plasma Science, 2007, vol. 35, no. 2 I. doi: 10.1109/TPS.2007.893253.

[21] C. A. Coverdale *et al*., “Observation of >400-eV precursor plasmas from low-wire-number copper arrays at the 1-MA zebra facility,” Physical Review Letters, vol. 102, no. 15, 2009, doi: 10.1103/PhysRevLett.102.155006.

[22] R. D. McBride *et al*., “Implosion dynamics and radiation characteristics of wire-array Z pinches on the Cornell Beam Research Accelerator,” Physics of Plasmas, vol. 16, no. 1, 2009, doi: 10.1063/1.3054537.

[23] M. E. Cuneo *et al*., “Compact single and nested tungsten-wire-array dynamics at 14-19 MA and applications to inertial confinement fusion,” Physics of Plasmas, vol. 13, no. 5, 2006, doi: 10.1063/1.2177140.

[24] V. L. Kantsyrev *et al*., “Double planar wire array as a compact plasma radiation source,” Physics of Plasmas, vol. 15, no. 3, 2008, doi: 10.1063/1.2896577.

[25] K. M. Williamson *et al*., “Implosion dynamics in double planar wire array Z pinches,” Physics of Plasmas, vol. 17, no. 11, 2010, doi: 10.1063/1.3511775.

[26] A. S. Safronova *et al*., “Double and Single Planar Wire Arrays on University-Scale Low-Impedance LTD Generator,” IEEE Transactions on Plasma Science, vol. 44, no. 4, 2016, doi: 10.1109/TPS.2016.2538291.

[27] V. L. Kantsyrev *et al*., “Studies of Implosion and Radiative Properties of Tungsten Planar Wire Arrays on Michigan’s Linear Transformer Driver Pulsed-Power Generator,” IEEE Transactions on Plasma Science, vol. 46, no. 11, 2018, doi: 10.1109/TPS.2018.2874045.

[28] C. J. Butcher *et al*., “Characteristic Effects of Pulsed Power Generators of Different Architecture on the Implosion Dynamics of Mid-Z Double Planar Wire Arrays,” 2021. doi: 10.1109/icops36761.2021.9588400.

[29] S. N. Bland *et al*., “Implosion and stagnation of wire array Z pinches,” in Physics of Plasmas, 2007, vol. 14, no. 5. doi: 10.1063/1.2671940.

[30] V. L. Kantsyrev *et al*., “Properties of a planar wire arrays Z-pinch source and comparisons with cylindrical arrays,” High Energy Density Physics, vol. 3, no. 1–2, 2007, doi: 10.1016/j.hedp.2007.02.009.

[31] A. A. Esaulov *et al*., “WADM and radiation MHD simulations of compact multi-planar and cylindrical wire arrays at 1 MA currents,” High Energy Density Physics, vol. 5, no. 3, 2009, doi: 10.1016/j.hedp.2009.03.010.

[32] A. Stafford *et al*., “Radiation from mid-atomic-number X-pinches at 1.5-1.7 MA,” Physics of Plasmas, vol. 23, no. 10, 2016, doi: 10.1063/1.4965245.

[33] R. R. Childers *et al*., “X-Ray Line Polarization of Ne-Like Mo Spectra from X-pinch Plasmas,” IEEE Transactions on Plasma Science, vol. 46, no. 11, 2018, doi: 10.1109/TPS.2018.2863599.

[34] V. L. Kantsyrev *et al*., “A review of new wire arrays with open and closed magnetic configurations at the 1.6 MA Zebra generator for radiative properties and opacity effects,” High Energy Density Physics, vol. 5, no. 3. 2009. doi: 10.1016/j.hedp.2009.04.001.

[35] V. L. Kantsyrev *et al*., “Radiation sources with planar wire arrays and planar foils for inertial confinement fusion and high energy density physics research,” Physics of Plasmas, vol. 21, no. 3, 2014, doi: 10.1063/1.4865367.

[36] V. L. Kantsyrev *et al*., “New compact hohlraum configuration research at the 1.7 MA Z-pinch generator,” in AIP Conference Proceedings, 2014, vol. 1639. doi: 10.1063/1.4904787.

[37] D. W. Scudder *et al*., “The Los Alamos megamp fiber z-pinch experiment,” in Phys. of Alt. Magnetic Confinement Schemes, 1991, pp. 519–525.

[38] B. S. Bauer *et al*., “Proceedings of the Fourth International Conference on Dense Z-pinches,” in AIP Conf. Proc., 1997, p. 409.

[39] A. S. Chuvatin *et al*., “Operation of a load current multiplier on a nanosecond mega-ampere pulse forming line generator,” Physical Review Special Topics - Accelerators and Beams, vol. 13, no. 1, 2010, doi: 10.1103/PhysRevSTAB.13.010401.

[40] V. L. Kantsyrev *et al*., “X-ray pulse shaping in experiments with planar wire arrays at the 1.6 MA Zebra generator,” in Journal of Physics: Conference Series, 2010, vol. 244, no. PART 3. doi: 10.1088/1742-6596/244/3/032030.

[41] D. A. Yager-Elorriaga *et al*., “Seeded and unseeded helical modes in magnetized, non-imploding cylindrical liner-plasmas,” Physics of Plasmas, vol. 23, no. 10, 2016, doi: 10.1063/1.4965240.

[42] A. M. Steiner *et al*., “Determination of plasma pinch time and effective current radius of double planar wire array implosions from current measurements on a 1-MA linear transformer driver,” Physics of Plasmas, vol. 23, no. 10, 2016, doi: 10.1063/1.4965241.

[43] A. M. Steiner, “The Electrothermal Instability on Pulsed Power Ablations of Thin Foils,” PhD Dissertation, University of Michigan, Ann Arbor, 2016.

[44] W. Rogowski and W. Steinhaus, “Die Messung der magnetischen Spannung,” Archiv für Elektrotechnik, vol. 1, no. 4, 1912, doi: 10.1007/bf01656479.

[45] P. K. Panigrahi and K. Muralidhar, “Laser schlieren and shadowgraph,” in SpringerBriefs in Applied Sciences and Technology, vol. 2, 2012. doi: 10.1007/978-1-4614-4535-7_2.

[46] D. A. Yager-Elorriaga, “Helical Instabilities in Magnetized Cylindrical Liner-Plasmas,” PhD Dissertation, University of Michigan, Ann Arbor, 2017.

[47] D. A. Yager-Elorriaga *et al*., "Discrete helical modes in imploding and exploding cylindrical, magnetized liners," Physics of Plasmas, vol. 23, no. 12, 2016, doi: 10.1063/1.4969082.

[48] A. M. Steiner *et al*., "The electro-thermal stability of tantalum relative to aluminum and titanium in cylindrical liner ablation experiments at 550 kA," Physics of Plasmas, vol. 25, no. 3, 2018, doi: 10.1063/1.5012891.

[49] B. L. Henke *et al*., "X-ray interactions: Photoabsorption, scattering, transmission, and reflection at E = 50-30, 000 eV, Z = 1-92," Atomic Data and Nuclear Data Tables, vol. 54, no. 2, 1993, doi: 10.1006/adnd.1993.1013.

[50] Opto Diode Corp., "Photodiodes: Electron, Photon, X-Ray Detectors (AXUV)," https://optodiode.com/photodiodes-axuv-detectors.html.

[51] G. C. Idzorek and R. J. Bartlett, "Silicon photodiode characterization from 1 eV to 10 eV," Proc. SPIE 3114, EUV, X-Ray, and Gamma-Ray Instrumentation for Astronomy VIII, vol. 3114, pp. 349–356, 1997.

[52] H. O. Funsten *et al*., "Response of 100% internal quantum efficiency silicon photodiodes to 200 eV-40 keV electrons," IEEE Transactions on Nuclear Science, vol. 44, no. 6 PART 3, 1997, doi: 10.1109/23.650863.

[53] K. W. Wenzel *et al*., "Soft Xray Silicon Photodiodes with 100% Quantum Efficiency," IEEE Transactions on Nuclear Science, vol. 41, no. 4, 1994, doi: 10.1109/23.322843.

[54] G. C. Idzorek and R. J. Bartlett, "Silicon photodiode soft X-ray detectors for pulsed power experiments," Digest of Technical Papers-IEEE International Pulsed Power Conference, vol. 2, 1997, doi: 10.1109/ppc.1997.674576.

[55] G. C. Idzorek and R. J. Bartlett, "Silicon photodiode characterization from 1 eV to 10 keV," EUV, X-Ray, and Gamma-Ray Instrumentation for Astronomy VIII, vol. 3114, 1997, doi: 10.1117/12.278897.

[56] J. Liu *et al*., "Design, fabrication and testing of CVD diamond detectors with high performance," AIP Advances, vol. 9, no. 4, 2019, doi: 10.1063/1.5094516.

[57] R. R. Prasad, "Diamond Radiation Detectors." Alameda Applied Science Corporation.

[58] R. B. Spielman, "Diamond photoconducting detectors as high power z-pinch diagnostics (invited)," Review of Scientific Instruments, vol. 66, no. 1, 1995, doi: 10.1063/1.1146188.

[59] J. Schein *et al*., "Radiation hard diamond laser beam profiler with subnanosecond temporal resolution," Review of Scientific Instruments, vol. 73, no. 1, 2002, doi: 10.1063/1.1424904.

[60] D. R. Kania *et al*., "Absolute x-ray power measurements with subnanosecond time resolution using type IIa diamond photoconductors," Journal of Applied Physics, vol. 68, no. 1, 1990, doi: 10.1063/1.347104.

[61] Rod Nave, "Bragg's Law," http://hyperphysics.phy-astr.gsu.edu/hbase/quantum/bragg.html.

[62] E. V. Aglizki *et al*., "New satellite structure of the solar and laser plasma spectra in vicinity of the Lα (mg xii) line," Solar Physics, vol. 56, no. 2, 1978, doi: 10.1007/BF00152478.

[63] N. D. Ouart *et al*., "Studies of radiative and implosion characteristics from brass planar wire arrays," in IEEE Transactions on Plasma Science, 2010, vol. 38, no. 4 PART 1. doi: 10.1109/TPS.2010.2040093.

[64] C. J. Butcher *et al*., "Load dynamics of double planar foil liners and double planar wire arrays on the UM MAIZE LTD generator," Physics of Plasmas, vol. 28, no. 8, 2021, doi: 10.1063/5.0044058.

[65] Matt Cooper, "The Compact Pulsed Power Generator Sparky II And Two X-Ray Spectroscopic Devices For Diagnosing Laboratory Plasmas," Master's Thesis, University of Nevada, Reno, Reno, 2016.

[66] O. B. Chassela *et al*., "Thermal characterization of resistance and gain of microchannel plate (MCP) detectors for the JENI experiment," CEAS Space Journal, vol. 11, no. 4, 2019, doi: 10.1007/s12567-019-00265-9.

[67] A. S. Shlyaptseva *et al*., "X-ray spectropolarimetry of high-current x-pinch plasmas," 2001. doi: 10.1109/ppps.2001.960776.

[68] Teledyne Princeton Instruments, "SOPHIA®-XO System Manual," no. 3. Trenton, NJ, 2019.

[69] K. A. Schultz *et al*., "Study of pure and mixed clustered noble gas puffs irradiated with a high intensity (7 × 1019 W/cm2) sub-ps laser beam and achievement of a strong X-ray flash in a laser-generated debris-free X-ray source," Laser and Particle Beams, vol. 37, no. 3, 2019, doi: 10.1017/S0263034619000521.

[70] Kimberly Schultz, "The Experimental Study of Characterized Noble Gas Puffs Irradiated by Ultra- Short Laser Pulses Compared with X-Pinches as an X-Ray Source," PhD Dissertation, University of Nevada, Reno, Reno, 2017.

[71] I. Shrestha *et al*., “Study of electron beams in wire arrays at 1-MA Z-pinch generators,” in IEEE Transactions on Plasma Science, 2010, vol. 38, no. 4 PART 1. doi: 10.1109/TPS.2010.2041365.

[72] A. A. Esaulov *et al*., “Wire dynamics model of the implosion of nested and planar wire arrays,” Physics of Plasmas, vol. 13, no. 12, 2006, doi: 10.1063/1.2402147.

[73] M. F. Gu, “The flexible atomic code,” Canadian Journal of Physics, vol. 86, no. 5. 2008. doi: 10.1139/P07-197.

[74] Stephanie Hansen, “Development and application of L-shell spectroscopic modelling for plasma diagnostics,” PhD Dissertation, University of Nevada, Reno, Reno, 2003.

[75] Nicholas Ouart, “Radiative properties of Z-pinch and laser produced plasmas from mid-atomic-number materials,” PhD Dissertation, University of Nevada, Reno, Reno, 2010.

[76] Austin Stafford, “Radiation from Precursor Plasmas of Cylindrical Wire Array and X-pinch Plasmas at 1-1.7 MA Current and Notable Spectroscopic Signatures of fs Laser Produced Plasmas,” PhD Dissertation, University of Nevada, Reno, Reno, 2016.

[77] R. D. McBride *et al*., “A Primer on Pulsed Power and Linear Transformer Drivers for High Energy Density Physics Applications,” IEEE Transactions on Plasma Science, vol. 46, no. 11, 2018, doi: 10.1109/TPS.2018.2870099.

[78] V. L. Kantsyrev *et al*., “Compact hohlraum configuration with parallel planar-wire-array x-ray sources at the 1.7-MA Zebra generator,” Physical Review E - Statistical, Nonlinear, and Soft Matter Physics, vol. 90, no. 6, 2014, doi: 10.1103/PhysRevE.90.063101.

[79] A. S. Safronova *et al*., “Radiation from mixed multi-planar wire arrays,” Physics of Plasmas, vol. 21, no. 3, 2014, doi: 10.1063/1.4864335.

[80] A. S. Safronova *et al*., “Larger sized planar wire arrays of complex configuration on 1.5-1.8 MA Z-pinch generator,” Physics of Plasmas, vol. 23, no. 10, 2016, doi: 10.1063/1.4965239.

[81] A. S. Safronova *et al*., “Radiative signatures of Z-pinch plasmas at UNR: from X-pinches to wire arrays,” International Journal of Modern Physics: Conference Series, vol. 32, 2014, doi: 10.1142/s2010194514603160.

[82] A. S. Safronova *et al*., “Analysis of X-ray iron and nickel radiation and jets from planar wire arrays and X-pinches,” in Journal of Physics: Conference Series, vol. 244, no. 3, 2010, doi: 10.1088/1742-6596/244/3/032031.

[83] M. E. Weller *et al*., “Radiation from Ag high energy density Z-pinch plasmas and applications to lasing,” Physics of Plasmas, vol. 21, no. 3, 2014, doi: 10.1063/1.4865368.

[84] M. G. Mazarakis *et al*., “High-current linear transformer driver development at sandia national laboratories,” in IEEE Transactions on Plasma Science, 2010, vol. 38, no. 4 2. doi: 10.1109/TPS.2009.2035318.

[85] W. A. Stygar *et al*., “Conceptual designs of two petawatt-class pulsed-power accelerators for high-energy-density-physics experiments,” Physical Review Special Topics - Accelerators and Beams, vol. 18, no. 11, 2015, doi: 10.1103/PhysRevSTAB.18.110401.

[86] J. P. Knauer *et al*., “Response model for Kodak Biomax-MS film to x rays,” Review of Scientific Instruments, vol. 77, no. 10, 2006, doi: 10.1063/1.2220046.

[87] K. M. Chandler *et al*., “Cross calibration of new x-ray films against direct exposure film from 1 to 8 keV using the X-pinch x-ray source,” Review of Scientific Instruments, vol. 76, no. 11. 2005, doi: 10.1063/1.2135276.

[88] M. F. Yilmaz *et al*., “Modeling of K-shell Al and Mg radiation from compact single, double planar and cylindrical alloyed Al wire array plasmas produced on the 1 MA Zebra generator at UNR,” High Energy Density Physics, vol. 8, no. 1, 2012, doi: 10.1016/j.hedp.2011.10.002.

[89] V. L. Kantsyrev *et al*., “Anisotropy of radiation emitted from planar wire arrays,” Physics of Plasmas, vol. 20, no. 7, 2013, doi: 10.1063/1.4817023.

[90] A. A. Esaulov *et al*., “Wire ablation dynamics model and its application to imploding wire arrays of different geometries,” Physical Review E - Statistical, Nonlinear, and Soft Matter Physics, vol. 86, no. 4, 2012, doi: 10.1103/PhysRevE.86.046404.

[91] V. L. Kantsyrev *et al*., “Radiation physics and particle beam research on a medium-class dense plasma focus generator with complex diagnostics,” APS Division of Plasma Physics Meeting 2018, 2018.

[92] C. R. Negus and N. J. Peacock, “Local regions of high-pressure plasma in a vacuum spark,” Journal of Physics D: Applied Physics, vol. 12, no. 1, 1979, doi: 10.1088/0022-3727/12/1/011.

[93] A. K. Zverkov *et al*., “X-ray production by a high-current micropinch,” Sov. J. Plasma Physics, vol. 13, no. 7, pp. 480–482, 1987.

[94] C. K. Erber *et al*., “Optimization of micropinch plasmas produced by vacuum spark discharges,” Plasma Sources Science and Technology, vol. 5, no. 3, 1996, doi: 10.1088/0963-0252/5/3/012.

[95] P. S. Antsiferov *et al*., “Two regimes of micropinching in a low-inductance vacuum spark,” Journal of Physics D: Applied Physics, vol. 22, no. 8, 1989, doi: 10.1088/0022-3727/22/8/010.

[96] M. Roth *et al*., “Laser accelerated ions in ICF research prospects and experiments,” in Plasma Physics and Controlled Fusion, vol. 47, no. 12 B, 2005, doi: 10.1088/0741-3335/47/12B/S66.

[97] N. Vogel, “The X-ray radiation from vacuum discharges at comparatively low applied voltages,” Physics Letters, Section A: General, Atomic and Solid State Physics, vol. 248, no. 5–6, 1998, doi: 10.1016/S0375-9601(98)00655-0.

[98] Y. V. Korobkin *et al*., “Investigation of a laser driven vacuum diode X-ray source of photon energy ∼5 keV,” Laser and Particle Beams, vol. 17, no. 3, 1999, doi: 10.1017/s0263034699173178.

[99] A. Moorti *et al*., “Characteristics of a multi-keV monochromatic point x-ray source based on vacuum diode with laser-produced plasma as cathode,” Pramana - Journal of Physics, vol. 63, no. 5, 2004, doi: 10.1007/BF02704341.

[100] A. Moorti *et al*., “Cathode plasma jet pinching and intense X-ray emission in a moderate-current laser-triggered vacuum discharge,” IEEE Transactions on Plasma Science, vol. 34, no. 5 IV, 2006, doi: 10.1109/TPS.2006.883389.

[101] I. V. Romanov *et al*., “Beams of Abnormally Accelerated Electrons Emitted by a Vacuum Discharge Plasma with Laser Ignition,” Technical Physics Letters, vol. 47, Dec. 2021, doi: 10.1134/S1063785021070129.

[102] Y. V. Korobkin *et al*., “Control of parameters of micropinches formed in current-carrying plasma jet,” Physics Letters, Section A: General, Atomic and Solid State Physics, vol. 372, no. 8, 2008, doi: 10.1016/j.physleta.2007.09.016.

[103] Y. V. Korobkin *et al*., “Micropinches in laser induced moderate power vacuum discharge,” Plasma Physics and Controlled Fusion, vol. 50, no. 6, 2008, doi: 10.1088/0741-3335/50/6/065002.

[104] I. V. Romanov *et al*., “Influence of the laser plasma-expansion specific on a cathode jet formation and the current stability in a laser-ignited vacuum discharge,” Physics of Plasmas, vol. 25, no. 8, 2018, doi: 10.1063/1.5037001.

[105] I. V. Romanov *et al*., “Study of the possibility for increasing the emission of soft X-rays from the plasma of a low-energy vacuum discharge triggered by a

laser," Plasma Physics and Controlled Fusion, vol. 61, no. 9, 2019, doi: 10.1088/1361-6587/ab362e.

[106] A. Rupasov *et al*., "Emission of a low-power laser-induced vacuum discharge plasma in the EUV and SXR spectral ranges," in EPJ Web of Conferences, vol. 167, 2018, doi: 10.1051/epjconf/201816703010.

[107] F. J. Marshall *et al*., "Absolute calibration of Kodak Biomax-MS film response to x rays in the 1.5- to 8-keV energy range," Review of Scientific Instruments, vol. 77, no. 10, 2006, doi: 10.1063/1.2221698.

[108] J. F. Seely *et al*., "Tungsten L transition line shapes and energy shifts resulting from ionization in warm dense matter," High Energy Density Physics, vol. 9, no. 2, 2013, doi: 10.1016/j.hedp.2013.03.005.

[109] C. J. Butcher *et al*., "Characteristic Effects of Pulsed Power Generators of Different Architecture on the Implosion Dynamics of Mid-Z Double Planar Wire Arrays," ***accepted to IEEE Trans. Plasma. Sci.***, 2022.